THE ATOMIC MASSES OF ^{57}Cu AND ^{59}Zn

by

Bradley Marc Sherrill

A DISSERTATION

Submitted to
Michigan State University
in partial fulfillment of the requirements
for the degree of

DOCTOR OF PHILOSOPHY

Department of Physics and Astronomy

1985

To my wife

Carolyn Moravitz Sherrill

ACKNOWLEDGMENTS

I would like to thank the staff, students, and faculty of the NSCL for their support of my education. I recognize that without their contributions the following pages would not exist.

I wish to acknowledge those people, among others, who were instrumental in making the S320 a working device: W. Benenson, R. Blue, S. Bricker, M. Distasio, L. Harwood, E. Kashy, W. Lynch, J. Nolen, J. vanderPlicht, D. Swan, J. Winfield, J. Yurkon, and an army of undergraduates.

There are several people to whom I owe special thanks. J. Winfield, M. Lowe, and R. Fox have made significant contributions to SARA; for their suggestions and help I am greatly indebted. J. Nolen has been helpful in all aspects of my graduate work, in particular he has taught me a great deal about experimental equipment and techniques. B.A. Brown has also helped me a great deal. He not only supplied the computer codes to perform the calculations, but also is responsible for most of the theory presented in this thesis. Above all, the person most responsible for the completion of this thesis and my ability to do so is W. Benenson. His

support, encouragement and teaching were greatly appreciated.

I want to thank my parents Janice and Wesley Sherrill for helping me reach this point, and my grandparents Carl and Marie Mansheim and Florence Sherrill for the special role they have played in my life.

Finally, I want to thank the person who taught me the most important lessons of my graduate years, and gave me the necessary love and affection to make it through: my wife Carolyn.

I am also grateful to MSU and the National Science Foundation for financial support during my graduate study.

TABLE OF CONTENTS

LIST OF TABLES..... viii

LIST OF FIGURES..... x

Chapter 1 - Introduction and Motivation..... 1

1.1 Motivation..... 1

1.2 Introduction to Mass Measurements..... 4
1.2.1 Stability Studies..... 4
1.2.2 Decay Studies..... 5
1.2.3 Q Value Measurements..... 8

1.3 Thesis Material and Organization..... 10

Chapter 2 - ^{57}Cu Mass Measurement..... 13

2.1 Introduction..... 13

2.2 Experimental..... 15
2.2.1 The S320 Spectrograph..... 15
2.2.2 The S320 Detector..... 18
2.2.3 Electronics..... 20
2.2.4 Particle Identification..... 23
2.2.5 Targets..... 26
2.2.6 Focal Plane Calibration..... 27

2.3 Results..... 31

2.4 Comparison with Mass Models..... 38
2.4.1 Comparison..... 38
2.4.2 Garvey-Kelson Predictions..... 40

2.5 Gamow-Teller Matrix Elements..... 41
2.5.1 Introduction..... 41
2.5.2 Derivation of Measured Values..... 43
2.5.3 Shell Model Predictions..... 46

2.6 Discussion and Conclusions..... 48

Chapter 3 - ^{59}Zn Mass Measurement..... 52

3.1 Introduction..... 52

3.2 Experimental..... 53
3.2.1 QQSP Spectrometer..... 55
3.2.2 Calibration..... 57
3.2.3 Cross Section Corrections..... 60

3.3 Results..... 60

3.4 Comparison to Mass Models..... 64
3.4.1 Comparison..... 64
3.4.2 Garvey-Kelson Predictions..... 66

3.5 Gamow-Teller Matrix Elements..... 66
3.5.1 Measured Values..... 68
3.5.2 Shell Model Calculations..... 68
3.5.3 Discussion and Conclusions..... 69

3.6 Conclusions..... 69

Chapter 4 - The Nolen-Schiffer Anomaly..... 72

4.1 Introduction..... 72

4.2 Tests for Charge Asymmetry..... 75

4.3 CDE Model..... 79
4.3.1 Introduction..... 79
4.3.2 Description of the Model..... 79
4.3.3 Results..... 83
4.3.4 Corrections..... 88

4.4 Discussion..... 94

4.5 Conclusions..... 95

Chapter 5 - The Rp-process..... 97

5.1 Introduction..... 97

5.2 Rp-process Background..... 98

5.3 Rp-process Flow to A > 56..... 102
5.3.1 Supermassive Star Explosions..... 102
5.3.2 Chaotic Cosmology..... 103
5.3.3 X-Ray Bursts..... 106

5.4 Recalculation of the ^{56}Ni(p,γ)^{57}Cu Rate.... 107
5.4.1 Introduction..... 107
5.4.2 Resonance Energy and Decay Widths.. 108

5.4.3 Photodisintegration Rates..... 115

5.5 Comparison to the Previous Calculations.... 116

5.6 Conclusions..... 124

Chapter 6 - Summary and Conclusions..... 126

Appendix A - The S320 Spectrometer..... 129

A.1 Background..... 129

A.2 Mechanical Design..... 130

A.3 Magnetic Optical Design..... 131
A.3.1 Notation..... 131
A.3.2 Optical Calculations..... 136

A.4 S320 Optical Design..... 140

A.5 Preliminary Experimental Results..... 148

Appendix B - Current Sheet Octupole..... 151

Appendix C - Data taking program SARA..... 158

LIST OF REFERENCES..... 170

LIST OF TABLES

TABLE		PAGE
2-1	Parameters for the S320 Spectrograph.....	17
2-2	Calibration comparison of levels measured with the ^{58}Ni(^{7}Li,^{6}He) reaction to those known from the ^{58}Ni(^{3}He,d) reaction.....	30
2-3	Sources of uncertainty in the ^{57}Cu mass excess..	33
2-4	Garvey-Kelson charge symmetric mass predictions for Cu isotopes. Also shown are the one and two proton separation energies for these nuclei.....	42
2-5	Known properties of ^{57}Cu.....	45
2-6	Single particle and shell model $\langle\sigma\tau\rangle$ matrix elements for the ^{57}Cu$\rightarrow^{57}$Ni, ^{29}P$\rightarrow^{29}$Si, and ^{55}Ni$\rightarrow^{55}$Co β-decays compared with experiment.....	49
3-1	Branching ratios for the ^{59}Zn$\rightarrow^{59}$Cu β decay.....	54
3-2	Garvey-Kelson charge symmetric mass predictions for Zn isotopes. Also listed are the one and two proton separation energies for these nuclei.	67
3-3	Measured vs. calculated $\langle\sigma\tau\rangle$ matrix elements for ^{59}Zn β-decay.....	70
4-1	Experimental nucleon-nucleon scattering lengths.	76
4-2	Summary of the experimental and extrapolated charge radii used in the CDE calculation.....	82
4-3	The experimental and the calculated CDEs.....	85
4-4	Main contributions to the CDE calculation.....	86
4-5	Corrections to the CDE calculation.....	87
4-6	Configuration mixing corrections to the CDE calculation.....	92

5-1 Elemental abundances calculated assuming an rp-process in chaotic cosmologies compared to solar abundances and type II stars. The data in the table is taken from WW (Wa81). The production ratios are the final mass fraction produced in the calculation divided by the solar mass fraction..... 105

5-2 Comparison of the old and the new parameters relevant to the $^{56}Ni(p,\gamma)^{57}Cu$ rate calculation.. 118

A-1 Optimized S320 spectrograph parameters for the QQDMS and the QQDS configurations..... 141

LIST OF FIGURES

FIGURE		PAGE
2-1	Top view of the S320 spectrograph.....	16
2-2	Schematic view of the S320 detector.....	19
2-3	Schematic view of the S320 electronics.....	21
2-4	Particle ID for the ^{58}Ni(^{7}Li,^{8}He) reaction...	24
2-5	Triton energy spectrum for a typical run.....	25
2-6	^{58}Ni(^{7}Li,^{6}He) spectrum used as a check of the S320 focal plane calibration.....	29
2-7	Position spectra for ^{8}He particles.....	32
2-8	The level structure of ^{57}Cu along with the predicted structure based on pertubation theory and the structure of ^{57}Ni, mirror nucleus of ^{57}Cu.....	35
2-9	Angular distributions for the measured states in ^{57}Cu.....	37
2-10	Comparison of the measured ^{57}Cu mass excess to various mass models.....	39
3-1	The QQSP spectrometer.....	56
3-2	The QQSP focal plane calibration.....	58
3-3	Pion position spectra from the ^{59}Zn mass measurement and one angular bin of the ^{14}O calibration run.....	61
3-4	Excitation spectra for ^{59}Zn and its mirror nucleus ^{59}Cu.....	63
3-5	Comparison of the ^{59}Zn mass excess to various mass models.....	65
4-1	The ratio of the experimental to the	

calculated CDEs as a function of A..... 84

4-2 Ratios of experimental to calculated CDEs versus A, including core polarization and finite well corrections..... 91

5-1 Diagram of the rp-process flow..... 101

5-2 The effect of the structure of ^{13}N on $^{12}C(p,\gamma)$ resonances. The data is taken from Ajzenberg-Selove (Aj81)..... 109

5-3 The predicted effect of the structure of ^{57}Cu on $^{56}Ni(p,\gamma)$ resonances..... 110

5-4 The ratio of the recalculated $^{56}Ni(p,\gamma)^{57}Cu$ rate in units of cm^3/mole-sec to the previously calculated rate vs. temperature. The dashed lines were calculated by varying the resonance energy by the uncertainty in the measurement, ±40 keV..... 119

5-5 Superratio of branching to A>56 vs. temperature. The dashed lines were calculated by varying the resonance energy by the uncertainty in the measurement, ±40 keV..... 123

A-1 Coordinate system for magnet optical notation..... 132

A-2 Sample MOTER calculation showing the residual momentum vs. the number of rays. The FWHM of the peak gives the predicted S320 resolution..... 139

A-3 Schematic layout of the S320 spectrograph showing the first order beam envelopes calculated with the program TRANSPORT..... 142

A-4 The optimum beam dispersion search for the S320 spectrograph..... 145

A-5 Calculated effects of reaction kinematics including the x-quad retuning. The QQDS case is better at larger k because of the smaller solid angle..... 146

A-6 Percent change in the x-quad needed to correct reaction kinematics..... 147

B-1 Cross section of the final design for the octupole magnet. One quarter of the magnet is shown. The boxed regions carry current,

while the air and iron regions are labeled. The lines drawn are lines of constant magnetic field calculated with the program POISSON.... 154

B-2 Plot of the POISSON calculated vs. measured median plane magnetic field. For reference, a true octupole field is also plotted..... 155

B-3 Detailed comparison between the measured multipole field and a pure octupole field. Also listed are the coefficients from a multipole expansion of the measured field.... 156

C-1 Schematic diagram of the NSCL data taking system..... 160

C-2 Flow diagram for online data taking..... 161

C-3 Flow diagram of offline data analysis..... 162

C-4 Flow diagram for the program SARA..... 166

C-5 Flow diagram for the subroutine DATAR..... 167

CHAPTER ONE

1.1 Motivation

The most fundamental property of any atom is its mass. From the mass the binding energy of the nucleus can be calculated, its decay modes predicted, and information on the nature of the nuclear force deduced. The abundances of the elements and their isotopes in the universe are due in large part to nuclear binding energies (C168,Ar79). Recently, based on atomic masses, predictions of new decay modes including proton decay (Fa84) and ^{14}C decay (Ro84a,St85a,Ga84) have been confirmed. Overall the importance of atomic masses can be understood when we note that indeed the mass of an atom is the lowest energy eigenvalue of the nuclear Hamiltonian.

Some of the first evidence for the shell model came from the change in slope of the binding energy curve for nuclei with magic numbers of neutrons and protons (Ma48,Ha49). In the present day, data on β-unstable nuclei still provide important information for shell model studies. Based on the properties of stable or near stable nuclei Wildenthal (Wi83) has developed a complete s-d shell

Hamiltonian. With this Hamiltonian, Wildenthal has predicted the halflives and masses of the neutron rich s-d shell nuclei. A test of the validity of the s-d shell Hamiltonian is to compare the predicted masses and lifetimes to the measured values for the s-d shell nuclei far from β-stability. This has been done for the nuclei with known properties, and in general the agreement is excellent, except for a region near ^{30}Na, where the mass excesses of very neutron rich Na isotopes are known (Th75,De83). This disagreement can be interpreted as a region of deformation. Further data on masses in the s-d shell will help understand the anomaly.

Mass data may indicate new degrees of freedom in other shells as well. In particular there are two regions where recent models have predicted new magic numbers. These are at ^{52}Ca (To81) and ^{146}Gd (Kl79). Currently, the masses of ^{51}Ca, ^{52}Ca and ^{147}Tb are unmeasured but are necessary for determining the validity of the predictions. In general new degrees of freedom are found by comparison of masses to predictions by the various models which predict atomic masses (for an almost complete summary see Maripuu (Ma76)).

Atomic mass models are based on assumptions ranging from the shell model to the liquid drop model. Some are also essentially empirical fits with thousands of free parameters. Since the mass is such a fundamental quantity, any global theory which could predict atomic masses must contain some fundamental information of the nuclear force.

Knowledge of, or the ability to predict atomic masses, is also essential to understanding the abundances of elements in the universe (Ar79). As a result there is great interest predictions of nuclear masses (see for example the proceedings of the Atomic Mass and Fundamental Constants conferences (AMCO), or the 4th International Conference on Nuclei far from Stability). Once a model has been developed, new masses far from β stability are needed to test the mass model validity. The farther from stability the model can predict, the greater its credibility.

Despite the great interest in atomic masses, of the 7000 isotopes which are predicted to be particle stable, only 1400 have known masses. The reason so few of the predicted particle stable isotopes have known masses is the difficulty in producing and studying nuclei far from β-stability. Only 284 isotopes are stable or have sufficiently long halflives that they are found naturally. In most cases the unknown isotopes must be synthesised from these nuclei. To date the largest deviation from the line of stability to measure a mass is 21 neutrons (Ro79), while β-stable nuclei are predicted up to a hundred neutrons away.

In this thesis the measurement of the mass of two nuclei far from β stability will be presented. As an indication of the importance of mass data, these results will be used to study the charge independence of the nuclear force, test a shell model for the f-p shell, and test previous assumptions used in astrophysical models involving

rapid hydrogen burning. Also as part of this thesis, techniques developed to perform mass measurements at the National Superconducting Cyclotron Laboratory at Michigan State University will be presented. Before beginning the discussion of these measurements, it is useful to review the techniques used to study nuclei far from β stability.

1.2 Introduction to Mass Measurements

The expression of mass which will be used in this thesis is the atomic mass excess defined as

$$ME = Mass - M_0 \times A \qquad (1.1)$$

where M_0= 931.5016 MeV is one atomic mass unit (AMU). The units used to quote mass will be MeV.

1.2.1 Stability Studies

There are many ways to determine the atomic mass excess of an exotic isotope. An upper limit on the mass excess can be determined by whether or not the isotope is particle stable. Historically, ^{14}Be, ^{11}Li, ^{19}C were predicted unstable, but were shown by experiment to be particle stable. Thus, the measurements which show the stability of an isotope are useful information for mass models.

Artukh et al. used deep inelastic transfer reactions with projectiles of ^{18}O (Ar69), ^{22}Ne (Ar70), and ^{40}Ar (Ar71a) to infer the stability of 28 new isotopes. They were also able to infer the instability of several isotopes

including ^{10}He (Ar71b). A review of the deep inelastic work was presented by Volkov (Vo78). Even earlier, proton spallation experiments were used to create nuclei far from β-stability (Po65,Bo74). More recently, proton spallation has been used in connection with an online mass separator to demonstrate the stability and measure masses and decay properties of very exotic K and Na isotopes (Th75,De83). Vieira has also used proton spallation and time-of-flight (TOF) techniques to identify and study neutron rich nuclei (Vi84). He and his colleagues plan to build a new, improved TOF spectrometer at LAMPF to measure the masses of nuclei produced in proton spallation reactions (Wo84).

Several groups have used high energy beams of ^{40}Ar (Sy79) and ^{48}Ca (We79,St81) from the Bevalac and the fragmentation mechanism to produce very neutron rich nuclei. Recently, Stevenson has demonstrated the particle stability of ^{19}B produced from the fragmentation of ^{48}Ca (St85b). Devices have now been built which will use the fragmentation mechanism to create nuclei far from β stability (Ha81b,Du84,La84). These devices can separate the reaction products by mass, which will allow decay properties and possibly masses to be studied for nuclei very far from β stability.

1.2.2 Decay Studies

Although useful in identifying new isotopes and in some cases studying decay properties, the above methods have not been generally useful in determining atomic mass excess.

The two general categories of experiments which have been used to determine atomic masses are decay studies and Q value measurements. Decay studies are usually performed on nuclei produced in fusion or fission reactions. Fusion reactions have been used at many laboratories, and the products separated by various types of devices such as online mass separators. Examples of this type of experiment are performed at GSI (Ro78) and CERN (Th75,De83). Fission studies are performed in such devices as COSIRIS (Bo71) and TRISTAN (Br80b).

The main technique by which many of the heavy elements, produced in either fusion or fission reactions, have had their mass excesses measured is by attempting to measure the maximum electron or positron energy from β decay, called β-endpoint measurements. The mass of an unknown isotope is derived from a known isotopes mass by

$$ME(unknown) = ME(known) + E_{\beta max} \qquad (1.2)$$

for β^- decay, and for β^+ decay

$$ME(unknown) = ME(known) + E_{\beta max} + 2m_e \qquad (1.3)$$

where m_e is the electron mass in MeV. If the decay is to an excited state in the daughter, then this excitation energy must also be known. Many authors have used this method. In fact, the Q value measurements presented in this thesis will

be compared to β-endpoint measurements for ^{57}Cu (Sh84a) and ^{59}Zn (Ar84). For examples of β-endpoint measurements and discussions of techniques, see any of the AMCO conference proceedings. The main problem in β-endpoint studies is that it is difficult to get good statistics near the endpoint. There is also usually background which must be subtracted from the spectrum. The response of the detector to the β energy is also an unknown and must be determined. The result is usually to limit the mass excess resolution to ±100keV or so. Since the nucleus being studied is also decaying, it is usually not possible to obtain information on the energy spectrum of that nucleus.

The other type of decay study, which yields a mass excess, is the study of α-chains ending in a known mass. In this case mass excess of very exotic nuclei can be inferred by

$$ME(\text{unknown}) = ME(\text{known}) + \sum_{\alpha} (ME(\alpha) + E_{\alpha}) \quad (1.4)$$

Again if any of the decays are to excited states the gamma ray energies must be measured and included. These types of studies have been performed on proton rich nuclei produced in fusion reactions (Ro78,Sc79, and Sc81 for example). The mass excesses which can be inferred have reasonable accuracy, but rely on a comparison to a single known mass. Also it is not always possible to connect α chains to known

masses. Finally, again no excited state information is obtained on the nucleus being studied.

One last method which can be used to measure atomic mass excesses from observing nuclear decays is to study the EC/β^+ ratio for proton rich nuclei (Ro84b). This ratio is sensitive to the mass difference between the mother and daughter. It is, in principle, reasonably accurate but is only applicable in a certain range of nuclei where this ratio is measureable. In general the β-decay energy for nuclei far from β-stability is large and the EC/β^+ ratio is extremely small, which makes it difficult to measure.

1.2.3 Q Value Measurements

The technique which has been used primarily in lighter nuclei to measure atomic mass excesses is the determination of the Q value of a reaction. The Q value is defined for the reaction A(B,C)D as

$$Q = ME(A) + ME(B) - ME(C) - ME(D) \qquad (1.5)$$

If the Q value can be measured and three of the involved masses are known, then the mass excess of the fourth can be determined. It is possible in fact to measure masses to better than 1 part in 10^7 with this method, which in the past have been more accurate than decay studies. The techniques and considerations for Q value measurements have been discussed by several authors (No74,Ka75,Th82). The

accuracy of this method relies on measuring the unknown Q value relative to known Q values.

It is possible to divide Q value measurements into two main categories. In the first type the nucleus to be studied is undetected. The mass excess of the particle D in the reaction A(B,C)D can be determined using two body relativistic kinematics and knowledge of the initial beam energy, scattering angle, and energy of the outgoing particle C. There have been many Q value measurements of this type, and it would be difficult to make a complete discussion of the work which has been done. Some examples of this type of measurement are the studies of mirror nuclei in the f7/2 shell by Mueller (Mu75) via the (^{3}He,^{6}He) and (^{3}He,^{7}Li) reactions. Benenson (Be79) has also used Q value measurements to study isobaric quartets in light nuclei. Some of the more exotic reactions studied of this type are the (π^{-},π^{+}) mass measurements of ^{14}Be (Gi84) and ^{18}C (Se78).

In the other general type of Q value measurement the nucleus to be studied is detected. An example of this method was the mass excess measurement of ^{17}C by the ^{48}Ca(^{18}O,^{17}C)^{49}Ti reaction (No77). This type of study is better in the sense that it is less sensitive to impurities in the beam or target, but it is more difficult to obtain excited state information on the nucleus of interest.

The main consideration for Q value studies, especially for studies on nuclei far from β stability, is the size of the cross section for the reaction. Since the cross section

drops as the reactions involve more nucleons and more complicated transfers and rearrangements, it is difficult to use Q value measurements to study nuclei very far from β stability. Although the reactions will involve the nuclear structure of the participants, it has been noted by several authors (An74,Po73,Br72) that in cases where the linear and angular momentum of the incoming and outgoing particles is matched, the reaction is favored. In general for reactions involving heavy ions this means high spin states in the residual nucleus will be favored because the angular momenta of the outgoing particle is much less than that of the incoming particle. However when the outgoing particle is heavier than the beam, it is possible to match momenta for the reaction if the appropriate beam energy is available. In these favorable cases the cross section for the reaction is expected to be a maximum for the ground state. Hence, in Q value measurements it is desirable to match, as close as possible, the momenta to maximize the cross section.

1.3 Thesis Material and Organization

In this thesis two exotic Q value measurements and their implications will be discussed. These reactions are $^{58}Ni(p,\pi^-)^{59}Zn$ and $^{58}Ni(^7Li,^8He)^{57}Cu$. With these reactions we were able to determine the mass excesses of ^{57}Cu and ^{59}Zn. These nuclei are interesting because they are $T_z = -1/2$ nuclei and are thus input for mass formula (Ke66) and provide data to study the Nolen-Schiffer anomaly (No69). Their β decays can also be used to investigate quenching of

Gamow-Teller strength in nuclear transitions. The nucleus ^{57}Cu is particularly interesting because it has, in a simple shell model, one proton outside the closed ^{56}Ni core. This makes its mass excess and level structure important for nuclear structure calculations and studies of the effect of the Coulomb force in nuclei. As we will see in chapter 5, the structure of ^{57}Cu is also important for nucleosynthesis, and in particular astrophysical models involving the rp-process (Wa81).

The organization of the thesis will treat the ^{57}Cu and ^{59}Zn measurements separately. Chapter 2 will describe the ^{57}Cu measurement, while chapter 3 will be devoted to the ^{59}Zn measurement. At the end of each chapter a discussion of the implications of the results for mass excess models and Gamow-Teller strengths will be presented. Chapter 4 will discuss the Nolen-Schiffer anomaly and the new data provided by these measurements. The possibility that this anomaly is evidence for charge symmetry breaking in the nuclear force will be reviewed. The rp-process will be discussed and its relation to the new ^{57}Cu data presented in chapter 5. The conclusions will be reviewed in chapter 6. The appendicies contain information on some of the experimental details related to the ^{57}Cu measurement. Appendix A discusses the magnetic optics calculations done for the design of the S320 spectrometer used in the ^{57}Cu mass measurement. Appendix B is a description of an octupole magnet which was designed and constructed to

improve the resolution of the spectrograph. Finally, appendix C is a description of the data taking program, SARA, used in experiments on the S320 spectrograph.

CHAPTER TWO

2.1 Introduction

The first atomic mass measured at the National Superconducting Cyclotron Laboratory (NSCL) with the K500 cyclotron was that of ^{57}Cu. The measurement was performed by determining the Q value of the ^{58}Ni(^{7}Li,^{8}He)^{57}Cu reaction, as part of this thesis. This reaction was chosen for the first attempt because of several advantages; thick targets could be used, ^{8}He has no excited states, and the cross sections were expected to be large since at the K500 beam energies it is possible to match the incoming and outgoing angular momenta of the ^{7}Li and ^{8}He nuclei. To match the incoming and outgoing particles angular momenta in the ^{58}Ni(^{7}Li,^{8}He)^{57}Cu reaction, as was discussed in the introduction, one needs a ^{7}Li beam energy of ~175MeV. The ^{8}He energy after the reaction is ~150MeV. To bend a ^{8}He nucleus with that energy requires a spectrograph with a K parameter of 280, where $K=(MeV/u)(u/q)^2$. Very few spectrometers with such a large K exist anywhere in the world. The HRS at Los Alamos (En70), GSI's simple

spectrograph (Sc83), and Big Karl (Ma83) at the KBI are examples. However, the NSCL is unique in the combination of the correct ^{7}Li beam energy and a K=320 spectrograph. Thus, the ^{58}Ni(^{7}Li,^{8}He) Q value measurement was proposed and performed at the NSCL.

The nucleus ^{57}Cu has received much attention, because it is a simple nucleus with one proton outside a ^{56}Ni closed core. It has only been observed twice, and most of its properties are not well known. It was observed first in a study of β-delayed proton emission from ^{57}Zn (Vi76). Because of the nature of the experiment only high excitation proton unbound states were observed. The other observation was reported in a preliminary report from a group at Tohoku University(Sh84a,Mi83), where ^{57}Cu was produced via the ^{58}Ni(p,2n) reaction. They measured the ^{57}Cu lifetime to be 233±16 msec and Q_{β}=7.72±0.13 MeV. Because ^{57}Cu has one proton outside the ^{56}Ni closed core, it makes data on the low-lying states and mass of ^{57}Cu very useful for studying nuclear structure effects in the fp shell, and in particular studying the effects of the Coulomb force in nuclei. One particular application of this data is in studying the Nolen-Schiffer anomaly(No69). Further, due to the role closed core nuclei play in nature, ^{57}Cu is important for astrophysical models. The primary model for which data on ^{57}Cu is needed is the rp-process(Wa81,Wa83). However, ^{57}Cu is difficult to study because it is 6 neutrons lighter than the first β-stable Cu isotope, ^{63}Cu. This means production

cross sections for transfer reactions are low and the lifetime is short.

In this chapter the experimental setup of the S320 spectrograph will be discussed, including the magnetic layout, detector, electronics, and the data acquisition system hardware and software. The mass measurement results, information on cross sections for the (^{7}Li,^{8}He) reaction, and level structure will be presented. The measured mass excess will be compared to standard nuclear mass models and the extracted Gamow-Teller (G-T) matrix elements compared to those calculated by the shell model. For a case such as ^{57}Cu one would expect the shell model calculations to be very good if the ^{56}Ni core is indeed doubly magic. The closed core nature of ^{56}Ni also makes the nucleus ^{57}Cu a particularly good case to study the Nolen-Schiffer anomaly because corrections to the calculated Coulomb displacement energy which depend on nuclear structure should be calculable. The Nolen-Schiffer anomaly will be discussed in chapter 4. The new information obtained on ^{57}Cu may also significantly influence the rates of element production for A>56 from the rp-process and the energy generation at late times in such a process. This will be discussed in detail in chapter 5.

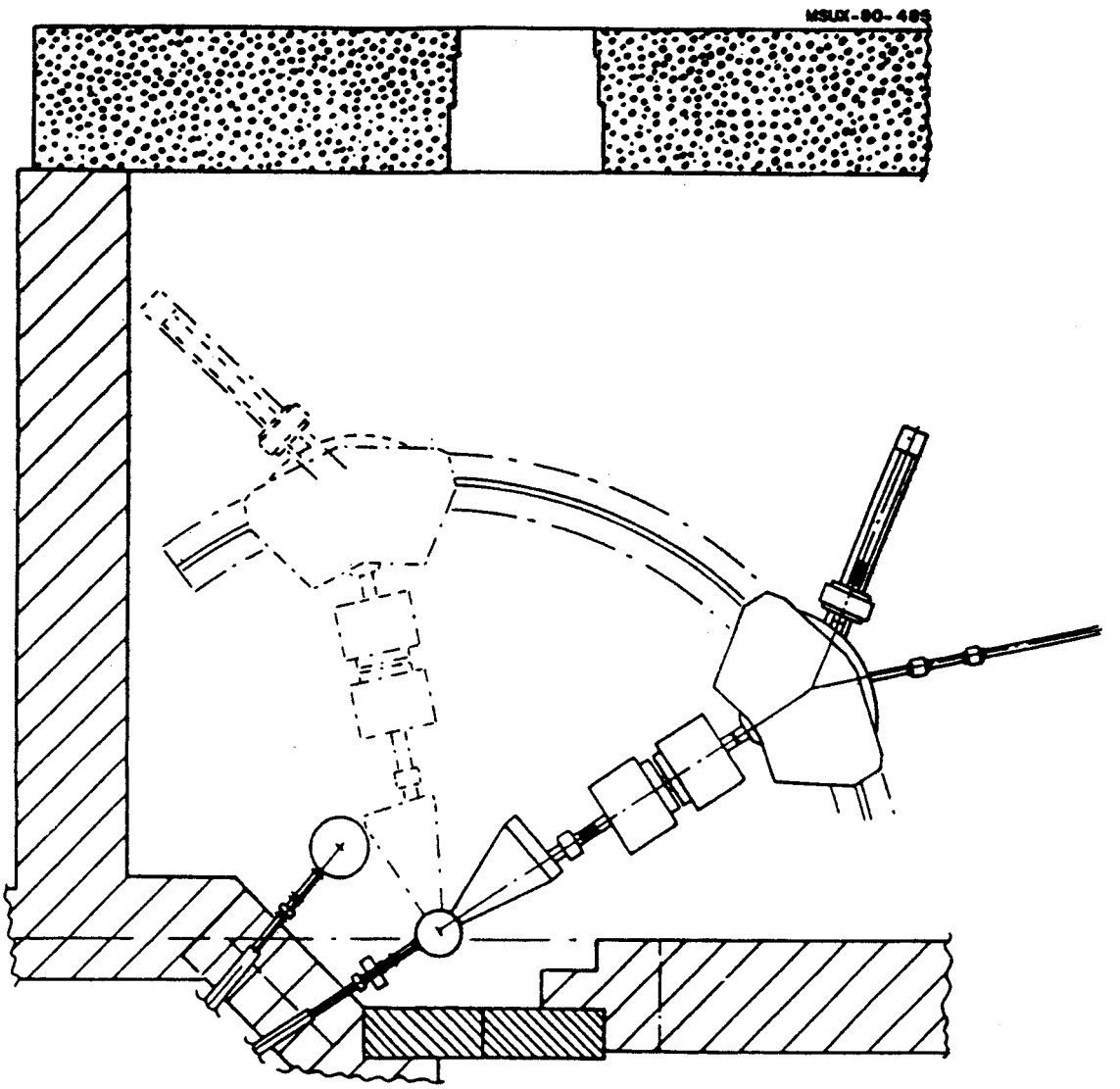

Figure 2-1: Top view of the S320 spectrograph.

Table 2-1: Parameters for the S320 Spectrograph.

Dispersion:	1.6 cm/% ($\Delta p/p$)
Magnification:	$M_x = -0.67$ (D/M=2.4)
	$M_y = -2.5$
Assumed target spot size:	0.5mm incoherent width
	3mm tall, dispersion
	matched (2.5cm/% opt.)
Solid Angle:	$\Delta\theta = \pm$ 12mr
	$\Delta\phi = \pm$ 12mr
	Ω = 0.56 msr
Calculated Line Width:	$\Delta E/E \leq 0.1\%$, 0.8mm
Range:	$\Delta E/E$ = 20%
	60 MeV at 300 MeV
Focal Plane:	Normal incidence,
	16cm long by 2.6cm tall
Maximum Rigidity:	$B\rho_{max} = 2.57$ T-m at
	B = 1.47 T
	$\rho_{max} = 1.75$ m

1.2 Experimental

1.2.1 The S320 Spectrograph

The measurements were performed in the K=320, S320 spectrograph. A top view of the spectrograph is shown in Figure 2-1. A schematic view of the component layout and beam envelopes calculated with the program TRANSPORT(Br77b) are shown in Figure A-3. The details of the S320 optical design will be presented in appendix A. The important optical and magnetic parameters for the S320 spectrograph are given in Table 2-1. The spectrograph is operated in the dispersion-matched mode with kinematic effects corrected by retuning the quadrupole doublet, as described in appendix A. The energy range of the device, 20%, or 60MeV at 300MeV beam energy, is adequate, but the small solid angle, 0.5msr (QDDD spectrometers have typically 14msr solid angles), makes collection times for experiments longer, and makes some low cross section experiments unfeasible. Due to the low solid angle, the minimum cross section which can be measured in a 3 day run, given typical K500 intensities, is 10 nb/sr. The 0.1% design energy resolution has not been reached to date. This may be due to a beam energy spread larger than the expected 0.1%, or an incoherent spot size larger than the assumed 0.5 mm. A detailed study to determine the cause of the failure to reach the design resolution has not been performed. The best energy resolution achieved thus far is 0.15%. In the present experiment, the thick targets used limited the resolution to values greater than 0.2%.

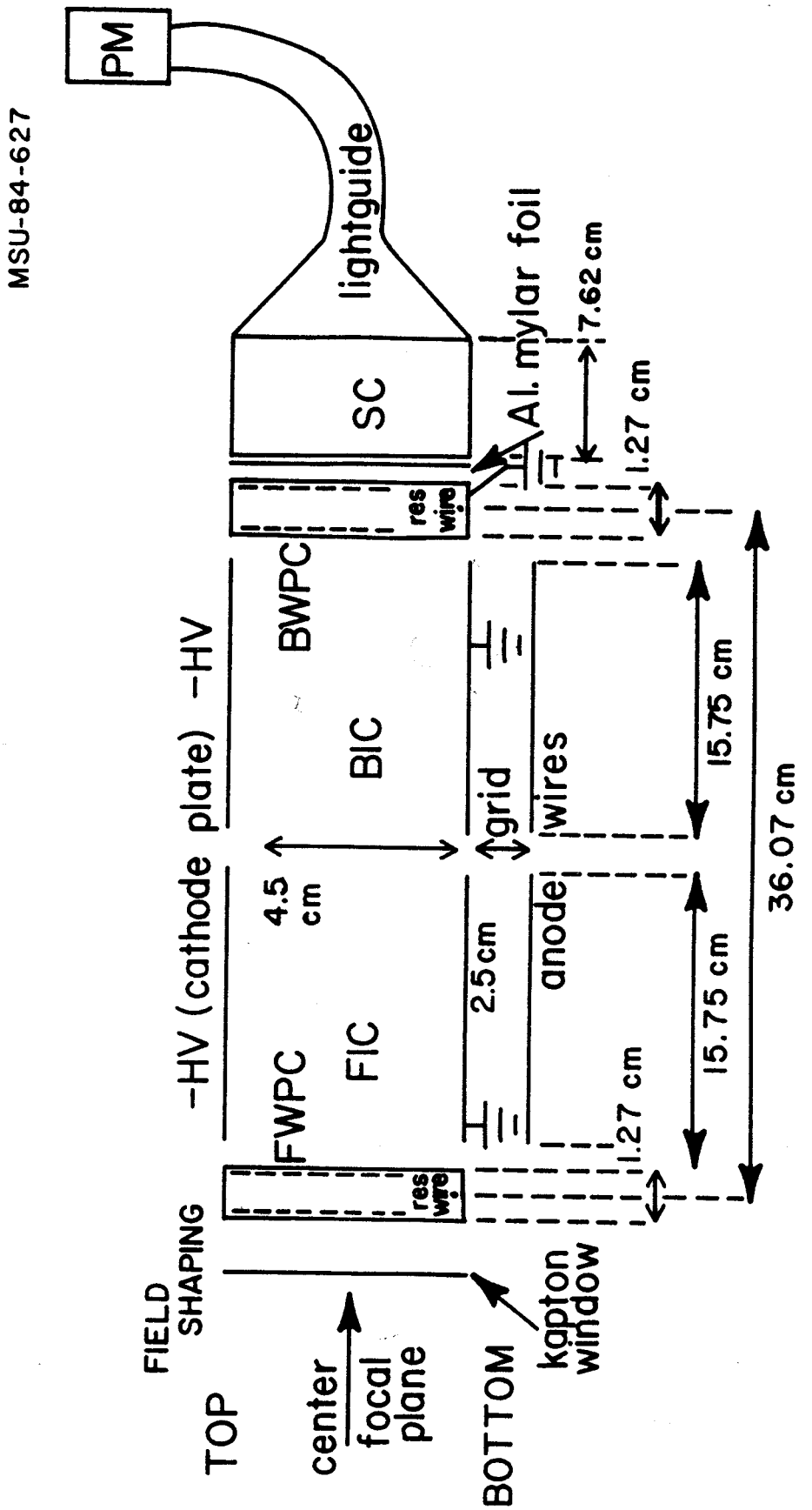

Figure 2-2: Schematic view of the S320 detector.

1.2.2 The S320 Detector

A schematic side view of the S320 detector is shown in Figure 2-2. The detector consists of two position sensitive proportional wires separated by ~40cm, and two ion chambers for energy loss information. The detector is backed with a 7.62cm thick plastic scintillator used for an event trigger, light output information, and a start signal for time-of-flight (TOF) against a stop from the cyclotron RF. This time provides a signal which is dependent on the particle velocity in the spectrograph. This detector has been described elsewhere in more detail by Yurkon et al.(Yu82).

2.2.3 Electronics

The electronics used for this experiment were relatively simple and are shown in the schematic diagram of Figure 2-3. There were nine signals which were recorded from the detector and processed by the electronics. An event was defined as a scintillator anode pulse above a CFD discriminator level set to gate out room background. The left and right signals from each wire were digitized, and the position was calculated by computer. The difference in position between the front and back wires was taken as a measure of the scattering angle relative to the central angle of the spectrograph. This is true because in first order $\theta_f = (\theta/\theta) \times \theta_i$, where $\theta_{i(f)}$ is the initial (final) scattering angle relative to the central spectrograph angle; higher order corrections are small. The anode signals were read from each ion chamber.

MSU-84-615

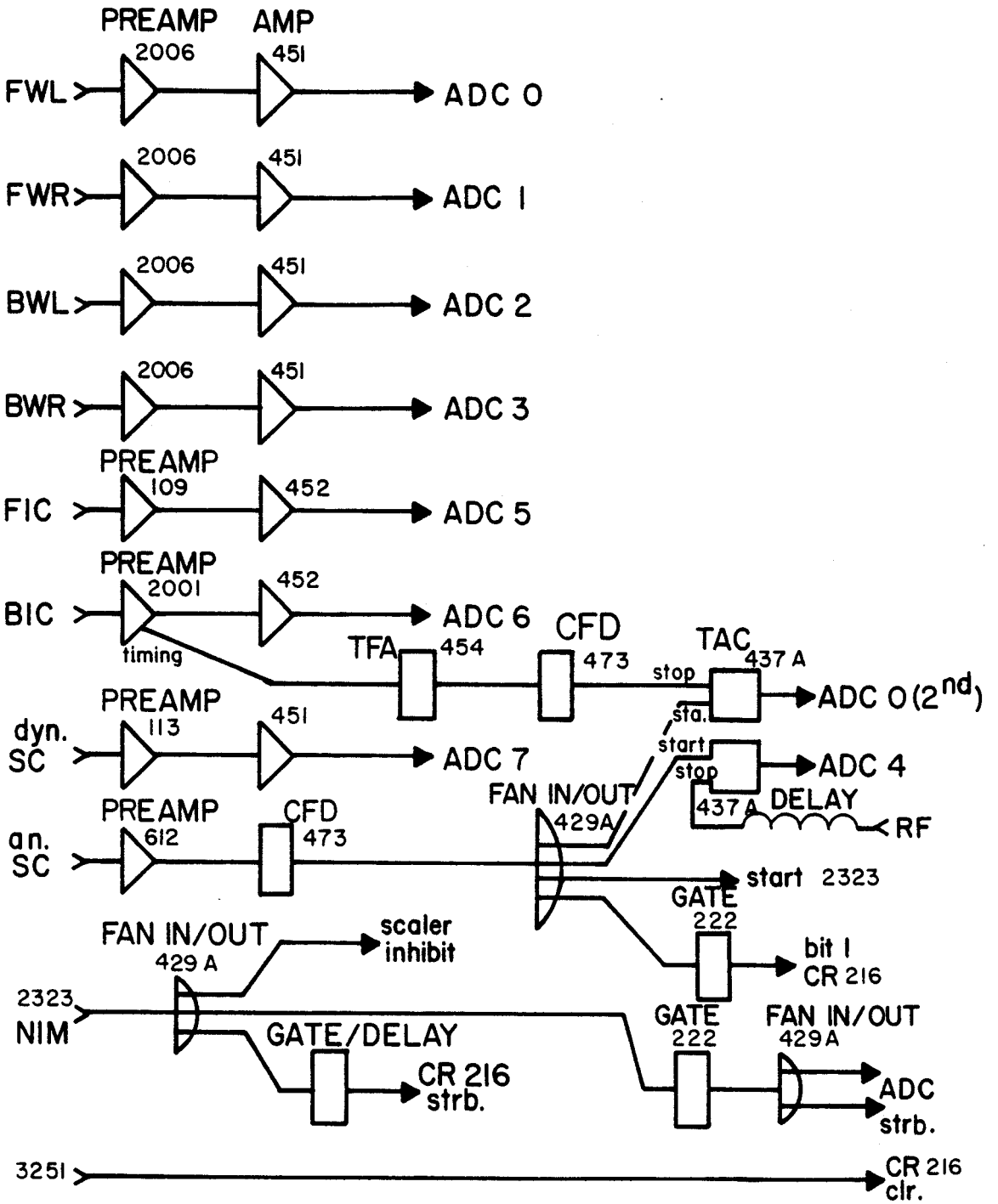

Figure 2-3: Schematic view of the S320 electronics.

A light output from the scintillator was read via the dynode signal from the scintillator phototube. Finally, two times were recorded using TACs. The drift time of the ions in the second ion chamber relative to the start pulse from the scintillator was used for y-height information. Also, the difference in time between a start from the scintillator and the next cyclotron RF pulse was recorded to measure velocity.

The signals were digitized with an ORTEC AD811 12bit ADC. The ADCs were read by an LSI-11 microcomputer acting as a smart CAMAC crate controller. The CAMAC data acquisition has been described in detail by Au et al. (Au83). The code to run the LSI was generated by the code SPECTRO written by R. Fox and D. Notmann(Fo84). The LSI stored events until an 8192 byte buffer was full, at which time the data was passed via a Kinetic Systems dataway interface to a VAX 11/750 computer. In the VAX an acquisition program named ROUTER distributed the data to subtasks which recorded the data on tape, recorded scalers, binned data, etc. The data display and analysis part of this system along with some details of the ROUTER system are discussed in appendix C. The online data acquisition system allowed the data to be monitored and analyzed as it was taken. In the case of the ^{58}Ni(^{7}Li,^{8}He) experiment it was almost possible to analyze the ^{8}He spectrum as it was taken. The same acquisition system was used offline to reread the data back from tape to perform more detailed analysis.

2.2.4 Particle Identification

The particle ID spectrum obtained for the $^{58}Ni(^{7}Li,^{8}He)^{57}Cu$ reaction is shown in Figure 2-4. The data are summed over angles ranging from 4 to 7 degrees. The detector gas was isobutane at a pressure of 70 Torr. Plotted in the figure is TOF vs. ΔE in the ion chamber and LIGHT output. In the TOF-ΔE spectrum the $^{8}HE^{2+}$ ions overlap with the $^{4}He^{1+}$ ions since both have the same velocity ($\Delta E \propto (Z^2/v^2)$ and $TOF \propto v$). However, the light output which is approximately proportional to $E^{1.7}$(Be74) separates the two because the $^{8}He^{2+}$ ions will have three times the $^{4}He^{1+}$ ions light output. Requiring counts to fall in the proper region of both plots clearly identifies the $^{8}He^{2+}$ ions. The TOF-LIGHT plot has some background, which may be due to the plastic's sensitivity to neutrons.

Two other particle groups which are prominent in the particle ID spectra are tritons and $^{7}Li^{2+}$ elastic scattering. The tritons, which are probably from some process such as a 3-body reaction, dominated the detector count rate at 1000 tritons/sec for a 20pnA beam. In contrast, the $^{8}He(^{57}Cu$ g.s.) rate was 0.5/hr. The triton energy spectrum for a typical run with θ_{sp} = 5 degrees and B_{sp} = 14.289 kG is shown in Figure 2-5.

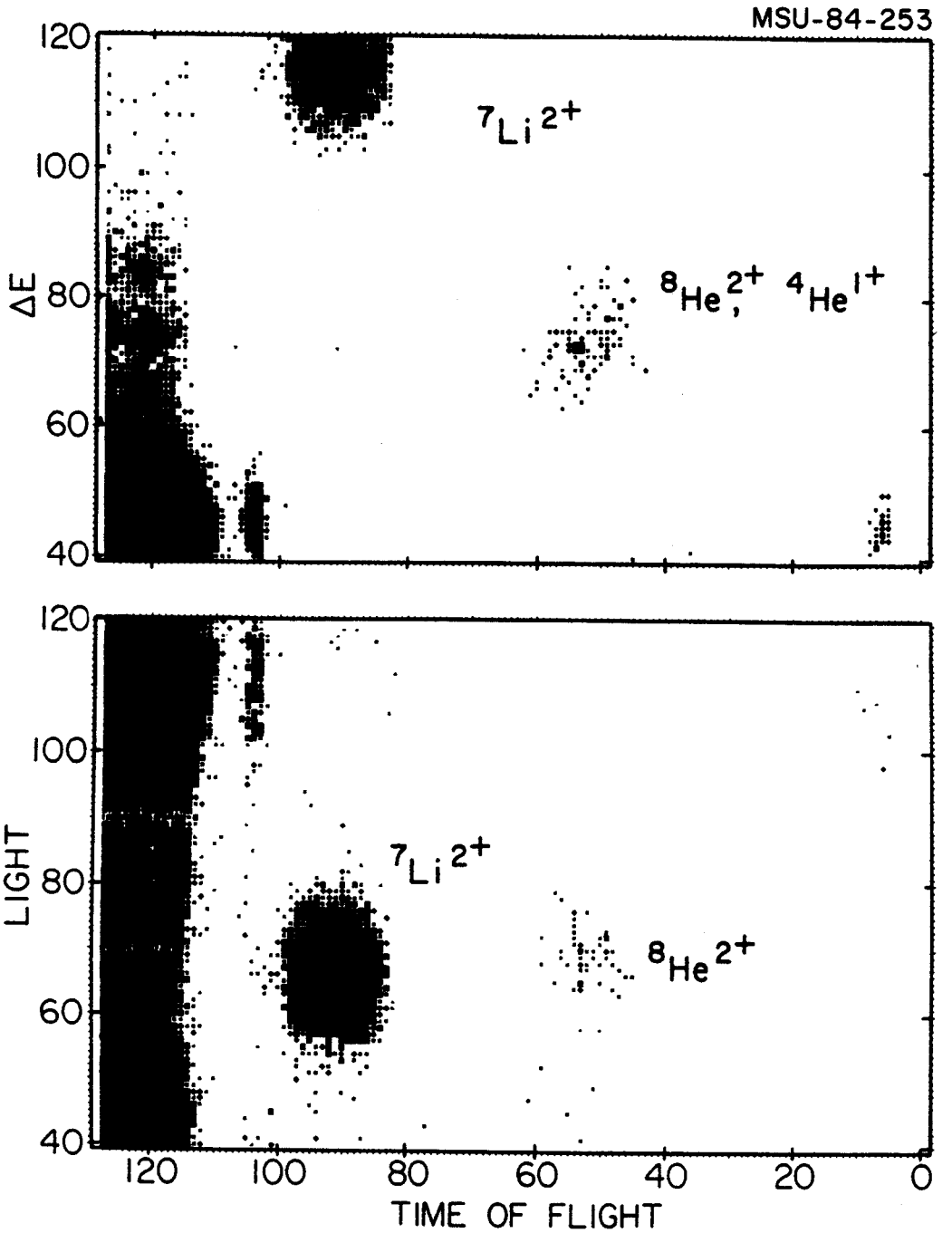

Figure 2-4: Particle ID for the $^{58}Ni(^{7}Li,^{8}He)$ reaction.

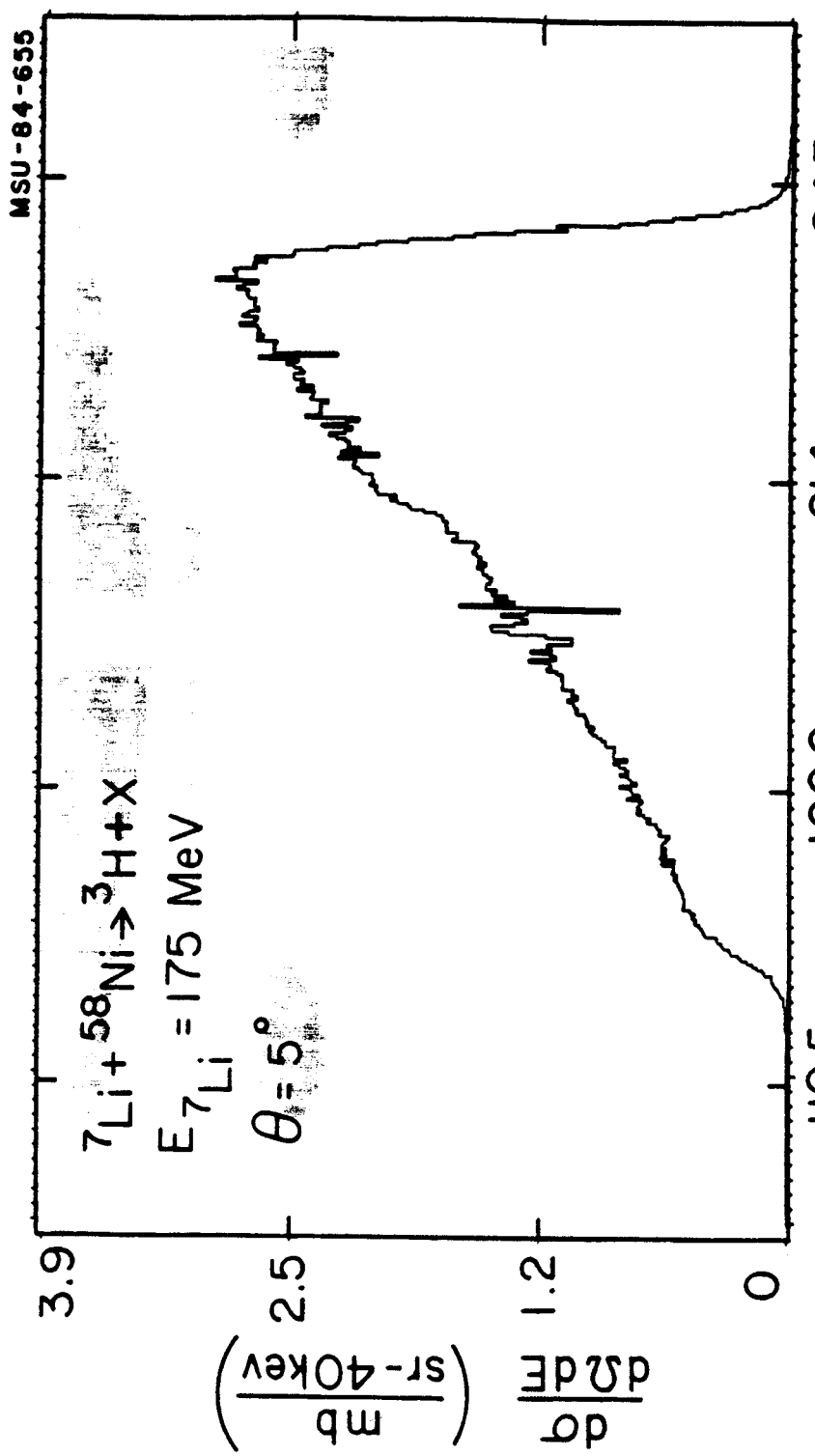

Figure 2-5: Triton energy spectrum for a typical run.

The apparent structure near E=107 MeV is due to roundoff errors in the position calculation since the triton energy loss in the proportional wires is very low and the signals were small. It might be interesting to investigate the mechanism which creates such large cross sections for tritons with velocities well above the beam velocity.

As seen in the particle ID spectra, the $^{7}Li^{+2}$ elastic peak also falls in the detector. We found the ratio between $^{7}Li^{2+}$ and $^{7}Li^{3+}$ at E_B= 175. MeV to be 9×10^{-5}. The elastic peak allowed the stability of the beam analysis system, cyclotron, and spectrograph to be monitored over the 3 days of the experiment. During long runs at constant dipole magnetic field, shifts of the order of 30 keV were observed. No evidence was seen for significant ^{12}C build up on the target, which would appear as a constant shift of the elastic peak.

2.2.5 Targets

The targets used were a 3.81(7) mg/cm^2 ^{58}Ni (99.93% enriched) target and a 3.03(6) mg/cm^2 ^{27}Al calibration target. The target thicknesses were determined by taking the weighted average of thicknesses determined by weighing and determined by the energy loss of α particles from a standard ^{241}Am α source. The α source measurement also showed that the targets were uniform to $\pm$0.04 mg/cm^2 over the region of the targets used in the experiment. To accurately determine the energy loss of the ^{7}Li and ^{8}He nuclei in the target material, it is not only necessary to

know the target thicknesses but also the stopping power of the target material. The standard technique is to obtain the stopping powers from tabulated values (Ho80,Zi80). To test the validity of the tabulated values for our energies and ions, we measured the relative energy loss between a 3.81(7) mg/cm^2 ^{58}Ni target and a 2.10(5) mg/cm^2 ^{58}Ni target for 173.4 MeV ^{7}Li and 145.0 MeV ^{6}He ions. Using the relative energy loss, we measured stopping powers of 0.140 MeV/mg/cm^2 for the ^{7}Li ions, and 0.062 MeV/mg/cm^2 for the ^{6}He ions. The tabulated values of Ziegler are 0.135 MeV/mg/cm^2 for the ^{7}Li ions and 0.051 MeV/mg/cm^2 for the ^{6}He ions. In extracting the experimental stopping powers a linear dependence on energy was assumed and the stopping powers quoted are for the average energy of the ion in the target. Due to the agreement, the tables of Ziegler were used in determining all target energy losses for this experiment.

1.2.6 Calibration

A critical ingredient in any mass measurement is the spectrograph focal plane calibration. The accuracy of the calibration will limit the accuracy of the mass determination. Depending on the experiment the absolute beam energy may also be a critical factor. In this experiment a 200 keV uncertainty in the beam energy (out of a total beam energy of 175 MeV) meant a 24 keV uncertainty in the mass. However this uncertainty could be larger if the calibration particle and the measurement particle have

significantly different energies with similar magnetic rigidities. In this experiment the functional dependence of position in the focal plane with energy is determined with $^{7}Li^{+2}$ elastic scattering by varying all magnetic fields in the spectrograph by a given percent change and recording the change in position. The absolute Q value scale is set by measuring a reaction with a known Q value, in this case $^{27}Al(^{7}Li,^{8}He)^{26}Si$. The beam energy is also determined with the ^{27}Al target by measuring the difference between the ^{26}Si g.s. and the $^{7}Li^{+2}$ elastic peak which is sensitive to the beam energy. The calibration can be checked by measuring a reaction with known excited states. In this case the calibration was checked by taking a spectrum from the reaction $^{58}Ni(^{7}Li,^{6}He)^{59}Cu$. The spectrum is shown in Figure 2-6. The measured energy levels are compared to known levels from an equivalent (^{3}He,d) reaction(Bi76). The comparison is shown in Table 2-2. The rms deviation of the known states to the measured ones is < 20 keV, which is adequate for this experiment. The measured mass excess for ^{59}Cu is also only ~20 keV from the expected value. This agreement in the measured mass excess is better than expected because it was necessary to lower the dipole magnetic field by ~1 kG to study the ($^{7}Li,^{6}He$) reaction. This usually introduces field scaling errors which would not be included in the calibration.

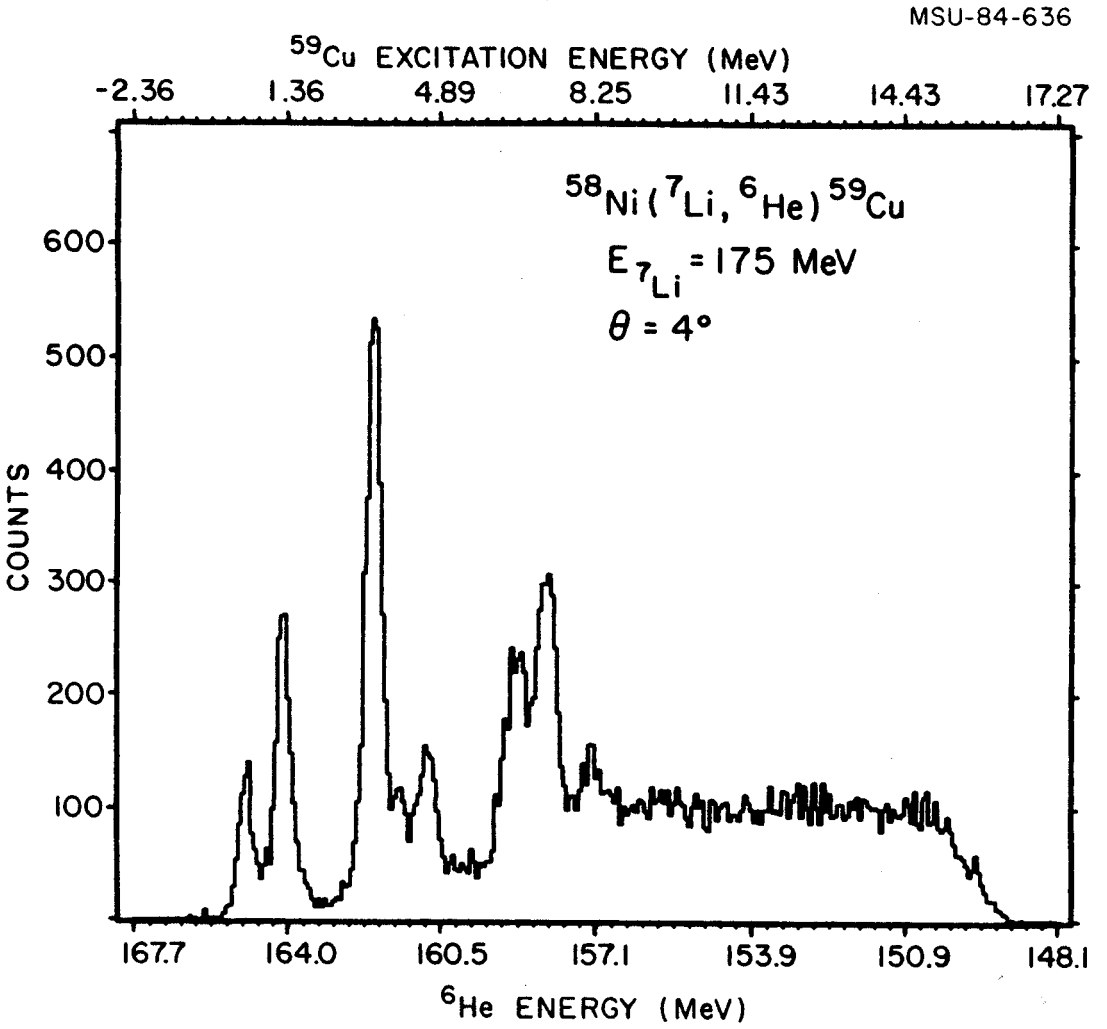

Figure 2-6: $^{58}Ni(^{7}Li,^{6}He)$ spectrum used as a check of the S320 focal plane calibration.

Table 2-2: Calibration comparison of levels measured with the $^{58}Ni(^{7}Li,^{6}He)$ reaction to those known from the $^{58}Ni(^{3}He,d)$ reaction.

B = 13.363 kG, θ = 4.0 deg:

$^{58}Ni(^{7}Li,^{6}He)^{59}Cu$	$^{58}Ni(^{3}He,d)^{59}Cu$ (Bi76)
0.0 MeV	0.0 MeV
0.896	0.913
3.031	3.047
4.330	4.307
6.203	6.202
6.945	6.937

The calibration calculations were carried out with the program CALIB. The general method is for the program to read an input file of calibration points, in this case elastic scattering, and to perform a polynomial fit of position in the focal plane, x, versus magnetic bend radius, ρ. A particle of given momentum, p, and charge q, will have a unique magnetic rigidity, Bρ. Hence given B, p, and q; ρ can be calculated and fitted versus x, which is measured. Once the fit has been performed, given any other x, ρ can then be determined. Then given B and q, the momentum and hence the energy of the particle can be determined. Using these techniques the program CALIB performs several options, including calculating the expected position for an ion from a given input reaction, excitation energy for a given channel number and reaction, and particle energy from a given channel number.

2.3 Results

The spectra obtained from the ^{58}Ni(^{7}Li,^{8}He)^{57}Cu reaction and the ^{27}Al(^{7}Li,^{8}He)^{26}Si calibration reaction are shown in Figure 2-7. The ^{57}Cu data is integrated over the angular range of 4 to 7 degrees, while the ^{26}Si data is from 5 degrees. The absence of counts below the lowest observed state in ^{57}Cu indicates good ^{8}He particle identification and a high purity ^{58}Ni target. Assuming the state at lowest excitation energy is the ^{57}Cu ground state, we measure a Q value of -29.564(54) MeV, which leads to a mass excess of ^{57}Cu of -47.35(5) MeV.

MSU-84-254

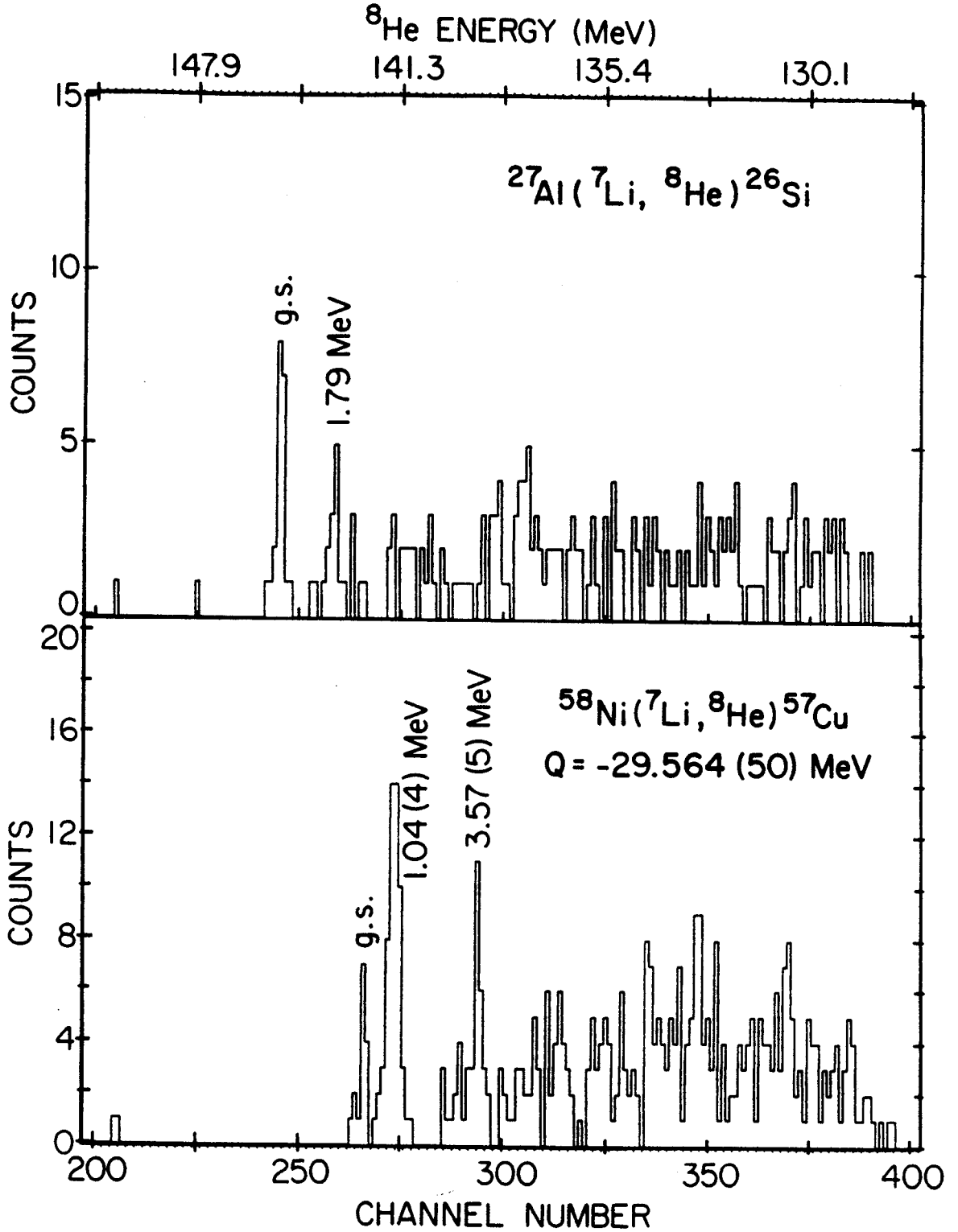

Figure 2-7: Position spectra for ^{8}He particles.

Table 2-3: Sources of uncertainty in the ^{57}Cu mass excess.

Parameter	Uncertainty in parameter	Mass Resolution (keV)
Target Thickness	2%	13.
Uniformity	1%	4.
Beam Energy	200 keV	24.
Angle	0.1 deg	9.
Statistics	^{26}Si g.s.	23.
	^{57}Cu g.s.	33.
Calibration		20.
		TOTAL 54.

(contributions added in quadrature)

The contributions to the uncertainty in the measurement are shown in Table 2-3. The primary uncertainty is from statistical uncertainties in the ^{26}Si g.s. and the ^{57}Cu g.s. centroids. These uncertainties added quadrature give 40 keV. The other two major sources of error are; 24 keV from uncertainty in the beam energy, and 20 keV from the uncertainty in the focal plane calibration. To obtain the final total uncertainty all effects were added in quadrature.

Figure 2-8 shows the measured levels of ^{57}Cu relative to its mirror nucleus, ^{57}Ni. The $1/2^-$ and the $5/2^-$ states are expected to lie within 50 keV of each other according to calculations of the displacement energies of these states and the structure of the mirror nucleus. The calculation is equivalent to treating the Coulomb force in first order perturbation theory and using the ^{57}Ni wave functions and energy levels as the unperturbed values. The calculations of the displacement energies reproduce quite well the trends in nearby nuclei and will be discussed in chapter 4 in connection with the Nolen-Schiffer anomaly. A statistical analysis of the peak at 1.04 MeV shows that its width is identical to that expected from the spectrograph resolution and the finite target thickness. However, a strong selectivity of the (^{7}Li,^{8}He) reaction for one of these states and not the other is not expected because the states are both single particle in composition.

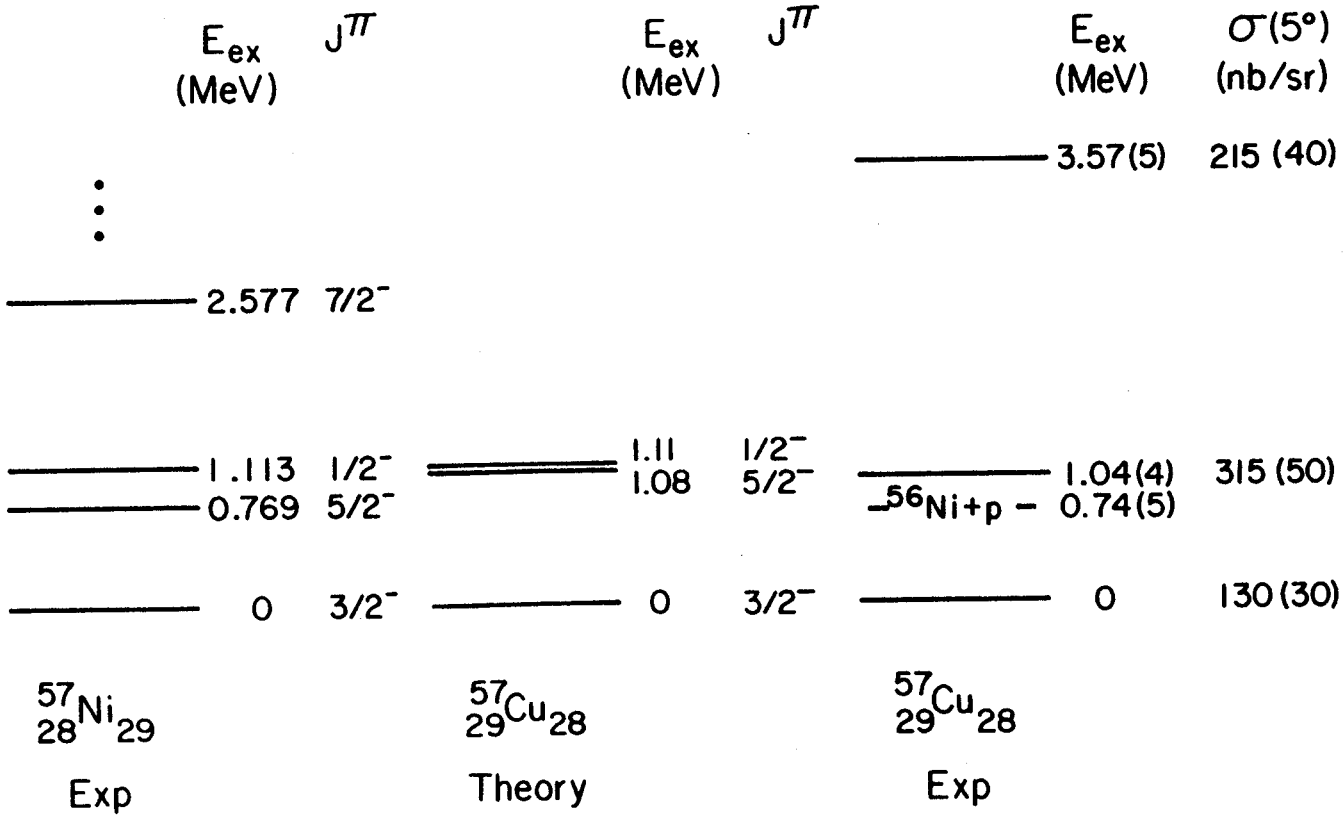

Figure 2-8: The level structure of ^{57}Cu along with the predicted structure based on pertubation theory and the structure of ^{57}Ni, mirror nucleus of ^{57}Cu.

Also, since the angular momentum mismatch between the incoming and outgoing particles is approximately 1.4 h, there should not be the selection of high spin states which is usually seen in heavy-ion reactions(Br72). Therefore we believe the $1/2^-$ and $5/2^-$ states both lie near 1.04(4) MeV excitation. It is possible, however, that only one of the states is populated, in which case the excitation of the other would be unknown. The quoted error of 40 keV for these states is included due to the uncertainty associated with the overlap of these states.

The limited angular distributions obtained for the measured states are shown in Figure 2-9. The error bars on the points reflect only the statistical uncertainties, $\sqrt{N}$, where N is the number of counts. Any systematic errors would shift the overall scale. No change in relative excitation is seen as a function of angle. In an attempt to understand the reaction mechanism two types of DWBA calculations were performed. First, since the low-lying states in ^{57}Cu are expected to be single particle states outside a ^{56}Ni core, one might hope to reproduce the results with DWBA calculations for the ^{56}Ni(^{9}Li,^{8}He)^{57}Cu reaction on the assumption that the l-transfer in this process will dominate the contributions from both the first step of this assumed route, ^{58}Ni(^{7}Li,^{9}Li)^{56}Ni, and all of the other possible reaction channels. These calculations were performed with the code SATURN-MARS (Ta74).

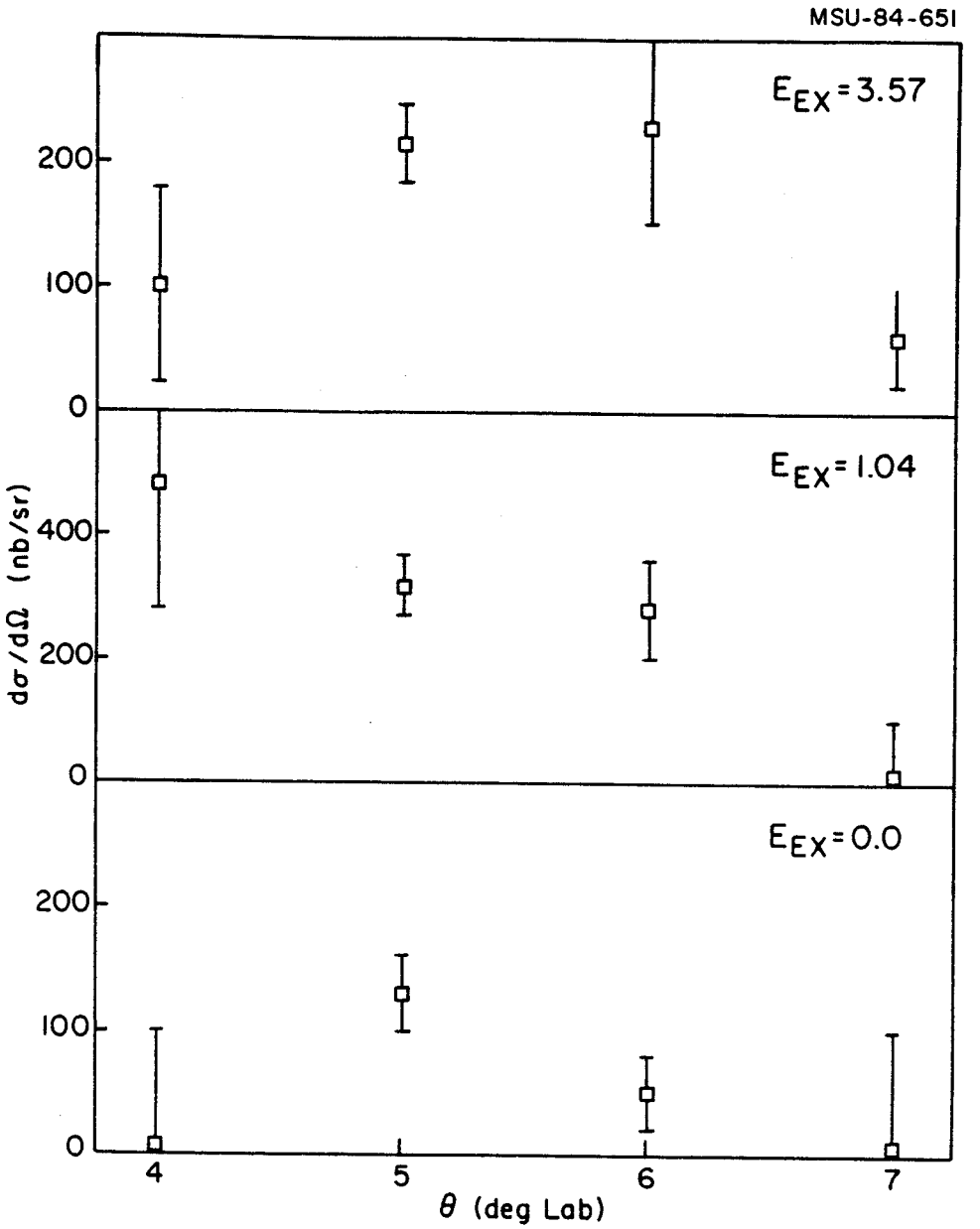

Figure 2-9: Angular distributions for the measured states in ^{57}Cu.

However, the predicted angular distributions did not match the data. In an attempt to determine if the reaction is more complicated, a sample two-step calculation assuming the simplest case of an l=0 two neutron pickup as the first step and the one proton stripping reaction as the second step, with the ground state of ^{56}Ni as the intermediate stage, were performed with the code SESIME (Pr76). Neither the relative magnitude of the cross sections for the observed levels or the angular distributions were reproduced. We conclude that the complexity of the (^{7}Li,^{8}He) rearrangement reaction, which is equivalent in quantum numbers to a Δ^{-} transfer from target to beam, makes it difficult to interpret in any simple way. We believe further study of the mechanism of the (^{7}Li,^{8}He) reaction would be interesting.

2.4 Comparison with Mass Models

2.4.1 Comparison

It is interesting to compare the measured mass excess to those predicted by the standard models. This comparison is shown in Figure 2-10. The predictions are taken from (Ma76). The error bars on the theoretical points represent the RMS deviation of the models with all known masses. The width of the line represents the uncertainty in this measurement.

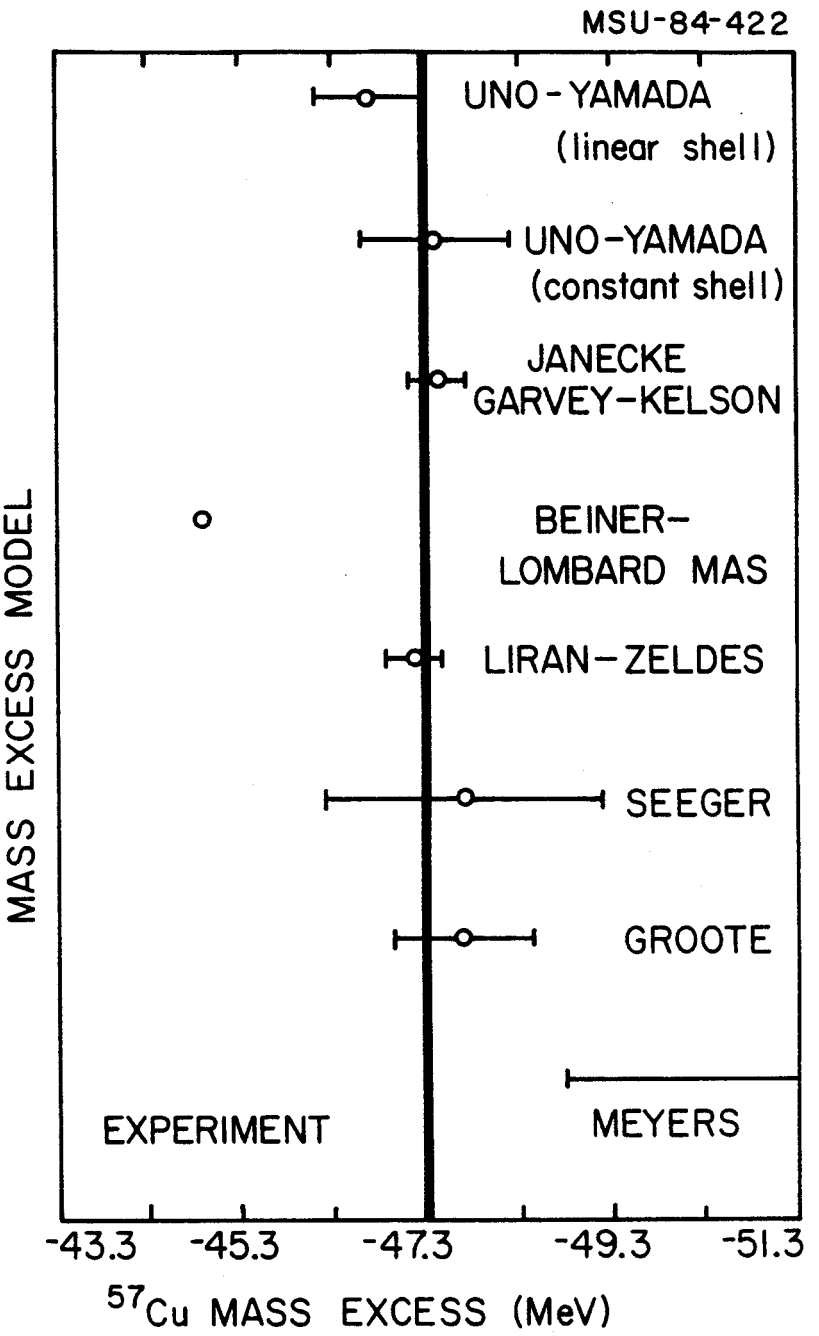

Figure 2-10: Comparison of the ^{57}Cu mass excess to various mass models.

The agreement indicates that the degrees of freedom in the models are sufficient to predict the ^{57}Cu mass excess. For a review of the various models see Maripuu (Ma76). Our measured mass excess also agrees with the β-endpoint measurement of Miyatake and Shinozuka (Mi83,Sh84a) of -47.36(13) MeV but has much better accuracy.

2.4.2 Garvey-Kelson Predictions

The mass excess of ^{57}Cu is also input into the Garvey-Kelson charge symmetric mass relation (Ke66). This mass relation is derived from the apparent charge independence of the nuclear force (charge independence will be discussed in detail in chapter 4). Hence the mass difference between analogue nuclei, $M(A,T=-T_z)$ and $M(A,T=T_z)$, is given by the Coulomb interaction. These Coulomb energies could be estimated from theoretical or phenomenological considerations or from a combination of each (see Ja68, or Chapter 4). Garvey and Kelson introduced a technique for evaluating the Coulomb energy and hence a method to predict the masses of proton rich nuclei provided the analogue neutron rich nucleus was known. The technique assumes a single particle model and determines the Coulomb energy for a proton in a given orbit by the difference between the mass excess of mirror nuclei with a valence particle in that orbit. Thus we write the the mass difference between analogue nuclei as

$$M(A,T_z=-T) - M(A,T_z=T) \approx \sum_{A'} [\, M(A',-1/2) - M(A',+1/2) \,] \quad (2.1)$$

where the sum runs over A' from A-(2T-1) to A+(2T-1) in steps of two. With this relation reliable predictions, with estimated errors of less than 100 keV, can be made for proton rich nuclei with N<Z (Ja68). Using the new data for ^{57}Cu, the mass excess predictions for lighter Cu isotopes are listed in Table 2-4. As shown in the table, ^{57}Cu is close to the predicted proton drip line.

2.5 Gamow-Teller Matrix Elements

2.5.1 Introduction

One interesting question which this new data may help answer is the goodness of the ^{56}Ni core. From the excitation spectra of ^{57}Ni it appears the energy gap between the f7/2 and 2p3/2 orbits is around 2.5 MeV. Thus, one might expect some admixture of the core in ^{57}Cu, but overall that ^{57}Cu is single particle in nature. A test is to use the known lifetime of ^{57}Cu and its mass excess to extract the ft-value for beta decay and hence the Gamow-Teller (G-T) matrix elements. These can be compared to those calculated in an extreme single particle model. Agreement would indicate a closed ^{56}Ni core. It must be noted however that exact agreement is not expected. Brown and Wildenthal have observed a quenching factor of 0.78 in s-d shell $\langle\sigma\tau\rangle$ values (Br83b).

Table 2-4: Garvey-Kelson charge symmetric mass predictions for Cu isotopes. Also shown are the one and two proton separation energies for these nuclei.

A	N	Z	Mass Excess	1 Proton Sep.	2 Proton Sep.
57	28	29	-47.35(5)	0.74	7.902
56	27	29	-38.614	0.574	5.183
55	26	29	-31.750	-0.176	3.688
54	25	29	-21.805	-0.316	2.083
53	24	29	-13.817	-1.570	0.975

The mechanisms for this quenching were studied by Brown and Wildenthal and also recently have been reviewed by Towner and Kahana (To83). We expect a similar quenching in the f-p shell.

2.5.2 Extraction of Measured Values

The G-T matrix elements can be extracted from experimentally measured lifetimes, branching ratios, and mass excess. This is true because the partial halflife for the β decay between an initial state $|i\rangle$ and a final state $|f\rangle$ is given by (see for example (Sh74))

$$t_{1/2} = C[(f_V + f_{EC})\langle\tau\rangle^2 + (f_A + f_{EC})(G_a/G_v)\langle\sigma\tau\rangle^2]^{-1}, \quad (2.2)$$

where $\langle\tau\rangle^2$ is the Fermi matrix and $\langle\sigma\tau\rangle^2$ is the Gamow-Teller matrix element. The Fermi matrix element for members of the same isospin multiplet can be expressed(Sh74) as

$$\langle\tau\rangle^2 = [\, T(T+1) - T_{Z_i} T_{Z_f} \,]\, \delta_{if}(1-\varepsilon) \quad (2.3)$$

where T is the total isospin and T_{Z_i} is the third projection. The factor $(1-\varepsilon)$ accounts for the reduction in the overlap between the initial and final state nuclear wave function due to isospin mixing. The ratio of the axial to vector β-decay coupling constants, G_a/G_v, is determined experimentally (Wi78) to be 1.251±0.009. The constants C and $(1-\varepsilon)$ are also determined experimentally(Wi78) to be C =

6170(4) and $(1-\varepsilon) = 0.997(3)$. The statistical rate factors f_V, f_A, and f_{EC} are for the vector, axial, and electron capture processes respectively. Given Q_β (Q_β= ME(parent) - ME(daughter)) for a transition f_A and f_V can be estimated using the parameterization of Wilkinson and Macefield(Wi74). In the cases studied in this thesis f_{EC} is small and will be ignored.

Table 2-5 lists the information known about the $^{57}Cu \rightarrow {}^{57}Ni$ β decay. The branching ratios and lifetime are not accurately known. The uncertainty in these quantities will dominate the calculated $\langle \sigma\tau \rangle$ values. Assuming a $3/2^- \rightarrow 3/2^-$ branching ratio of 96(3)% we find $ft = 5.3(4) \times 10^3$ and $\langle \sigma\tau \rangle^2 = 0.10(6)$. The branching for the $3/2^- \rightarrow 1/2^-$ decay was measured to be 3.7±1.7%, and no branching was observed for the $3/2^- \rightarrow 5/2^-$ transition. Based on shell model calculation one would expect ~1% branching to the $5/2^-$, and ~14% to the $1/2^-$, which is not consistent with the experimental values.

Table 2-5: Known properties of ^{57}Cu.

Mass excess = -47.35(5)

Lifetime = 233(16) msec

Branching ratios:

Transition	Branching ratio
$3/2^- \rightarrow 3/2^-$	96(3) %
$3/2^- \rightarrow 1/2^-$	3.7(1.7) %
$3/2^- \rightarrow 5/2^-$	?

2.5.3 Shell Model Predictions

To compare the experimental values with theory we first consider the extreme single particle model. In this model the ^{56}Ni core is assumed to be inert and only one particle in either the 2p3/2, 2p1/2, or 1f5/2 orbits changes isospin projection. With these assumptions it is possible to show(Br77a)

$$\langle\sigma\tau\rangle^2 = 6(2j_f+1)\begin{Bmatrix} 1/2 & 1/2 & 1 \\ j_f & j_i & l_f \end{Bmatrix}^2 \delta_{l_i l_f} \qquad (2.4)$$

where $j_f(l_f)$ and $j_i(l_i)$ are the final and initial total angular (orbital) momenta respectively. The results for the transitions considered here are shown in Table 2-5 and are labeled $\langle\sigma\tau\rangle_{sp}$. We find $\langle\sigma\tau\rangle_{sp}/\langle\sigma\tau\rangle_{exp} \approx 3.5$. This result is surprising because one would expect the single particle model to work best for nuclei with one particle outside a closed core, as in the case of ^{57}Cu and ^{57}Ni. To test if the origin of the discrepancy is in the single particle assumption one can compare shell model calculations including core excitations to the single particle value.

Shell model calculations using a given interaction and model space yield a series of wave functions Ψ^{NJT}, where N=A-Core, J is the total spin, and T is the total isospin. These total wavefunctions are constructed of linear combinations of the single particle states ρ^{nlj}, where the superscripts refer only to a single orbit. To perform the

shell model calculation the code OXBASH (Ra84) was used. The model space was the 2p3/2, 2p1/2, and f5/2 orbits and either 0, or 1 holes in the f7/2 core. From the calculated wave functions we extract the density matrix elements for one body operators; $[a^{\dagger}_{j_f} \otimes a_{j_i}]$ ($\sigma\tau$ in this case), coupled to $\Delta J = 1$ and $\Delta T = 1$. The operators $a^{\dagger}_j$ and a_j create and annihilate, respectively, nucleons in the shell model orbit j, where j denotes the single particle state ρ^{nlj}. The density matrix elements are given by

$$D_{j_i j_f} = (2\Delta J + 1)^{-1/2}(2\Delta T + 1)^{-1/2} \times \langle \Psi_f^{NJT} | | | [a^{\dagger}_{j_f} \otimes a_{j_i}]^{\Delta J=1, \Delta T=1} | | | \Psi_i^{NJT} \rangle \qquad (2.5)$$

The density matrix element contains all the shell model information. The total G-T matrix element is determined from

$$\langle \sigma\tau \rangle = [2(2J_i + 1))]^{-1/2} \begin{bmatrix} T_f & 1 & T_i \\ -T_{z_f} & \Delta T_z & T_{z_i} \end{bmatrix} \times \sum_{j_i j_f} D_{j_i j_f} S^{GT}_{j_i j_f} \qquad (2.6)$$

where

$$S^{GT}_{j_i j_f} = \langle \rho_f^{nlj} | | | \underline{\sigma} \cdot \underline{\tau} | | | \rho_i^{nlj} \rangle \qquad (2.7)$$

and the $|||$ bars represent reduction in both spin and isospin space. The single particle matrix elements, $S^{GT}_{j_i j_f}$,

were calculated with the program DENS (Br84), which also evaluates $\langle\sigma\tau\rangle$ after it reads the one-body transition density matricies output from OXBASH.

2.6 Discussion and Conclusions

The results of the calculations are shown in Table 2-6. The calculations assuming a closed ^{56}Ni core are labeled $\langle\sigma\tau\rangle_{cc}$, and those labeled $\langle\sigma\tau\rangle_{ph}$ assume up to one hole in the ^{56}Ni core. The interaction used in the shell model calculation was taken from VanHees(He81), and reproduces the low-lying excitations in fp shell nuclei. We see that although the shell model calculations give values for the G-T matrix elements which are closer to the measured value, they still are a factor of three high. As mentioned previously Brown and Wildenthal (Br78c,Br83b) have found that to reproduce the measured G-T matrix elements in the sd shell a renormalization factor of 0.6 (0.8 for $\langle\sigma\tau\rangle$ values) must be included in the single particle matrix elements. Even including this factor the discrepancy is large.

Table 2-6: Single particle and shell model $\langle\sigma\tau\rangle$ matrix elements for the $^{57}Cu \rightarrow {}^{57}Ni$, $^{29}P \rightarrow {}^{29}Si$, and $^{55}Ni \rightarrow {}^{55}Co$ β-decays compared with experiment.

Transition	$\langle\sigma\tau\rangle_{sp}$	$\langle\sigma\tau\rangle_{cc}$	$\langle\sigma\tau\rangle_{ph}$	$\langle\sigma\tau\rangle_{exp}$
^{57}Cu with VanHees interaction (He81):				
$3/2^- \rightarrow 3/2^-$	1.291	1.291	0.986	0.32(9)
$3/2^- \rightarrow 1/2^-$	1.155	1.155	0.737	0.25(6)
$3/2^- \rightarrow 5/2^-$	0.0	0.0	0.216	?
^{57}Cu with Mooy interaction (Mo83):				
$3/2^- \rightarrow 3/2^-$	1.291	1.291	0.869	0.32(9)
$3/2^- \rightarrow 1/2^-$	1.155	1.155	0.710	0.25(6)
$3/2^- \rightarrow 5/2^-$	0.0	0.0	0.140	?
^{29}P with Wildenthal interaction (Wi83):				
$1/2^+ \rightarrow 1/2^+$	1.732		0.515	0.440
		full space =	0.575	
^{55}Ni with VanHees interaction (He81):				
$7/2^- \rightarrow 7/2^-$	1.134		0.816	0.508(8)

The discrepancy is probably due to higher order configuration mixing in the ^{56}Ni core. However, this is unexpected because the amount of mixing is inversely proportional to the energy spacing of the levels in first order, and inversely proportional to the n^{th} order of the energy spacing in n^{th} order. Since the correction to the G-T matrix elements was small (see Table 2-6) including 2p-1h states, additional mixing, which would require 3p-2h configurations, should have an even smaller effect. One way to test this conjecture is to study a similar system where a complete shell model calculation is available. The full space calculation can be compared to the 2p-1h calculation to determine in additional mixing can explain the discrepancy. We have done this comparison for the decay of ^{28}P. We find that the 2p-1h calculation gives essentially the same result as the full space calculation. The $\langle\sigma\tau\rangle$ values are only 10% different. The calculated and experimental values for ^{29}P are listed in Table 2-6. We also see that the calculated values for the ^{29}P decay reproduce the 0.8 quenching factor expected. The agreement in the s-d shell indicates the additional quenching in the fp shell may be due to an inadequacy in the interaction of VanHees which was used to calculate the $\langle\sigma\tau\rangle$ values.

To check the interaction we have also included in Table 2-6 the calculated and measured (Ay84) values for the β-decay of ^{55}Ni. Again we see a quenching much stronger than the 0.78 expected, but not as large as the ^{57}Cu

quenching. Finally, as another check of the VanHees interaction, the interaction of Mooy (Mo83) was used to repeat the calculations. As shown in Table 2-6 the results are essentially identical. Since both interactions do a reasonable job in reproducing spectra and electromagnetic transition matrix elements, we would expect them to reproduce the Gamow-Teller matrix elements also. In any event such a large quenching is surprising.

The solution may be that the mechanism of the quenching is a function of A and is stronger in the heavier nuclei, although this is not expected (To83b). Another possibility is that mixing from higher-lying orbits, such as the g9/2 orbit, is contributing. Again considering the energy gap between the 2p3/2 and the g9/2 orbit, this seems very unlikely. It is also possible that the isospin mixing correction is much larger than the $1-\varepsilon = .998$ measured for lighter nuclei (Wi78). If we include the 0.7 renormalization factor, then we find $1-\varepsilon$ must be 0.48(8) to explain the measured ft value. Although one would expect some additional isospin mixing this value seems much too large, considering the largest mixing observed to date gives $1-\varepsilon \approx 0.997$ (Wi78). Presently this large discrepancy remains an interesting and unexplained problem. However due to the lack of an other suitable explanation, the discrepancy seems to be due to an inadequacy in the interaction used in the shell model calculations.

CHAPTER THREE

3.1 Introduction

The nucleus ^{59}Zn is the heaviest $T_z = -1/2$ nucleus for which the mass and lifetime are known (Sh83,Ar84). For this reason its properties are important data for mass predictions (Ke66), studies of Gamow-Teller (G-T) transitions in fp shell nuclei (Ar81,Ar84,Ho81a), and understanding the effects of the Coulomb force in nuclei (Sh83). In particular this nucleus extends the data base for studying the Nolen-Schiffer anomaly (see chapter 4) to the A = 59 mirror pair. With the mass measurement of ^{59}Zn, the A = 59 pair is the heaviest mirror pair with both mass excess known. In this chapter we will review the information previously known on ^{59}Zn, discuss the experimental details of the ^{58}Ni(p,π^-)^{59}Zn reaction used to study ^{59}Zn, and then discuss the implications of the results for mass models and G-T transitions in the fp shell as was done for ^{57}Cu. The implications for the Nolen-Schiffer anomaly will be discussed in chapter 4. When the ^{58}Ni(p,π^-)^{59}Zn reaction was studied an attempt to measure

the $^{40}Ca(p,\pi^-)^{41}Ti$ reaction was also made, and will be discussed at the end of the chapter. We were unable to observe the ^{41}Ti ground state, which has implications on the closed core nature of ^{40}Ca.

The nucleus ^{59}Zn has been observed twice previously. The first observation(Ho81a) was performed at the University of Jyväskylä MC-20 cyclotron. The ^{59}Zn nuclei from the $^{58}Ni(^3He,2n)^{59}Zn$ fusion-evaporation reaction were separated with a He-jet system and the β-decays observed with a Ge(HP) detector. They measured a ^{59}Zn β halflife of 210±20 msec, with the branching ratios shown in Table 3-1. No information was obtained on the mass excess of ^{59}Zn. The second measurement was performed at the University of Tohoku Cyclotron Facility. The ^{59}Zn nuclei were also created via the $^{58}Ni(^3He,2n)^{59}Zn$ reaction but in this case were separated with the Tohoku Isotope Separator On-Line (ISOL)(Fu81). They found a β halflife of 182.0±1.8 msec. The measured branching ratios are also shown in Table 3-1. They were able to extract a ^{59}Zn mass excess by studying the endpoint of the β energy distribution. They deduced a mass excess of -47.23(10) MeV.

3.2 Experimental

As noted in the introduction, Q value measurements of direct reactions usually provide a better technique for measuring the mass and level structure of an unknown nucleus than studying β-decay.

Table 3-1: Branching ratios for the $^{59}Zn \rightarrow ^{59}Cu$ β decay.

Transition	B (%)	
	(Ar84)	(Ho81)
$3/2^- - 3/2^-$	94.1 ± 0.7	93 ± 3
$3/2^- - 1/2^-$	4.8 ± 0.6	5 ± 2
$3/2^- - 5/2^-$	1.1 ± 0.2	1.6 ± 0.8
	Lifetime (msec)	
	182 ± 1.8	210 ± 20
	Branching ratio to proton unbound states	
	$9 \pm 2 \times 10^{-4}$	$2.3 \pm 0.8 \times 10^{-3}$

However in the case of ^{59}Zn the lack of suitable targets and multinucleon transfer reactions makes its study via Q value measurements difficult. Thus, the ^{58}Ni(p,π^-)^{59}Zn reaction was performed at the Indiana University Cyclotron Facility (IUCF) to measure the mass excess of ^{59}Zn and its low-lying level structure. The experiment was done at IUCF because the large Q value of the reaction, Q=-144.7 MeV, required a large proton energy (at least 150 MeV). Also the IUCF coupled cyclotrons are capable of producing several μA of beam current. Finally, IUCF has a QQSP spectrometer optimized for pion detection(Gr82). This measurement was the first use of the (p,π^-) reaction to measure a nuclear mass. Previously the reaction was used to study 1p-2h states in nuclei(Vi82).

3.2.1 The QQSP Spectrometer

The QQSP spectrometer was set at 30 degrees. At the focal plane of the spectrometer a vertical drift chamber detector measured both position and angle(Gr83). Figure 3-1 shows the spectrograph and detector layout. The standard setup, which is described by Green (Gr83), uses time of flight between the scintillators and between the front scintillator and the rf of the cyclotron to eliminate background from other particles, particularly electrons. In the present experiment an aluminum absorbing wedge was placed after the focal plane detector and before the scintillators.

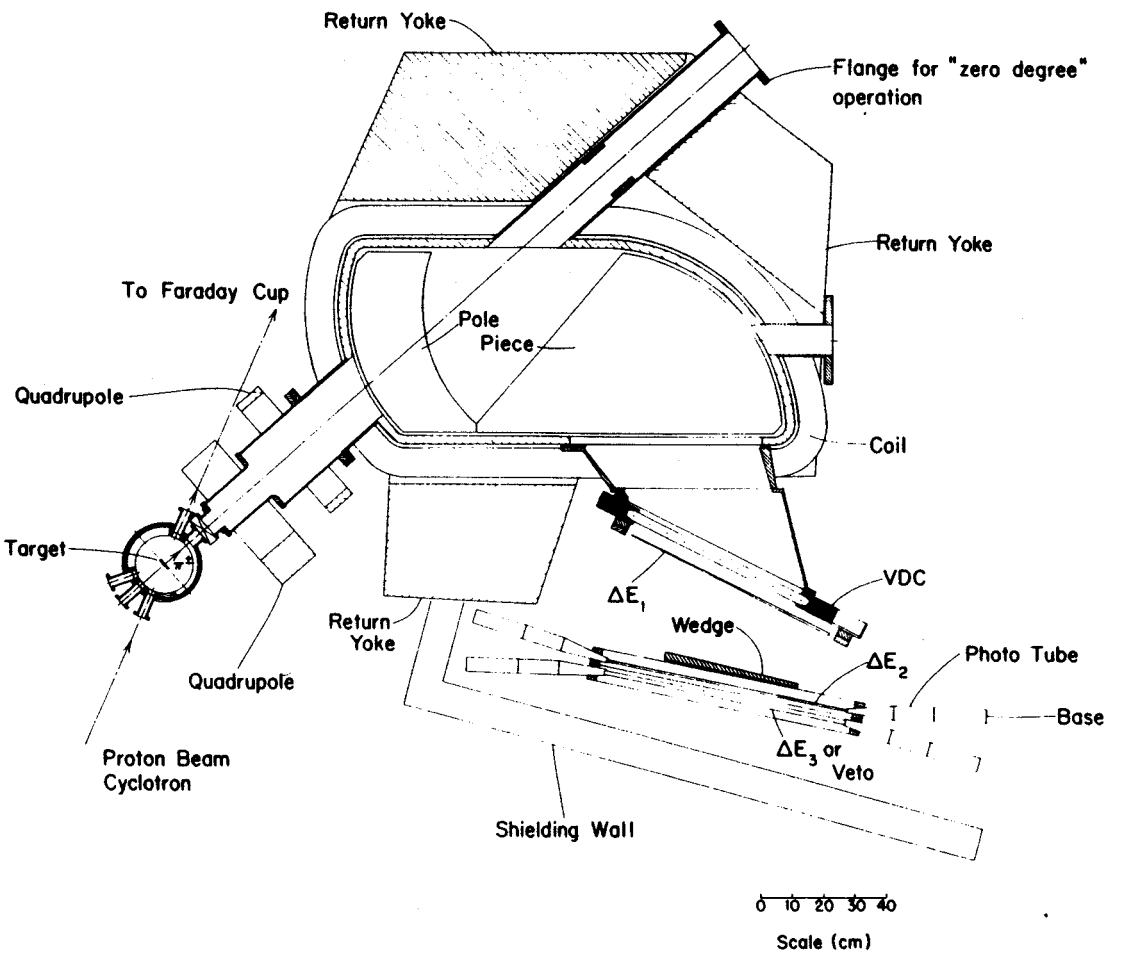

Figure 3-1: The QQSP spectrometer.

The thickness of the wedge was chosen to cause the negative pions to stop in the last scintillator, where they deposited some part of their rest mass energy plus their kinetic energy. Thus by gating on large (ΔE_2 > 40 MeV) energy signals in the ΔE_2 scintillator, we were able to reduce the background by two orders of magnitude from the standard setup without changing the efficiency. The limitation of this technique is that it works for only a limited range of pion energy due to the geometry of the wedge and the pion orbits in the spectrograph.

3.2.2 Calibration

The mass measurement itself was carried out by determining the Q value of the reaction $^{58}Ni(p,\pi^-)^{59}Zn$ relative to the Q values of the calibration reactions(Wa84)

$$^{13}C(p,\pi^-)^{14}O \quad Q = -136.650 \text{ MeV}$$

$$^{25}Mg(p,\pi^-)^{26}Si(1.796 \text{ MeV}) \quad Q = -140.595 \text{ MeV}$$

$$^{25}Mg(p,\pi^-)^{26}Si(2.783 \text{ MeV}) \quad Q = -139.607 \text{ MeV}$$

Since the QQSP measured angle as well as position, the angular resolution of the detector permitted the division of the ^{14}O calibration data into 11, 0.9 degree angular bins. The reaction kinematics made the outgoing pion energy a function of angle, hence the angular bins gave a calibration point every channel in the region of the ^{59}Zn ground state and provided a precise calibration of spectrograph focal plane.

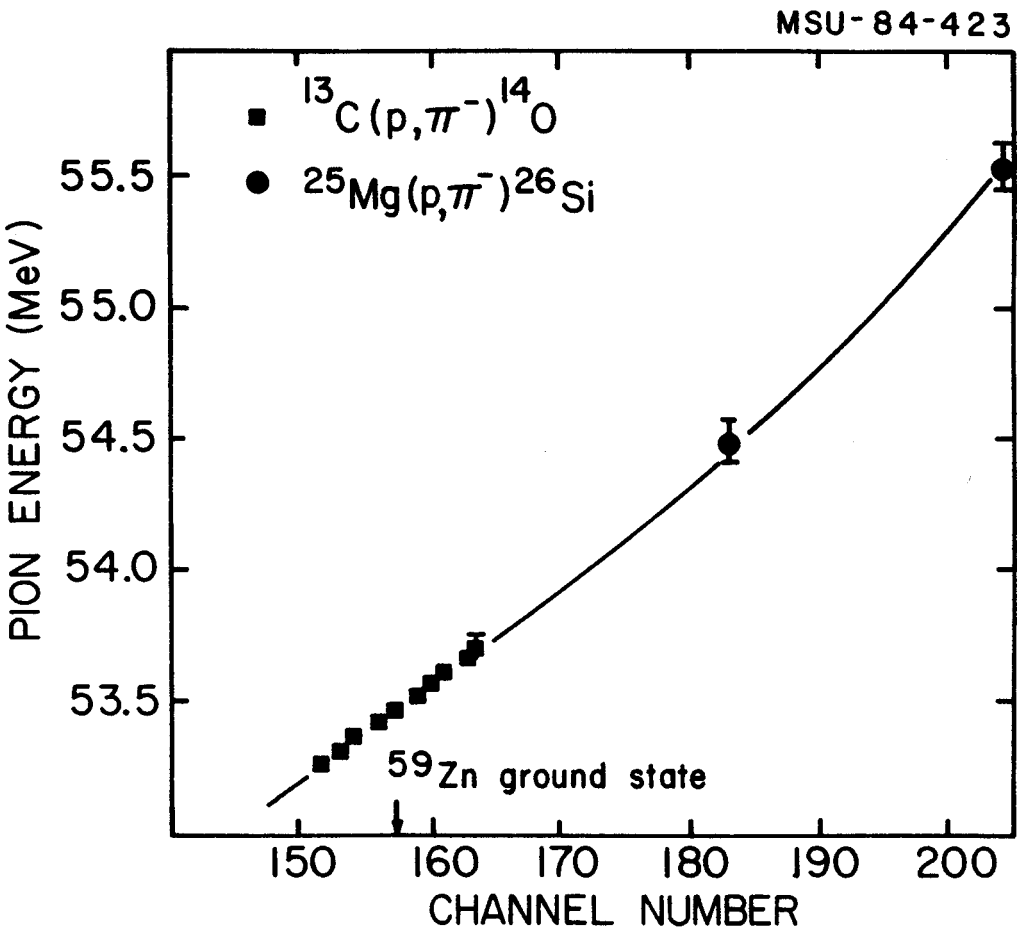

Figure 3-2: The QQSP focal plane calibration.

The calibration data are shown in Figure 3-2. Several corrections were applied to the measured centroids of these data. The data-analysis and display program RACHEL(We76,Gr82) corrects for reaction kinematics taken from an input reaction. In our case we required all data to be analysed as if it were from the $^{58}Ni(p,\pi^-)^{59}Zn$ reaction. However the calibration reactions have somewhat larger kinematic corrections because the targets are lighter. Thus the pion energy for a given angle from a calibration reaction must be corrected for the difference between the kinematics of the calibration reaction and the (p,π^-) reaction from the ^{58}Ni target. The kinematic corrections were calculated with the program SPECKINE9 (Be83). A further correction was the effect of the different target thickness for the ^{58}Ni, ^{13}C, and ^{25}Mg. However, the target thickness (21.5 mg/cm^2 ^{13}C, 28.5 mg/cm^2 ^{58}Ni, and 26.3 mg/cm^2 ^{25}Mg) were chosen so the energy loss corrections were the same in each target, within 14 keV, for the reactions studied. Finally, the ^{13}C calibration data were taken at 10 hour intervals. Between calibrations shifts of less than one channel were observed. These shifts were probably due to instabilities in the QQSP dipole power supply. All data was corrected for the observed shifts.

3.2.3 Cross Section Corrections

To extract (p,π^-) cross sections it was necessary to correct for the π^- decays in flight. The fraction of remaining pions after a time t is given by

$$N = e^{-t / \lambda_{\pi}} \qquad (3.1)$$

where $\lambda_{\pi} = \gamma \lambda_{\pi}^{o}$, λ_{π}^{o} is the mean pion lifetime,

$$\gamma = (1 - \beta^{2})^{-1} \qquad (3.2)$$

with $\beta = v_{\pi} / c$, and v_{π} is the pion velocity. The mean flight path in the QQSP is 2.0 m, and the pion kinetic energy is 53.5 MeV (γ = 1.36), hence the fraction is N = 0.764 .

3.3 Results

The Q value for the ^{58}Ni(p,π^{-})^{59}Zn reaction was measured to be Q = -144.735(40) MeV, which gave a mass excess of ME(^{59}Zn) = -47.256(40) MeV. The measured cross section was 0.080(20) nb/sr. This mass excess agrees with the β-endpoint measurement made by Arai et al.(Ar81) of ME(^{59}Zn) = -47.23(10) MeV. The weighted average of the two measurements is ME(^{59}Zn) = -47.253(37) MeV. The experimental spectrum is shown in Figure 3-3 along with a calibration spectrum. The ^{58}Ni target data are integrated over the whole angular range, whereas the ^{13}C spectrum is shown for one of the 0.9 degree angular bins.

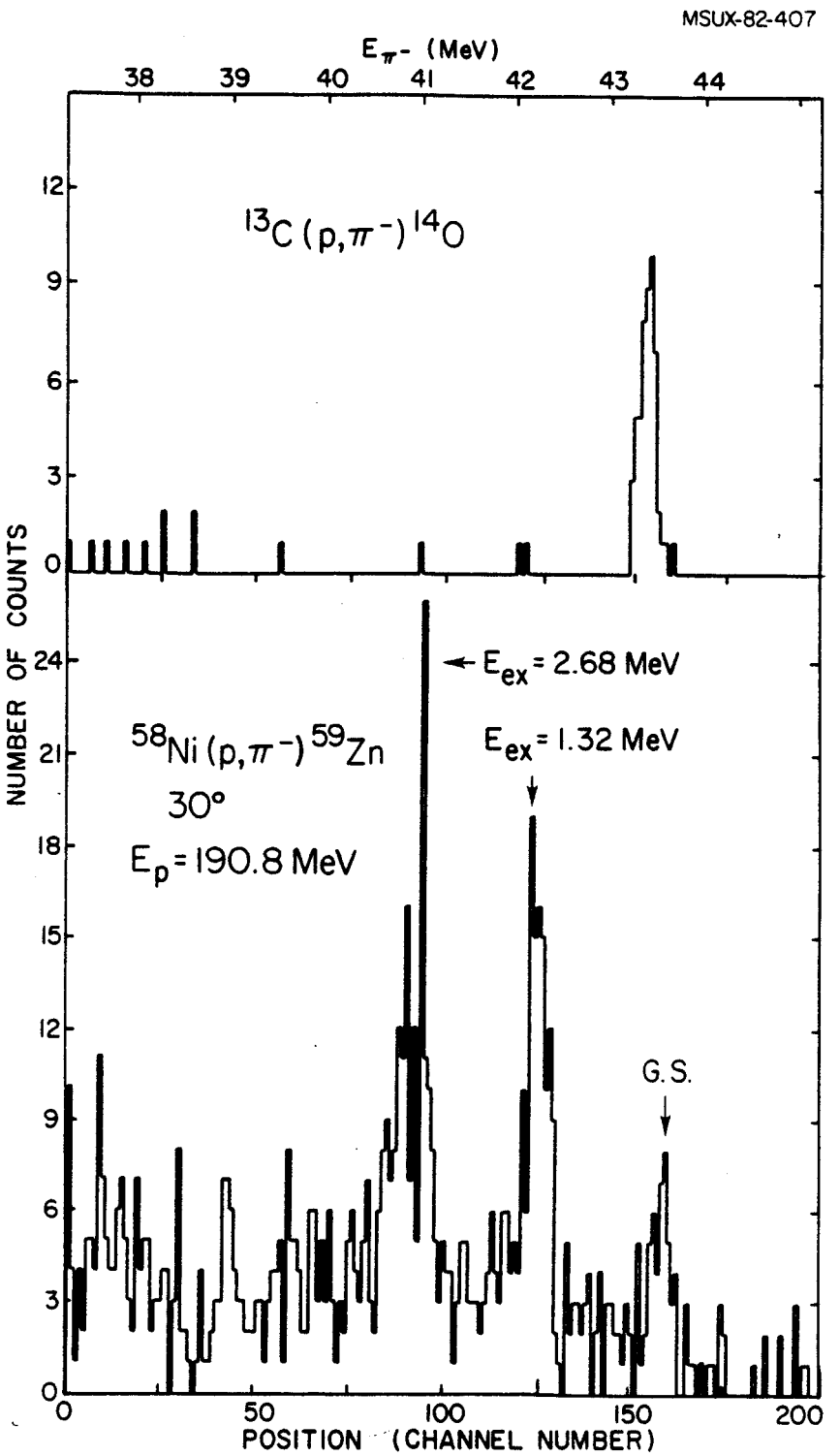

Figure 3-3: Pion position spectra for the ^{59}Zn mass measurement and one angular bin of the ^{14}O calibration run.

The uncertainty in the mass measurement of ^{59}Zn came from four sources. First, the difference in reaction kinematics between ^{58}Ni(p,π^-) and the calibration reactions ^{13}C(p,π^-) and ^{25}Mg(p,π^-) coupled to a 0.5 degree uncertainty in spectrograph angle lead to a 20 keV systematic uncertainty in the mass measurement. Second, the absolute beam energy was uncertain by 200 keV. This lead to a 4 keV uncertainty, again due to the difference in reaction kinematics. Third, observed shifts in calibration data were of the order of 80 keV. Thus, although the ^{59}Zn runs were shifted and summed according to the observed shifts in the calibration spectra, we conservatively estimate that this fluctuation introduced a 20 keV systematic uncertainty into the mass measurement. Finally, poor statistics, due to the small ^{58}Ni(p,π^-) cross section and the uncertainty in background subtraction, lead to a 28 keV centroid uncertainty. All other contributions to the uncertainty were determined to be less than 4 keV. For the final total uncertainty all effects were added in quadrature.

The measured low-lying level structure of ^{59}Zn is shown in Figure 3-4. Also shown is the level structure of ^{59}Cu (Le78), mirror nucleus of ^{59}Zn. The cross sections are consistent with the observation that the (p,π^-) reaction selects high spin states due to the large pion-proton momentum mismatch (Br83a).

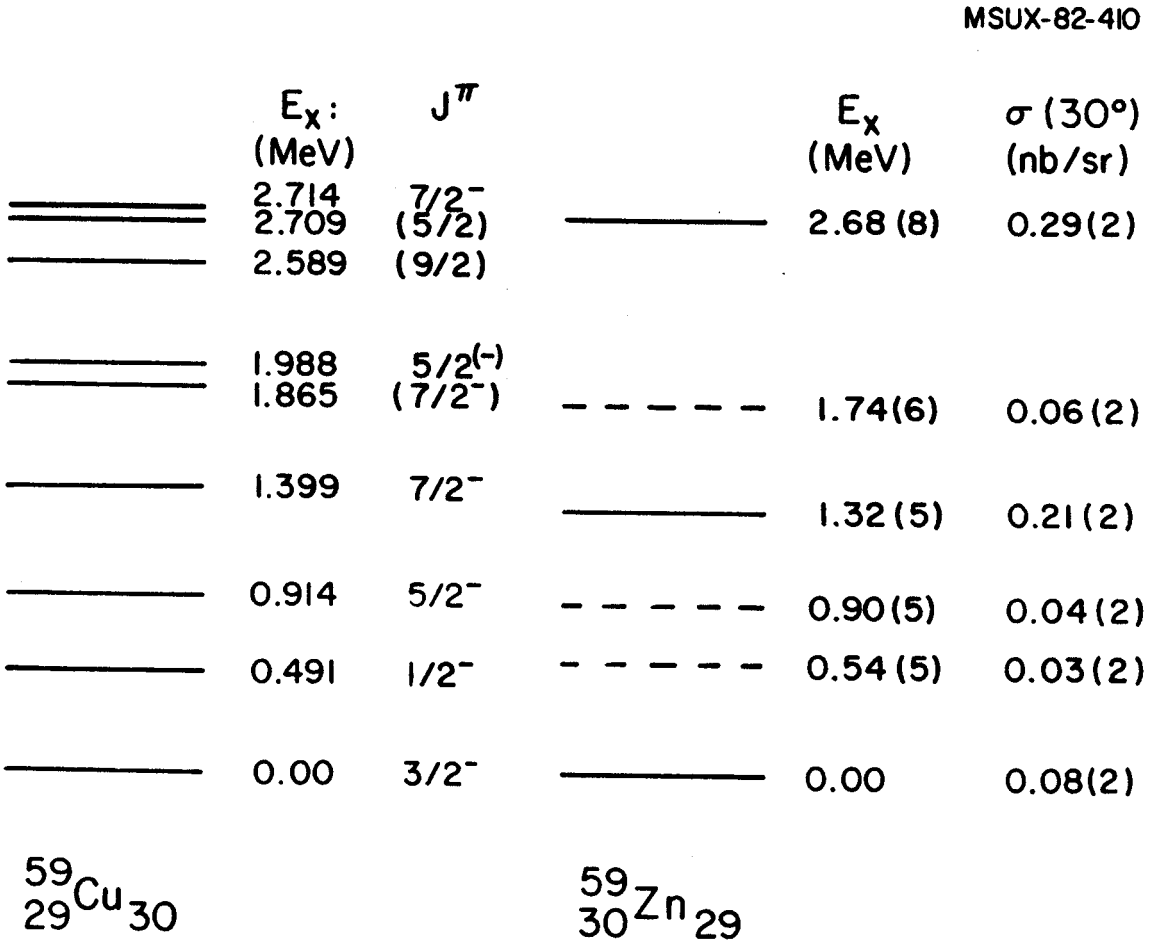

Figure 3-4: Excitation spectra for ^{59}Zn and its mirror nucleus ^{59}Cu.

We also attempted to measure the mass of ^{41}Ti with the reaction ^{40}Ca(p,π^-), but no counts were observed above the background. This lack of yield gives an upper limit for the cross section of 0.003 nb/sr.

3.4 Comparison to Mass Models

3.4.1 Comparison

The first simple test which can be performed with any new mass excess measurement is to check the results against the predictions from various models. Figure 3-5 shows the comparison to the standard models(Ma76). The width of the line labeled experiment indicates the uncertainty in the measurement. The error bars on the theory represent the rms deviation of the various theories from known masses. In general the agreement is very good. There is a large disagreement with the prediction by Myers (My76). This however is not surprising because this model is based on the liquid drop model in which only 4 free parameters were used to fit the approximately 1000 known masses. The general agreement indicates that no new degrees of freedom, such as deformation in the nuclear shape, are occurring in this region of the isotope table. The measurement of several more lighter Zn isotopes would be necessary to make a detailed study of the systematic discrepancies with the model mass predictions.

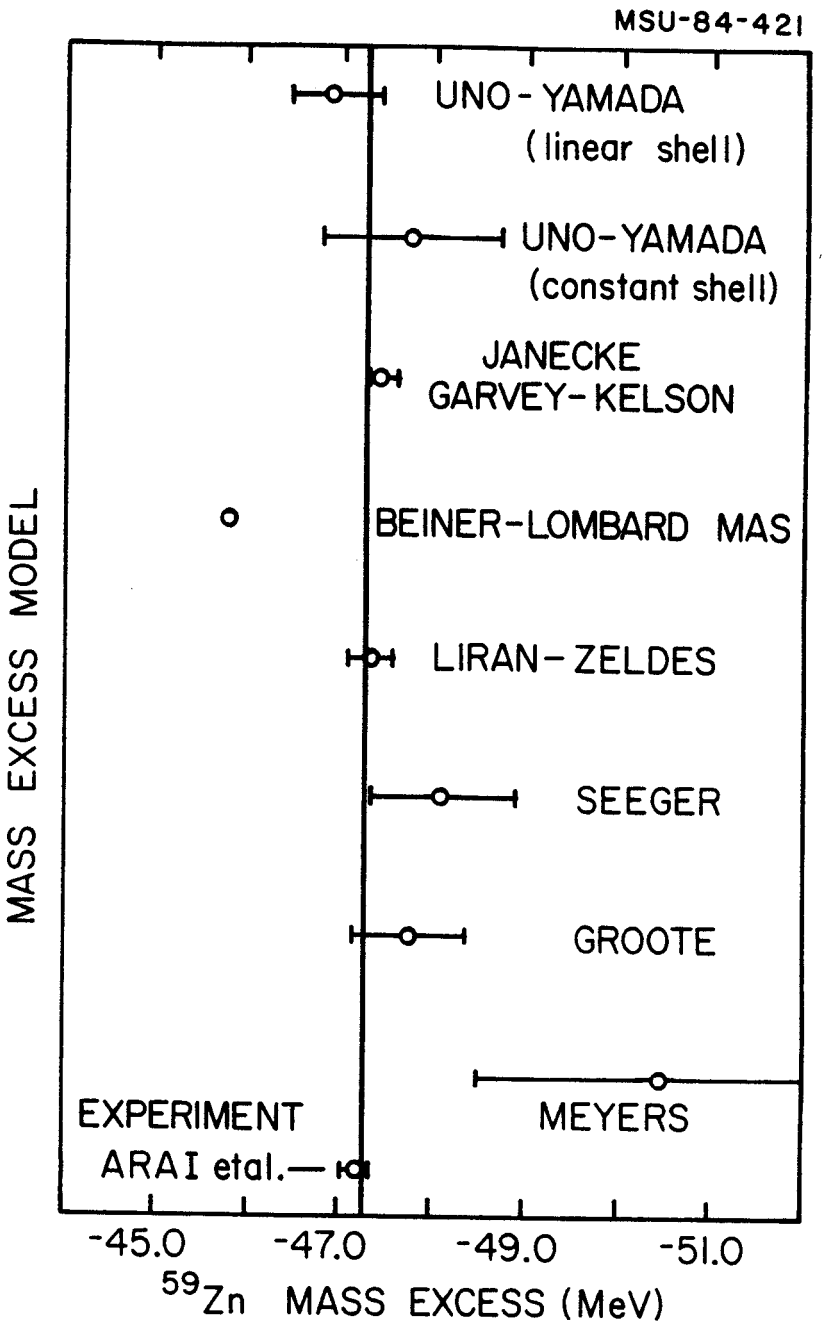

Figure 3-5: Comparison of the ^{59}Zn mass excess to various mass models.

3.4.2 Garvey-Kelson Predictions

The mass excess of ^{59}Zn is also input in to the Garvey-Kelson charge symmetric mass relation (Ke66). The justification and description of this mass relation were described in Chapter 2. Table 3-2 show the Garvey-Kelson predictions for proton rich Zn isotopes. It is interesting that the Zn isotopes are predicted to be stable out to ^{54}Zn, which is 10 neutrons from the the first β-stable Zn isotope, ^{64}Zn.

3.5 Gamow-Teller Matrix Elements

Gamow-Teller (G-T) matrix elements have been studied extensively in the s-d shell, and it was found that a renormalization of 0.6 is required to fit the known G-T β-decay lifetimes(Br78c,Br83b). The ^{59}Zn data allows us to further study the G-T matrix elements in the f7/2-2p3/2-2p1/2-f5/2 shell to see if a similar renormalization in required. For the ^{57}Cu→^{57}Ni β decays a much larger quenching was observed. It is interesting to see if this large reduction in $\langle\sigma\tau\rangle$ is present in other f-p shell G-T transitions. The data on the ^{59}Zn β-decay provide useful information for such a systematic study.

Table 3-2: Garvey-Kelson charge symmetric mass predictions for Zn isotopes. Also listed are the one and two proton separation energies for these nuclei.

A	N	Z	Mass Excess	1 Proton Sep.	2 Proton Sep.
58	28	30	-42.431	2.370	3.107
57	27	30	-32.852	1.527	2.100
56	26	30	-25.810	1.349	1.178
55	25	30	-14.894	0.378	0.062
54	24	30	-6.397	-0.131	-1.701

3.5.1 Measured Values

To extract the G-T matrix elements it is necessary to know the ^{59}Zn lifetime and branching ratios in addition to the ^{59}Zn mass excess. These measurements have been performed, and the results were given at the beginning of this chapter. Using the new ^{59}Zn mass excess we are able to obtain a more accurate ft value and hence are able to extract a more accurate G-T matrix element.

The ft values for the β^+ decay of ^{59}Zn have been calculated previously (Ho81a,Ar84). Using the new mass of ^{59}Zn, we obtained a more accurate value for the decay to the ground state ^{59}Cu. The statistical rate function f was calculated, according to the method of Wilkinson and Macefield (Wi74), to be $f = 2.61(6)\times10^4$. The error in f is due to the uncertainty of the ^{59}Zn mass. Using the weighted average of the lifetime and branching ratios (Ar84,Ho81a) we obtain ft = 5048(131). Using these results and the method described in section 2.5 of this thesis we deduce the ft values and G-T matrix elements for the ^{59}Zn β-decay. The results for the $3/2^- \rightarrow 3/2^-$, $3/2^- \rightarrow 1/2^-$, and $3/2^- \rightarrow 5/2^-$ transitions are shown in Table 3-3.

3.5.2 Shell Model Calculations

The G-T matrix elements are calculated from the extreme single particle model, $\langle\sigma\tau\rangle_{sp}$, and a shell model using the interaction of VanHess(He81) assuming a closed ^{56}Ni core, $\langle\sigma\tau\rangle_{sh}$. As in the case of ^{57}Cu decay the measured G-T matrix elements are a factor of 3 lower than

the calculated values. Arai commented that this reduction may be due to the assumption of a closed ^{56}Ni core(Ar84). To test this conjecture we repeated the shell model calculation allowing one hole in the f7/2 orbit of the ^{56}Ni core. The results are show in table 3-2 under $\langle\sigma\tau\rangle_{ph}$. While some reduction in the discrepancy between calculated and measured G-T matrix elements is seen, there is still more than a factor of two disagreement.

3.5.3 Discussion and Conclusions

The results of this section are consistent with the large reductions in the G-T matrix elements observed in ^{57}Cu β decay. As noted in chapter 2, the reduction may be due to configuration mixing of higher order, or an inadequacy in the model space interaction.

3.6 Conclusions

The failure to observe the ground state of ^{41}Ti in the reaction ^{40}Ca(p,π^-)^{41}Ti is evidence for the closed core nature of ^{40}Ca. If ^{40}Ca had a large 2p-2h component, then this cross section would be similar to the ^{48}Ca(p,π^-)^{49}Ti cross section scaled by a factor of 7/2 to include the extra neutrons present in the f7/2 shell in ^{48}Ca.

Table 3-3: Measured vs. calculated $\langle \sigma\tau \rangle$ matrix elements for ^{59}Zn β-decay.

E_f(keV)	Transition	exp	sp	$\langle \sigma\tau \rangle_{shell}$	sh(1h)
0	$3/2^- \rightarrow 3/2^-$	0.39±0.06	1.291	0.965	0.690
491	$3/2^- \rightarrow 1/2^-$	0.23±0.02	1.155	0.817	0.491
914	$3/2^- \rightarrow 5/2^-$	0.13±0.02	0	0.113	0.282

The absence of any observed counts near the expected ground state sets an upper limit of about 25% for the 2p-2h neutron contribution to the ^{40}Ca wave function.

Due to the low cross section and lack of suitable target there are not many uses for the (p,π^-) reaction in mass measurements. Two remaining possibilities are $^{64}Zn(p,\pi^-)^{65}Ge$ and $^{92}Mo(p,\pi^-)^{93}Ru$. Many more proton rich nuclei could be reached with the $(^3He,\pi^-)$ reaction, but the ground state cross sections are expected to be even smaller than for (p,π^-) due in part to an even worse momentum mismatch.

CHAPTER FOUR

4.1 Introduction

The concept of a mirror pair of nuclei implies a symmetry in nuclear structure with respect to the interchange of neutrons and protons. Since the proton rich members of the A=57 and A=59 mirror pairs have been measured as part of this thesis, it is interesting to use these results to study mirror symmetry and the resulting implications for nuclear structure and the nuclear force. Figures 2-8 and 3-4 demonstrate the similarities in the excited states of the members of the A=57 and A=59 mirror pairs. Many other mirror pairs are known with A<57, and in all cases the excitation spectrum of both members is similar. The nuclear structure appears to be independent of the interchange of all neutrons and protons.

The symmetry in mirror systems was formulated by Heisenberg(He32) with the introduction of the quantum number of isospin. In this picture the proton and the neutron are different isospin projections of the nucleon. The standard convention in nuclear physics is to define

$$t_3|p\rangle = -1/2|p\rangle \qquad (4.1), \text{ and}$$

$$t_3|n\rangle = +1/2|n\rangle \qquad (4.2)$$

where $|p\rangle$ and $|n\rangle$ are the proton and neutron wavefunctions and t_3 is the third component of the full isospin operator T. Isospin independence of the nuclear force can be stated as

$$[H,T] = 0 \qquad (4.3)$$

where H is the nuclear Hamiltonian. If 4-3 is valid, then nuclei with the same A and same T will have identical energy levels, as has been noted in mirror systems. However, since H contains a contribution due to the Coulomb force between protons, which will not commute with T, it is useful to write

$$H = H_N + V_C \qquad (4.4)$$

where H_N is the Hamiltonian due to the nuclear force, and V_C is the Hamiltonian due to the Coulomb force. Since in general $H_N >> V_C$, V_C is treated in pertubation theory or simply ignored. V_C can be interpreted as the cause for the slight differences in structure in mirror pairs. Figure 2-8 demonstrates the effect of V_C. If one starts with the nucleus ^{57}Ni and calculates the effect due to the Coulomb force by changing one neutron into a proton, one predicts

the level structure shown as $^{57}Cu^{THY}$, which agrees with the measured nature of ^{57}Cu. Excluding the effect of V_C the requirement for charge independence is then

$$[H_N, T] = 0 \qquad (4.5)$$

A lesser restriction on H_N is charge symmetry, which is written as

$$[H_N, P_C] = 0 \qquad (4.6)$$

where $P_C = e^{-i\pi T_2}$, $T_2 = \sum_i t_2(i)$ where i runs over the nucleons in the nucleus. The effect of these symmetries on the nuclear potentials V, for nucleons acting in the T=1 state, are for charge independence to require

$$V_{nn} = V_{pp} = V_{pn} \qquad (4.7),$$

and for charge symmetry

$$V_{nn} = V_{pp} \neq V_{pn} \qquad (4.8).$$

The notation used is that V_{nn} is the potential between a pair of neutrons, V_{pp} is the potential between a pair of protons, and V_{pn} is the potential between a proton-neutron pair. It is charge symmetry which is involved in mirror

systems because the number of pn interactions does not change.

4.2 Tests for Charge Asymmetry

One technique for testing charge independence and charge symmetry is to measure the nn, np, and pp scattering lengths, written as a_{nn}, a_{pp}, and a_{pn}. Recently measured values of these scattering lengths are summarized in Table 4-1. These values show evidence for charge independence breaking for T=1 states but within errors no evidence for charge symmetry breaking. The breaking of charge independence implied by this data can be understood as a consequence of the $\pi^{\pm}$ and π^{0} mass difference and second order mesonic effects in the NN force (Sh78,He79). The errors in the measurements of a_{nn} and a_{pp} must be reduced before definite statements can be made on charge asymmetry. The relatively large error bars are due to the difficulty in performing and analyzing the nn scattering experiments(Ga81,Fe81) and the difficulty in subtracting the Coulomb effects from the pp scattering data(Sa77). It has been argued that the error bars on the p-p data should be larger, as Sauer and Walliser (Sa77) have pointed out that there are theoretical uncertainties in subtracting Coulomb effects from a_{pp}.

Table 4-1: Experimental nucleon-nucleon scattering lengths.

System	State	a_{NN}(fm)	Reference
n - n	$^1S_{J=0}$	-16.6 ± 0.5	(Fe81)
		-18.6 ± 0.5	(Sa77)
p - p	$^1S_{J=0}$	-17.1 ± 0.2 *	(Na79,He73)
n - p	$^1S_{J=0}$	-23.748 ± 0.010	(Na79)
n - p	$^3S_{J=1}$	5.424 ± 0.004	(Na79)

* Corrected for electromagnetic effects.

Since the scattering lengths are not well known, and not even very sensitive to a CSB potential(Sh78), (in fact in may be possible to construct a CSB potential which leaves $a_{nn} = a_{pp}$ (He79)) a better test for charge symmetry is necessary.

A CSB potential not only changes the force between nucleons; it will also effect the optical-model describing nucleon scattering. DeVito et al.(De81) have used this to search for evidence of charge asymmetry in p and n elastic scattering from ^{40}Ca. They found that the volume integral of the real optical potential for proton scattering exceeded that for neutron scattering by 14±10 MeV-fm^3, after correcting the p+^{40}Ca data for Coulomb effects. This result, if interpreted in terms of a CSB part of the N-N force implies a slightly stronger pp than nn force. However, similar analysis by Winfield and Austin (Wi84) found the reverse effect in nucleon scattering from ^{28}Si and ^{32}S. They also analysed data from ^{12}C and found an effect of the same sign and the ^{40}Ca data. The reason for the internal disagreement and the disagreement with the DeVito data is unknown. It could be from Coulomb effects not included in the optical model analysis.

A sensitive test for CSB forces is the Coulomb displacement energies from mirror nuclei. The Coulomb displacement energy is defined as

$$E_C = Z_> - Z_< + \Delta_{nh} \qquad (4.10)$$

where $Z_{>(<)}$ is the atomic mass excess of the $T_z = -1/2$ $(+1/2)$ member of the pair, and Δ_{nh} is the neutron-hydrogen mass difference. Since the difference between mirror members is one neutron has been changed to a proton, the number of V_{np} and $V_{nn} + V_{pp}$ interactions remains constant while $V_{nn} - V_{pp}$ changes sign. The displacement energy is then a direct measure of whether $V_{nn} = V_{pp}$ and charge symmetry is valid.

The Coulomb force is well known, and hence it should be easy to calculate the decrease in the binding energy due to the increase Coulomb energy in the $T_z = -1/2$ member. The difference between the calculated Coulomb displacement energy assuming charge symmetry, E_C^{THY}, and the measured Coulomb displacement energy, E_C^{EXP}, will be due to CSB forces. The A=57 mirror pair provides a particularly good test because it has one nucleon outside the A=56 doubly magic closed core. Thus, the nuclear structure calculations will be more reliable, as in the case of other single particle or single hole mirror nuclei, because the wavefunctions are better known than in other mirror pairs.

The first detailed review article of the comparison between calculated and measured Coulomb displacement energies by Nolen and Schiffer(No69) found a constant ~7% discrepancy. This disagreement is now known as the Nolen-Schiffer anomaly. The authors suggested a 15% to 20% reduction in the valence orbit calculated from single particle models would resolve the anomaly. However, there is little experimental or theoretical support for such a

reduction(Br79), and it shifts the anomaly from one of displacement energies to nuclear radii. Although Nolen and Schiffer studied systems with $T \geq 1/2$, we will restrict ourselves to $T = 1/2$ systems. Systems with $T > 1/2$ would require charge independence to have $E_C^{EXP} / E_C^{THY} = 1$

4.3 CDE Model

4.3.1 Introduction

To illustrate the anomaly we will use a model for Coulomb displacement energies (CDEs) developed by Brown and Meyer-Schutzmeister(Br78a). We will compare the calculated and measured CDEs in mirror nuclei in the region A=39 to 59, including the new results for A=57 and 59, for levels having either single particle or single hole structure. The deviations between experiment and this standard model will be discussed in terms of some conventional improvements which can be made in the model wavefunctions and in terms of some less conventional corrections which have been proposed. The consistency of these results with a CSB potential will then be discussed.

4.3.2 Description of the Model

The calculations were performed in terms of particle interactions. If the neutron rich nucleus, $Z_<$, had even $Z_<$, then it was treated as a one-particle state with the core charge $Z_c = Z_<$. The core radius was taken as the ground state charge radius of the neutron rich member, $r_c = r(Z_<)$. If however $Z_<$ was odd, then the system was treated as three nucleons outside of a $Z_c = Z_< - 1$ core, with r_c calculated from

the oscillator parameter extracted from $r(Z_<)$. In this case an additional term was present representing the Coulomb interaction between the two valence protons. The Coulomb displacement energy was then taken as the sum of three terms, the direct term equation 4-11, the exchange term, and for odd $Z_<$ systems the pairing energy.

The direct term was calculated numerically with harmonic-oscillator (H-O) radial wave functions. In order to understand qualitatively how the results depend on the valence (r_v) and the core (r_c) point proton rms radii, Brown studied several simple functional forms which involve these quantities and found the following useful parameterization

$$\Delta E_d = 6e^2 Z_c/[5R_c(1 + \delta/4)] \qquad (4.11)$$

where $R_c = (5/3)^{1/2} r_c$, $\delta = (r_v/r_c)^2 - 1$. The relative dependence of the exact numerical calculation upon r_c and r_v is well reproduced by ΔE_d and is in absolute agreement with the exact calculation to within about 0-5% depending on the orbit. The difference between the exact H-O result and equation 4-11 was treated as a correction (labeled ΔE_{dcorr} in Table 4-4). Note that in the limit when the valence and core rms radii are equal ($\delta=0$), ΔE_d is just that for a uniformly charged sphere. In the limit when $r_v >> r_c$, ΔE_d goes to zero as expected.

The finite proton size can be included by using the experimental charge radius, $R_c = (5/3)^{1/2} r_{ch}$. For the A = 39

and 40 the rms charge radius is known experimentally. Other core radii can be extrapolated from the rms radii measured in near by nuclei (Sh76), e.g. in the A=57 case

$r_{ch}(^{57}Ni) = r_{ch}(^{58}Ni) + r_{ch}(^{53}Cr) - r_{ch}(^{54}Cr) = 3.753$ fm.

Comparisons to known nuclei show the extrapolation method to be better than 1%. Table 4-2 lists the values of r_{ch} used in the calculations along with the references.

The exchange term, ΔE_{ex}, was taken to be 0.7 times the Fermi gas model prediction (Eq. 3 in (No69)). The factor of 0.7 was based on an average comparison between the exchange terms calculated with H-O radial wave functions and the Fermi gas model for the A=15,17,39, and 41 nuclei. The valence two-particle interaction, ΔE_{pp}, was calculated with an appropriate 3 particle wavefunction of seniority one and an H-O radial wave function with an oscillator length deduced from the rms charge radius discussed above(Br78a). For the total displacement energy Brown also included ΔE_{so} the relativistic spin-orbit correction(Eq. 21 in (Br78a)), ΔE_{vp} the vacuum polarization correction (Eq. 4.23 in (Sh78)), and the contribution, ΔE_{np}, from change in kinetic energy due to the proton-neutron mass difference (Eq. 4.29 in (Sh78)).

Table 4-2: Summary of the experimental and extrapolated charge radii used in the CDE calculation.

Nucleus	$r_{ch}(exp)^a$ [fm]
^{39}K	3.437 ± 0.002
^{41}Ca	3.481 ± 0.010
^{43}Sc	(3.540) = $^{45}Sc-^{44}Ca+^{42}Ca$
^{45}Ti	(3.586) = $^{46}Ti-^{44}Ca+^{43}Ca$
^{47}V	(3.638) = $^{51}V-^{50}Ti+^{46}Ti$
^{49}Cr	(3.667) = $^{50}Cr-^{48}Ti+^{47}Ti$
^{51}Mn	(3.684) = $^{55}Mn-^{54}Cr+^{50}Cr$
^{53}Fe	(3.697) = $^{49}Ti-^{50}Ti+^{54}Fe$
^{55}Co	(3.713) = $^{55}Mn-^{54}Cr+^{54}Fe$
^{57}Ni	(3.753) = $^{58}Ni-^{54}Cr+^{53}Cr$
^{59}Zn	(3.822) = $^{58}Ni-^{62}Ni+^{63}Cu$

[a] Experimental data for A=39 from (Br80a), A=41 from (Be80,Ko79), and A=43-59 extrapolated from the data from (Wo81) and (We80).

4.3.3 Results

The experimental CDEs and the results of the calculation are listed in Table 4-3. The main contributions to the calculated CDE are listed in Table 4-4. For the initial comparison, δ was taken from the H-O value. The ratios of experimental to theoretical displacement energies are plotted in Figure 4-1. In the comparison shown in Figure 4-1 note that for the A=41, 7/2- state the 11% enhancement of experiment over theory is known as the Nolen-Schiffer anomaly(No69). The ratios of our new results are consistent with the decrease in the ratio established from the more accurately measured displacement energies. An interesting feature of the results is the apparent absence of an anomaly for the 3/2+ orbits. The orbit dependence of the anomaly suggests a nuclear structure correction which has not been included. There are three possible corrections which will now be discussed.

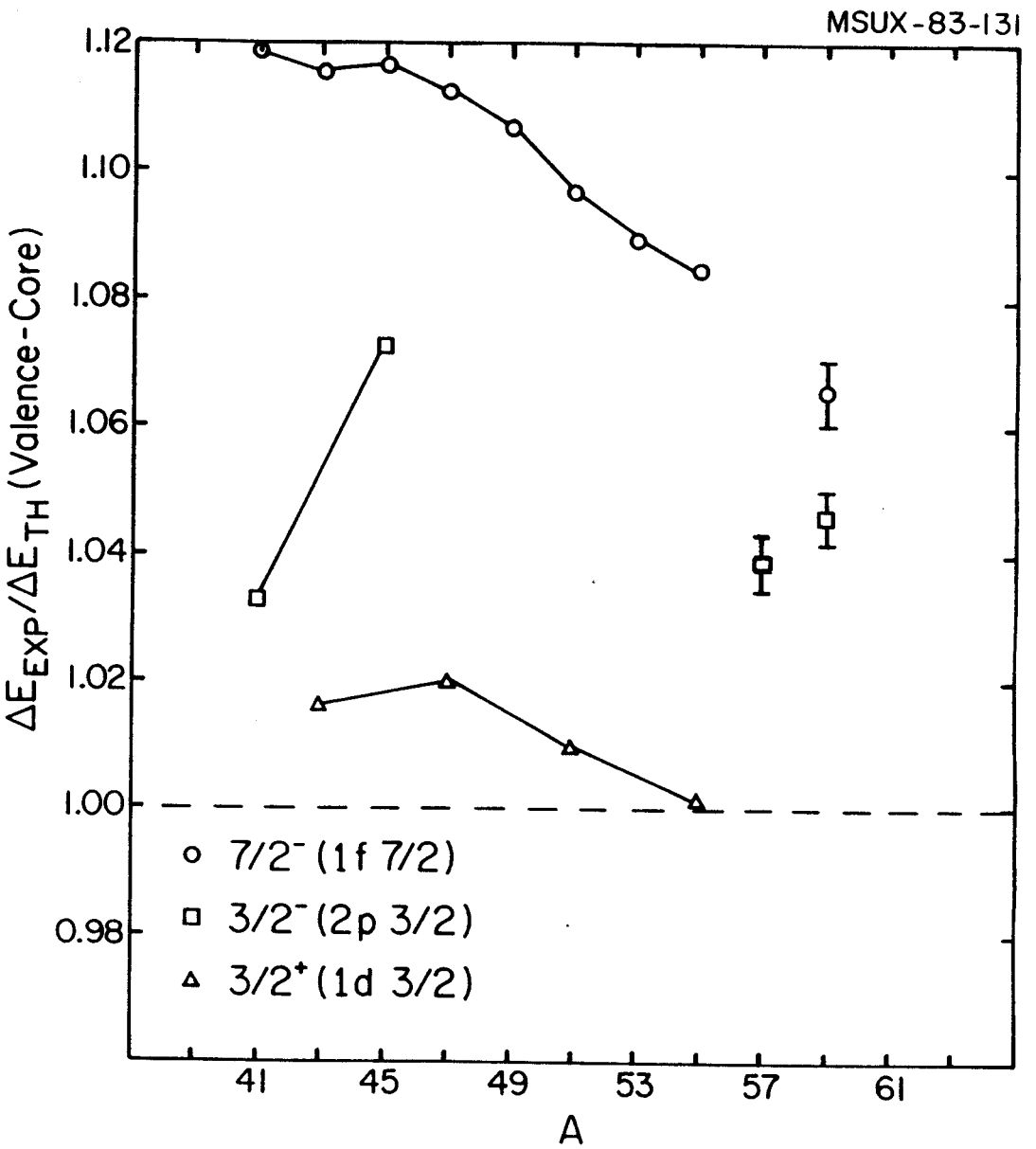

Figure 4-1: The ratio of the experimental to the calculated CDEs as a function of A.

Table 4-3: The experimental CDEs and the calculated CDEs.

A	J^{π}	ΔE_C^{exp}(keV)	Reference	ΔE_C^{thy}(keV)
39	$3/2^+$	7307(5)	(Wa84)	6791
41	$7/2^-$	7278	(Wa84)	6563
	$3/2^-$	7053(1)	(En78)	6389
43	$3/2^+$	7805(8)	(Me78)	7315
	$7/2^-$	7644(8)	(Wa84)	6893
45	$7/2^-$	7902(27)	(Wa84)	7098
	$3/2^-$	7929(27)	(Gr80)	7086
47	$3/2^+$	8447(13)	(Ha77)	7894
	$7/2^-$	8258(10)	(Ha77)	7433
49	$7/2^-$	8490(25)	(Ha78)	7656
51	$3/2^+$	9059(14)	(Mu77)	8562
	$7/2^-$	8846(13)	(Mu77)	8049
53	$7/2^-$	9086(18)	(Wa84)	8283
55	$3/2^+$	9699(12)	(Mu77)	9237
	$7/2^-$	9473(10)	(Wa84)	8603
57	$3/2^-$	9510(50)	(Sh85)	8661
59	$3/2^-$	9882(40)	(Sh83)	8911

Table 4-4: Main contributions to the CDE calculation.

A	J^{π}	ΔE_d (keV)	δ_{HO}	δ_{HF}	ΔE_{dcorr}	ΔE_{ex}	ΔE_{pp}
39	$3/2^+$	6727	0.189	0.187	64	-296	454
41	$7/2^+$	6836	0.500	0.513	-19	-304	0
	$3/2^-$	6836	0.500	1.354	288	-304	0
43	$3/2^+$	7292	0.129	0.187	75	-298	448
	$7/2^-$	6801	0.500	0.513	-12	-303	376
45	$7/2^-$	7407	0.435	0.457	-12	-307	0
	$3/2^-$	7407	0.435	0.590	234	-307	0
47	$3/2^+$	7888	0.085	0.108	85	-301	445
	$7/2^+$	7369	0.435	0.590	-4	-305	373
49	$7/2^-$	7992	0.385	0.401	-4	-311	0
51	$3/2^+$	8569	0.050	0.051	93	-308	446
	$7/2^-$	8016	0.385	0.401	3	-312	375
53	$7/2^-$	8666	0.345	0.309	-15	-318	0
55	$3/2^+$	9274	0.022	-0.079	99	-315	449
	$7/2^-$	8684	0.345	0.296	10	-319	377
57	$3/2^-$	9263	0.313	0.520	220	-323	0
59	$3/2^-$	9144	0.313	0.520	258	-319	346

Table 4-5: Corrections to the CDE calculation.

A	J^{π}	ΔE_{so} (keV)	ΔE_{vp}	ΔE_{np}	ΔE_{fw}	ΔE_{cp}
39	$3/2^{+}$	94	42	33	-27	-320
41	$7/2^{-}$	-99	46	42	13	44
	$3/2^{-}$	-33	46	42	-354	-82
43	$3/2^{+}$	93	45	32	10	-382
	$7/2^{-}$	-98	46	42	12	28
45	$7/2^{-}$	-100	49	40	11	13
	$3/2^{-}$	-33	49	40	-197	-109
47	$3/2^{+}$	94	48	30	47	-444
	$7/2^{-}$	-98	49	40	10	-18
49	$7/2^{-}$	-102	53	39	9	-17
51	$3/2^{+}$	99	52	29	84	-507
	$7/2^{-}$	-103	53	39	8	-32
53	$7/2^{-}$	-108	56	38	7	-47
55	$3/2^{+}$	105	56	29	121	-570
	$7/2^{-}$	-108	57	38	6	-62
57	$3/2^{-}$	-37	60	37	-372	-191
59	$3/2^{-}$	-36	59	37	-374	-205

4.3.4 Corrections

As seen in Figure 4-1 the orbits which are close to being unbound, such as the A=41 and A=57 $3/2^-$ states, have a smaller anomaly that the more bound states of the same spin and parity. This effect is due to the overestimation of the binding energy using H-O wavefunctions which leads to the underestimation of δ for these orbits. This effect can be corrected by recalculating the CDEs with wavefunctions generated from a finite potential well. The correction, ΔE_{fw}, is taken as the difference between spherical Hartree-Fock (H-F) calculations of the CDE using an H-O potential and the SGII potential of Sagawa and van Giai(Gi81). Both calculations were performed with the same rms charge radius of the core, hence the CDE difference will reflect only the change in the valence wavefunctions. For the calculation of the correction for the ^{57}Cu-^{57}Ni pair, we assumed a closed $f_{7/2}$ shell for ^{56}Ni and a valence particle in the $p_{3/2}$ orbit. The separation energy between ^{57}Cu and ^{56}Ni was constrained to the experimental value in the H-F calculation by multiplying the central H-F potential by an appropriate factor. Calculations for the other single particle orbits were done in a similar manner. The corrections for single hole states, such as A=59 $3/2^-$, were taken from a linear extrapolation in A from the single particle results. The exceptions to this method were for the A=39 and 55 $3/2^+$ states. These corrections were taken directly from the H-F calculations because of the A=40 and 56 closed cores and the

single hole nature of these states. The results for ΔE_{fw} are shown in Table 4-5. The effect of this correction was to make the dependence of the anomaly for a given orbit more linear in A.

The second correction which should be considered is the core polarization correction(Au69,Sh78), ΔE_{cp}. This correction arises from the change in the radial wave functions of the core protons due to the interaction with the valence neutron or proton. There is an orbit dependence in this correction due to the fact that the core protons can be "pulled out" or "pulled in" depending on the shape and size of the valence radial wave function. This correction was obtained, for example in the A=57 case, by carrying out the spherical H-F calculations separately for ^{57}Cu and ^{57}Ni and then finding the difference between the total Coulomb energy of the core protons in each nucleus. Since the nuclear force is charge symmetric in H-F calculations, the difference between the calculated core Coulomb energy of these two calculations will be due to the Coulomb force only, i.e. the core polarization correction. The change in the total energy due to the change in the nuclear densities will cancel because the valence neutron has the same effect on the core protons in the $Z_<$ member as the valence proton has on the core neutrons in the $Z_>$ member. Other mirror pairs with A=40 or 56 closed cores are calculated in the same manner. A linear interpolation is used to extract the

correction for other pairs. The results for ΔE_{cp} are listed in Table 4-5.

The results of these corrections are shown in Figure 4-2. Much of the orbit dependence which existed in Figure 4-1 has been removed. There is still a discrepancy between particle and hole states. This difference is probably do to configuration mixing in the core which was not included in these calculations. The effect of configuration mixing has been considered by several authors(Sa76,Po77).

Sato(Sa76) included the effects of core excitations by correcting the experimental CDEs to reflect the fact that the measured CDEs include a component which is due to core configuration mixing. The correction found by Sato for the A=39 and 41 cases is shown in Table 4-6. Also included in the table is the configuration mixing correction calculated by Poves, Cedillo and Gomes(Po77). These authors, unlike Sato, simply diagonalized $H = H + V_C$ in a model space with excitations up to 4p-4h. Although the method is probably better, the results are not significantly different.

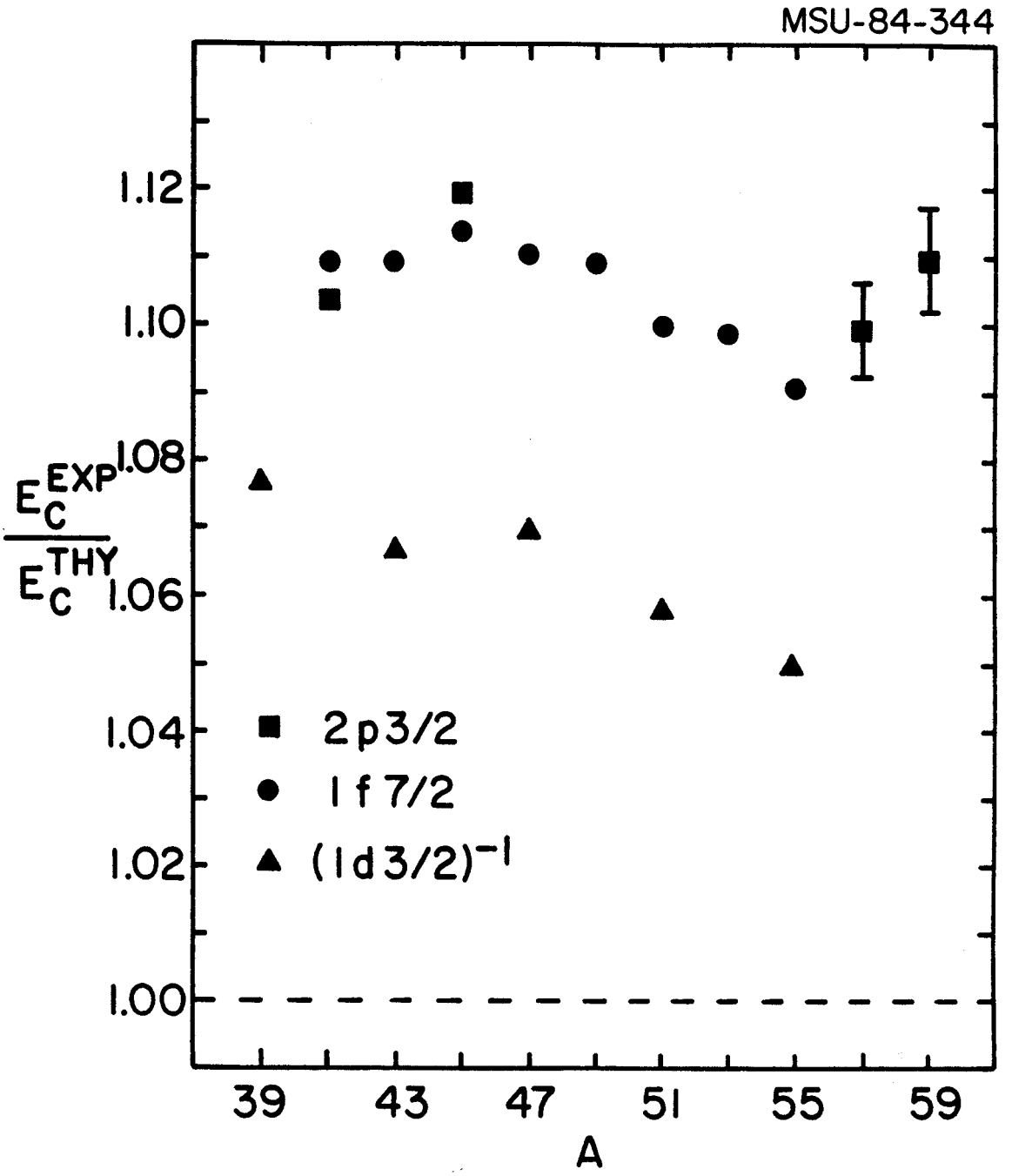

Figure 4-2: Ratios of experimental to calculated CDEs versus A, including core polarization and finite well corrections.

Table 4-6: Configuration mixing corrections to the CDE calculation.

A	J^{π}	ΔE^{Sa76}_{conf}(keV)	ΔE^{Po78}_{conf}(keV)
39	$3/2^{+}$	-125	-160
41	$7/2^{-}$	50	140
	$3/2^{-}$	350	---

If we take the average of these corrections and apply them to the appropriate orbits in this study, we find

$$E_C^{EXP} / E_C^{THY}(A=39;3/2^+) = 1.10$$

and

$$E_C^{EXP} / E_C^{THY}(A=41;7/2^-) = 1.09.$$

This correction seems to remove, at least for the A=40 core, the remaining discrepancy between particle and hole states. We have not performed the configuration mixing calculations for other orbits, but we suspect it is responsible for the difference in the anomaly for particle and hole states.

The implication of the 5 to 10% discrepancy between the calculated and measured CDEs is either that some significant effect has been left out of the calculations or that charge symmetry breaking exists in mirror systems. The former seems unlikely, especially for the single particle orbits outside closed cores, such as the ^{57}Cu-^{57}Ni case, where the H-F and shell model calculations are expected to be good. Similar conclusions have been reached by several authors for the A = 3(Br78b,Ba82), 15, 17(Po77,Sh78,Sa76,Ba77), 39, and 41(Au80,Ne74) systems. Two of these studies found a smaller anomaly than we find(Po77,Au80), approximately 4% compared to 9%, but still did not resolve the anomaly.

4.4 Discussion

The remainder of this chapter will be a brief review of the different explanations of the anomaly, including a review of the consistency of the results with a CSB potential.

Brown has shown(Br78a) that the entire anomaly can be explained by the core-compression model proposed by Shlomo and Friedman(Sh77,Fr77). Shlomo and Friedman make the hypothesis that the charge radius of both mirror nuclei are equal. Given that the valence radius is in general larger than the core radius, this can only be accomplished by forcing the valence radius to be smaller (the idea originally proposed by Nolen and Schiffer) or by compressing the protons in the proton rich nucleus. Since neither of these effects can easily be reproduced by microscopic calculations, these hypotheses simply shift the displacement energy anomalies into radius anomalies.

Another recent conjecture on a solution to the anomaly was was given by Greben and Thomas(Gr84). They use a hybrid quark-nucleon model in which nucleons can form multiquark bags at short distances. They note that it has already been observed that the mass difference between 6q bags formed from two protons and from two neutrons is not equal to twice the proton-neutron mass difference(To83a). They find they are able to resolve the anomaly for the A=3 system for which they are able to perform a detailed calculation. However for heavier nuclei they can not resolve the anomaly. In

fact they comment that their model gives identical results to the conventional nuclear physics models for A > 32, whereas all the anomaly can be resolve in the A=3 system and 1/2 the anomaly around A=12.

4.5 Conclusions

The remaining question is: Is the Nolen-Schiffer anomaly evidence for charge symmetry breaking? Shlomo(Sh78) has done a study of CSB potentials involving meson exchange. He finds that if one fixes the constants to resolve the A=3 anomaly, the CSB potentials are too short range to resolve the anomaly for heavier A nuclei, similar to the results of Greben. Negele(Ne74) however has noted that adjusting the ratio of the central and spin components of a given force, such that they almost cancel in the 3-body system in which only even states are present and contribute strongly in heavier nuclei in which odd partial waves are significant, can reproduce the systematic behavior of the Nolen-Schiffer anomaly. However, as Shlomo has argued(Sh78), this form for charge symmetry breaking potentials is not expected. It is interesting to note that the differences in optical potentials between proton and neutron scattering found in the recent analysis by Austin and Winfield (Wi84) may be accounted for by a CSB potential which is in rough agreement with that needed to solve the Nolen-Schiffer anomaly (Ne74). However the optical-potential results are inconsistent (see section 4.2) and have the disadvantage that only the effect of the mean field

is tested rather than the N-N force itself. The size of a CSB potential consistent with the results of Winfield and Austin for ^{28}Si and ^{32}S is however consistent with the measured N-N scattering lengths, although the error bars on the N-N scattering lengths are large and any firm conclusions difficult to make. We do believe that the Nolen-Schiffer anomaly is evidence for charge asymmetry, despite some remaining uncertainty in calculating corrections. But, its magnitude is an open and interesting question. In light of the uncertainty of the data on NN scattering lengths and lack of other evidence for CSB it is difficult to draw any definite conclusion.

CHAPTER FIVE

5.1 Introduction

According to recent theories it is possible to find rapid hydrogen burning in various astrophysical environments. The name given to this type of hydrogen burning is the rp-process in analogy to the classical r-process (Bu57,Se65) of rapid neutron capture in nucleosynthesis. The environments where one would expect the rp-process to play a role are: supermassive stars ($M/M_{\odot}$= 10^5 to 10^8) (Ho65,Fr73,Fr74,Fr78), accreting neutron stars (Ha75,Jo80,Ta81,Wa82), dense, inhomogeneous cosmologies (Re72,Ho75), red giants with neutron star cores (Wa81), and nova and supernova outbursts (St74,St75). A common feature of these systems is a large hydrogen density and a high temperature in the range of 10^8 K to 10^9 K (10 to 100 keV) or higher. The high temperature is necessary because the Coulomb barrier prohibits proton burning at the typical main sequence stellar temperatures of 10^7 K (1 keV). Since the rp-process involves proton rich nuclei, it is interesting to see if ^{57}Cu and ^{59}Zn play a role.

In a detailed study of the rp-process Wallace and Woosley (WW) (Wa81) found that the $^{56}Ni(p,\gamma)^{57}Cu$ reaction was an important branch point between the A≤56 and the A>56 nuclei. The mechanism of hydrogen burning is the (p,γ) reaction, hence knowledge of the proton resonance energy and Q value for the inverse reaction, photodisintegration, is necessary to perform rp-process calculations. In their calculation, Wallace and Woosley (Wa81) assumed that the structure of ^{57}Cu would be identical to its mirror nucleus, ^{57}Ni. As we have seen in chapter 2, this is not true. WW took the $Q_{\gamma p}$ value from a prediction of Harcore ($Q_{\gamma p}$= -0.69 (Ha67)), which was very close to our measured value of $Q_{\gamma p}$= -0.74(5). In this chapter hydrogen burning will be discussed in relation to the data obtained on the atomic mass and structure of ^{57}Cu. After an introduction to the rp-process, the importance of ^{57}Cu to the rp-process calculations of X-ray bursts, chaotic cosmologies, and supermassive star emplosions will be discussed. In the following section the calculations of the proton decay widths of ^{57}Cu and photodisintegration rates will be presented to demonstrate the effect of the new data on the rp-process calculations. Finally, the implications of the new data will be discussed.

5.2 Rp-process Background

One expects that at temperatures around the range of 10^8 K or 10^9 K that the dominant mode for energy generation would be the β-limited CNO cycle (Ho65,Fr73). The name

denotes that the rate at which hydrogen is converted to He is limited by the β-decay lifetimes of the two proton-rich nuclei ^{14}O and ^{15}O, rather than the proton capture rate of ^{14}N, which characterizes lower temperatures. The β-decays also limit the energy generated, except at very high densities ($\rho > 10^7$ g/cm^3) (Wa81) where electron capture accelerates the weak decays. The β-limited CNO cycle follows the path

$$^{14}O(\beta\nu)^{14}N(p,\gamma)^{15}O(\beta\nu)^{15}N(p,\alpha)^{12}C(p,\gamma)^{13}N(p,\gamma)^{14}O \qquad (5.1)$$

It is possible to have a breakout from this cycle via the $^{15}O(\alpha,\gamma)^{19}Ne$ reaction. If in addition

$$\rho X \lambda_{p\gamma}(^{19}Ne) > \lambda_{\beta}(^{19}Ne) \qquad (5.2)$$

where ρ is the density, X is the ^1H mass fraction, $\lambda_{p\gamma}$ is the rate for reaction $^{19}Ne(p,\gamma)^{20}Na$ in units of cm^3/mole-sec, and λ_{β} is the β-decay rate of ^{19}Ne; then ^{19}Ne captures a proton to form ^{20}Na rather than decaying to the stable nucleus ^{19}F. WW (Wa81) have shown that there are many combinations of temperature and density (above 10^8 K and log ρ(g/cm^3) > 10^{-2}) at which the breakout from the CNO cycle is possible, and proton capture on ^{19}Ne is favored over β-decay (see Figure 2 of WW (Wa81)).

Once ^{19}Ne has captured a proton, it is impossible for material to return to the main CNO cycle. Thus seed

material is burned in the rp-process, which depletes the fuel for the process. As was mentioned in the introduction, the rp-process is similar to the r-process. Protons are added to seed nuclei until the proton drip line is reached. The process moves along the drip line because near the drip line the (p,γ) resonances are lower in proton energy. This is true unless a short β-decay lifetime limits the production of a particular isotope. For lighter nuclei the β-decay rates do not compete, and material is synthesised out to the proton drip line. For larger Z, increasing Q_β values and an increasing Coulomb barriers causes the β-decays to compete. A diagram taken from WW (Wa81), Figure 5-1, shows the rp-process flow, for a sample calculation.

Wallace and Woosley (Wa81) found that the flow tended to build up at ^{56}Ni. This is due to the unique combination of long β-decay half life (6.1 days) for ^{56}Ni and the low photodisintegration temperature for ^{57}Cu (T_9= 0.5). In stellar environments the lifetime of ^{56}Ni would be even longer because ^{56}Ni decays only by electron capture (β-decay is forbidden due to the structure of ^{56}Co), and normally the electron densities are low. In a model in which no flow above ^{56}Ni was possible, the rp-process would generate energy until all the seed nuclei were converted to ^{56}Ni, and the process would stop. Wallace and Woosley demonstrated the potential importance of the rp-process under these assumptions since the energy liberation from the rp-process was 100 times that of the β-limited CNO cycle.

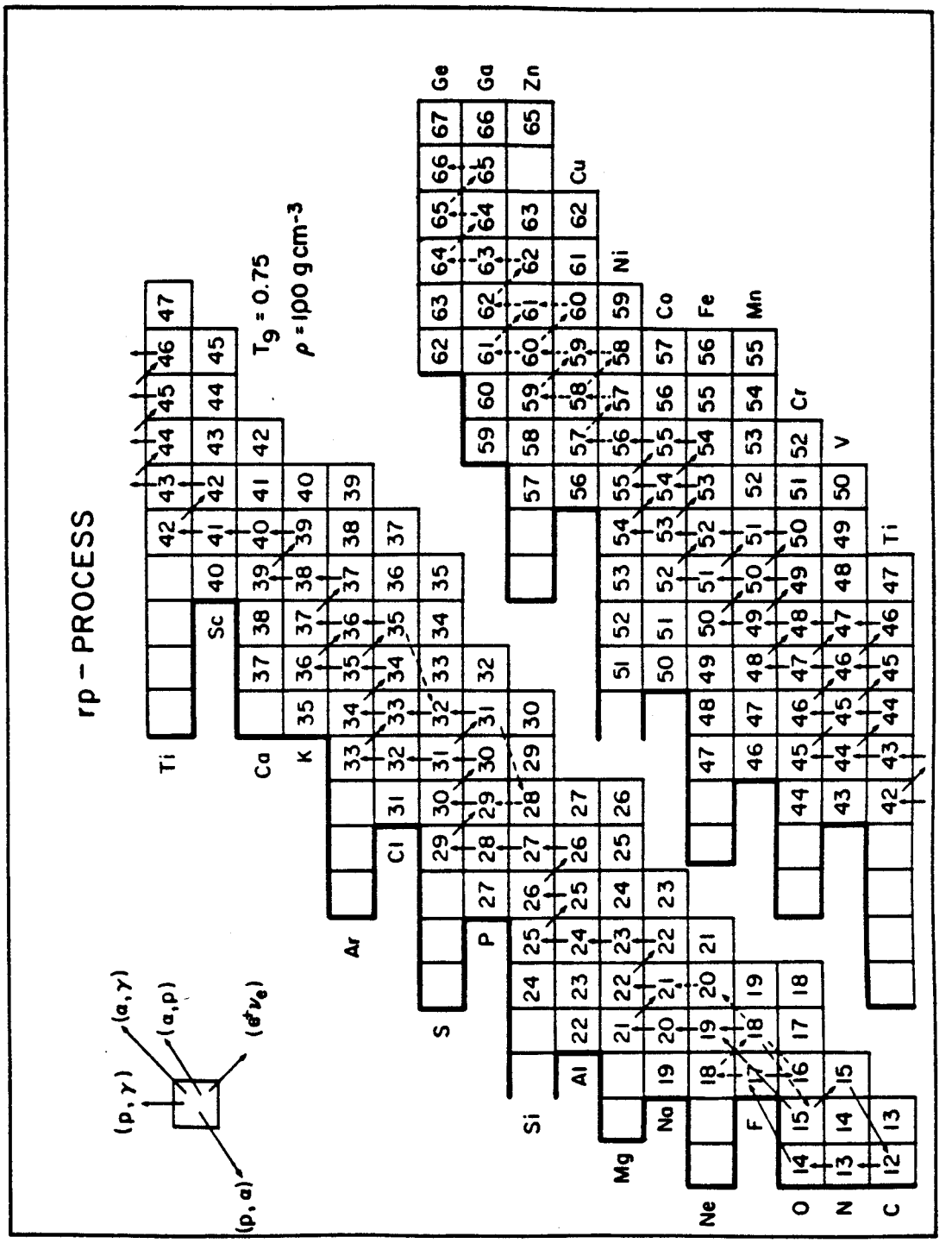

Figure 5-1: Diagram of the rp-process flow.

Any further energy generation or nucleosynthesis at later times in the process would depend on the flow above A=56.

5.3 Rp-process Flow to A>56

As noted in the previous section the rp-process tends to concentrate material at ^{56}Ni. The flow and energy generation for A>56 will be dominated by the ^{56}Ni(p,γ)^{57}Cu reaction. To study the effects and implications of flow above A=56 we will consider three phenomena for which such flow is considered important: supermassive star (SMS) explosions (Ho65,Fr73,Fr74), chaotic cosmologies (Re72,Ho75), and one area of great current interest, X-ray bursts (Ha75,To80,Ta81,Wa81,Wa82,Wa83).

5.3.1 Supermassive Star Explosions

Calculations by Fowler (Ho65) and Frick (Fr73,Fr74) suggest that enhanced energy generation may stop the collapse of very heavy stars. This would cause a bounce and reexplosion of the star. The occurrence of such an event will depend on the process of energy generation in the hot, dense hydrogen environment. Recent calculations by Frick and Ober (Fr78) suggest that the rp-process would allow such a bounce of super massive stars to occur even for initial metallicity of zero. An interesting question is whether such occurrences would account for the initial metallicity in the universe (Wa81). The rp-process would generate large

amounts of heavy elements which would be spread by the resulting reexplosion.

Wallace and Woosley attempted to calculate the heavy element production in such a process but noted (Wa81) that the hydrodynamic details of such SMS are not well known, which makes reliable nucleosynthesis calculations difficult. Under various models WW compared the elemental nucleosynthesis to an extreme population II star, HD122563 (Tr75). They found that the rp-process overpredicts rarer elements such as scandium and vanadium because the rp-process does not select according to binding energy but rather according to the (p,γ) reactions and β^+-decays. They also noted that at temperatures $T_{9\ max} > 1$ the amounts of isotopes such as ^{74}Se and ^{78}Kr are predicted in amounts well above the naturally observed solar abundances. This indicated that if the process took place, the material was not spread into the interstellar medium.

5.3.2 Chaotic Cosmology

In the standard Big Bang model (Wa67) the universe undergoes a uniform expansion and cooling. Nucleosynthesis calculations with a constant entropy per baryon and other parameters to match observed properties of the current universe yield ^{1}H, ^{2}H, ^{3}He, ^{4}He and ^{7}Li in reasonable agreement with the observed solar abundances (Wa73). In such a model the baryon density is low during the era of

nucleosynthesis ($T \sim 10^9$), and no heavier elements are produced. Because of the low densities the rp-process is not expected to play a role. If however there were density fluctuations in which a sufficient baryon density was reached, the rp-process could be responsible for early heavy element production in the universe. Reese (Re72) has explained the presence of the microwave background radiation as due to turbulence in the initial expansion. This is consistent with density fluctuations up to 10^6 times ρ_0, where $\rho_0 = \rho_0(t)$ is the density assumed in the standard Big Bang model. Hoyle (Ho75) has predicted even larger density fluctuations, up to 10^9 ρ_0.

Wallace and Woosley performed rp-process calculations assuming the cosmology of Reese. The resulting nucleosynthesis from the calculations are summarized in Table 5-1. The solar abundances are taken from Cameron (Ca73). It is interesting that elements from Ca to Kr are produced at a rate roughly 10^{-4} that of solar abundances. It is especially interesting that the abundances for the heavy elements agree well with the abundances seen in HD1222563. However, Wallace and Woosley concluded that the large disagreement with the lower A abundances placed serious doubts on the validity of the model. This seems reasonable since the other nucleosynthesis which produced the additional lighter elements should have also produced additional heavier elements.

Table 5-1: Elemental Abundances calculated assuming an rp-process in chaotic cosmologies compared to solar abundances and type II stars. The data in the table is taken from WW (Wa81). The production ratios are the final mass fraction produced in the calculation divided by the Solar mass fraction.

Elements	Solar Abundance	Production Ratio	
		HD122563	Calculation
C	3.43(-3)		3.03(-7)
N	1.23(-3)		3.50(-7)
O	8.29(-3)		5.90(-7)
Si	6.79(-4)		1.31(-11)
Ca	6.97(-5)		6.31(-6)
Sc	3.80(-8)	1.6(-3)	1.37(-3)
Ti	3.03(-6)	2.5(-3)	2.95(-4)
V	3.22(-7)	7.9(-3)	2.70(-3)
Cr	1.55(-5)	3.2(-3)	1.39(-3)
Mn	1.24(-5)	1.3(-3)	1.03(-3)
Fe	1.06(-3)	2.5(-3)	4.29(-3)
Co	3.15(-6)	2.0(-3)	2.04(-3)
Ni	6.75(-5)	4.0(-3)	3.95(-4)
Cu	8.30(-7)	....	1.45(-3)
Zn	1.95(-6)	6.3(-3)	6.87(-4)
Ga	8.09(-8)	....	8.34(-4)
Ge	1.10(-7)	....	4.43(-4)
As	1.20(-8)	....	7.89(-5)
Se	2.16(-8)	....	1.40(-4)

The results of this model also seemed to rule out cosmologies with $\rho >> \rho_0$ since they predict even larger abundances of heavier elements. Wallace and Woosley concluded that regions having very high baryon densities as in the Hoyle model, if they existed, must have formed a small fraction of the mass of the universe or else remained bound objects.

5.3.3 X-Ray Bursts

Grindlay et al. in 1976 reported astrophysical objects which periodically emitted short bursts of X-rays. The emissions called X-ray bursts can be explained by the rp-process (Wo76,Wa83,Ta80). The general picture of these objects is that matter is accreted onto the surface of a neutron star from a companion white dwarf. On the surface of the neutron star when sufficient density of H has been reached, the rp-process starts and a thermonuclear runaway takes place (To80,Ta81,Wa82). However, since the rp-process burns the seed material, the runaway will stop in a finite time period. This mechanism produces bursts of X-rays with a set period and length depending of the details of the binary system. There are actually two classes of observed X-ray bursts. The rp-process is able to account for Type I bursts which have lengths from seconds to minutes. Type II bursts have shorter times and are less regular.

Generally, the rp-process flow is believed to stop at ^{56}Ni. In fact in some calculations the only remaining products are ^{56}Ni and H (Wo83). However, in the extreme conditions found in some neutron star accretion models, some flow may continue beyond ^{56}Ni. The energy generated at the late times depends critically on the flow above ^{56}Ni. Calculations by Hanawa, Sugimoto, and Hashimoto (Ha82) suggest that (p,γ) reactions on elements heavier than Ni are very important for X-ray burst models. In particular, the question of the particle stability of ^{65}As is critical because it determines whether A>65 material can be produced in the rp-process.

5.4 Recalculations of the ^{56}Ni(p,γ)^{57}Cu Rates

5.4.1 Introduction

To understand how the resonant energy for the (p,γ) reaction effects the cross section, a short discussion of resonant reactions will be presented. For a more detailed discussion see Clayton section 4-7 (C168). We will only consider the resonant reaction rate formalism, since WW found that the cross sections are dominated by the (p,γ) resonances and the contributions from nonresonant reactions were small. The distinction between the formalisms is that in the resonant formalism we need only consider protons at the resonance energy, where as the nonresonant reactions

involve integration over the proton energy spectrum with many energies contributing.

To illustrate the effect of the level structure of ^{57}Cu on resonant reaction rates we will take as an example the $^{12}C(p,\gamma)^{13}N$ reaction, which has been studied extensively. Figure 5-2 shows the influence of the states in ^{13}N on $\sigma[^{12}C(p,\gamma)]$. For the temperatures we are considering, $T_9 = 1$, the resonance at $E_r = 424$ keV will dominate the cross section. As seen in the figure the total cross section for the reaction will depend on the width, Γ_p, of the resonance. In the case of the reaction $^{56}Ni(p,\gamma)^{57}Cu$, it is difficult to measure the (p,γ) cross section since ^{56}Ni has only a 6 day halflife. It is possible however to calculate this cross section with information on the level structure of ^{57}Cu. These calculations will be discussed below. Based on the data obtained on ^{57}Cu from the $(^7Li,^8He)$ reaction the expected picture is shown in Figure 5-3. The various parameters in the figure will be discussed in section 5.5 of this chapter.

5.4.2 Resonance Energy and Decay Widths

The rate per pair of particles 1 and 2, λ_{12}, can be expressed as (see Clayton eq. 4-190)

$$\lambda_{12} = \int_0^\infty \Psi(E)v(E)\sigma(E)dE \qquad (5.3)$$

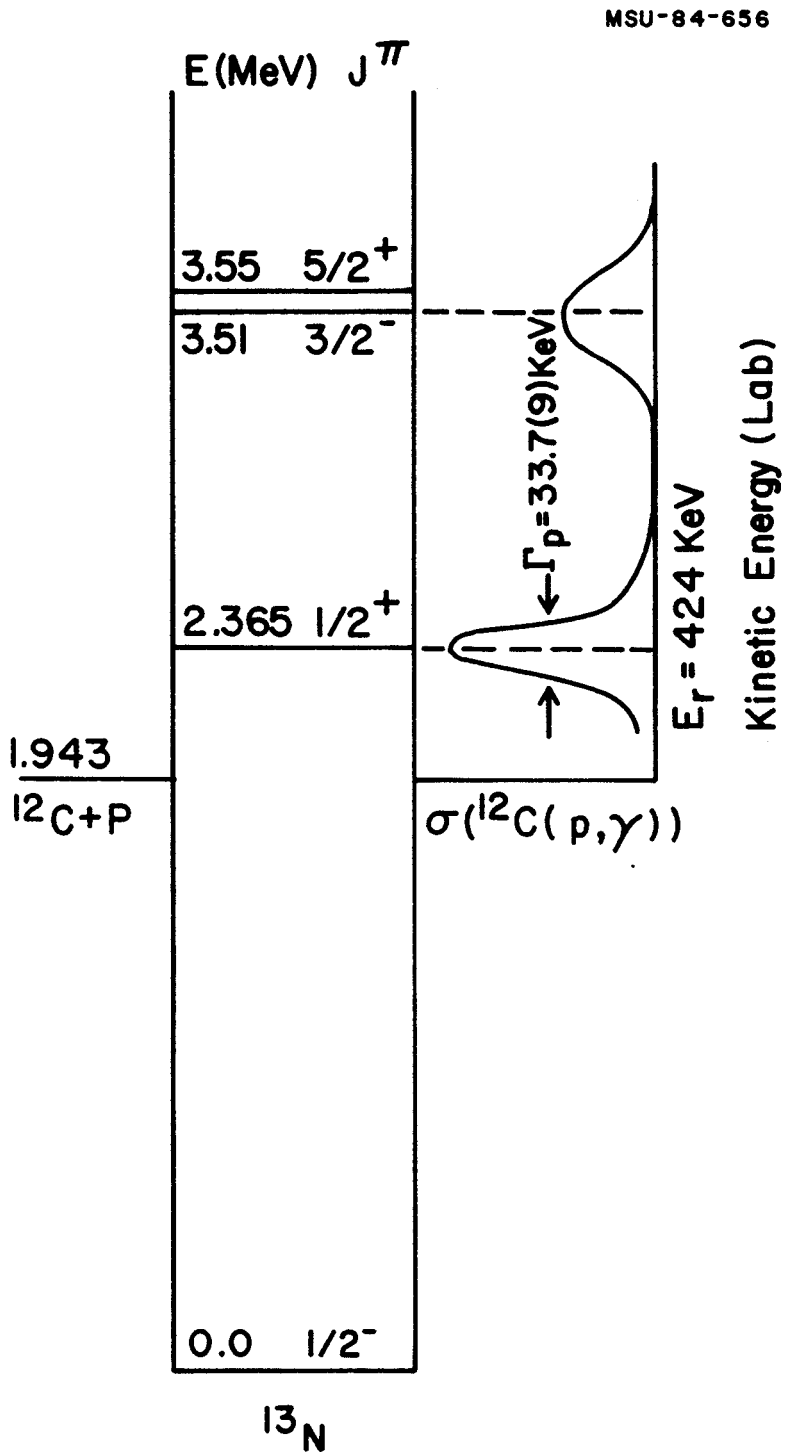

Figure 5-2: The effect of the structure of ^{13}N on $^{12}C(p,\gamma)$ resonances. The data is taken from Ajzenberg-Selove (Aj81).

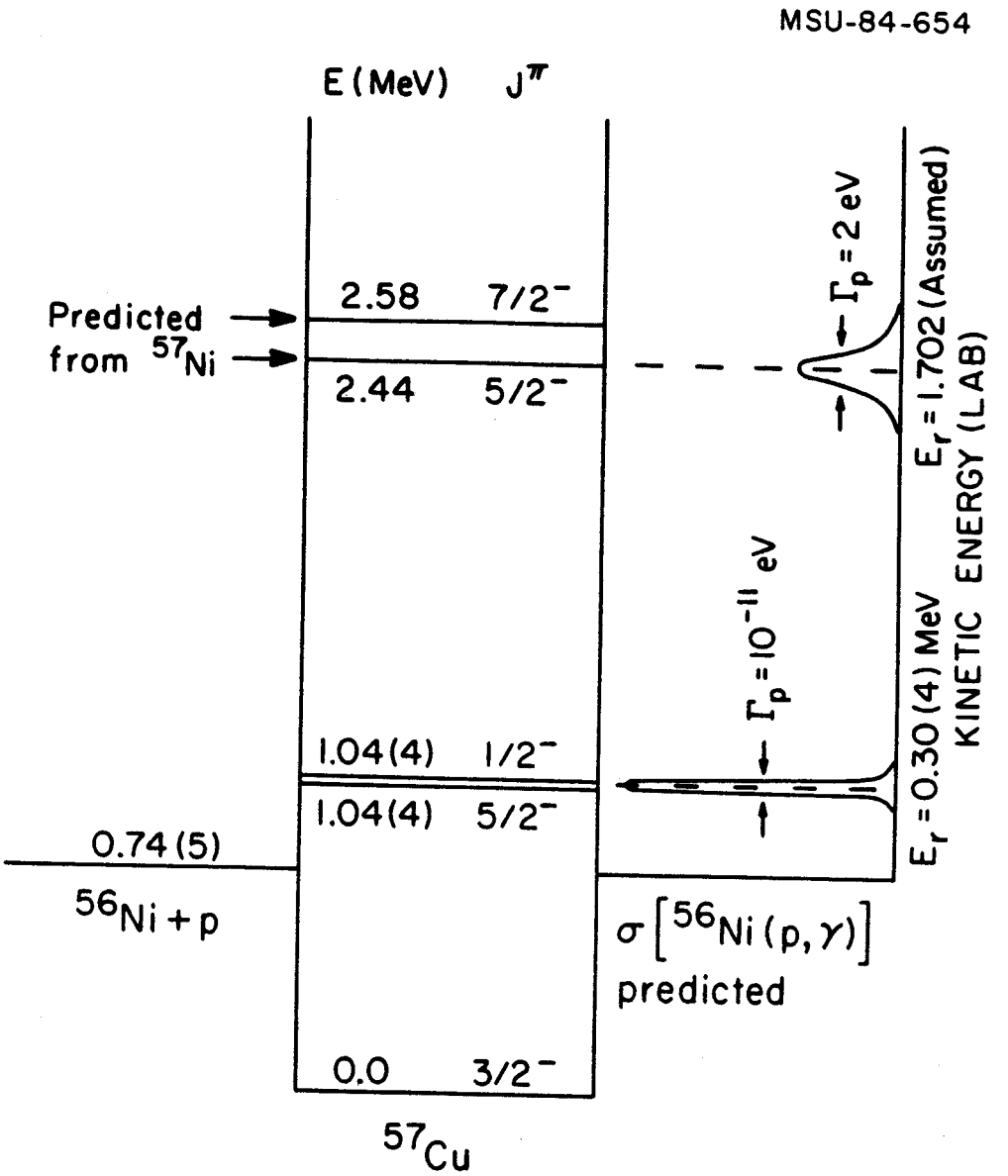

Figure 5-3: The predicted effect of the structure of ^{57}Cu on ^{56}Ni(p,γ) resonances.

where E is the energy in the particles center of mass, $\Psi(E)$ is the velocity distribution, $\sigma(E)$ is the cross section, and $v(E)$ is the relative velocity. Since the widths of the resonances which we will consider are less than 10 eV, $\Psi(E)$ and $v(E)$ do not change much over this energy range. Hence we have

$$\lambda_{12} = \Psi(E_r)v(E_r) \times \int_0^\infty \sigma(E)dE \qquad (5.4)$$

Next, if we assume the resonance has a Breit-Wigner shape (B152) with $\Gamma = \Gamma_1 + \Gamma_2$, where Γ_x is the decay width for the decay x ;

$$\sigma_{12} = (2l+1)\pi\lambda^2 \times \frac{\Gamma_1 \Gamma_2}{(E-E_r)^2(\Gamma/2)^2} \qquad (5.5)$$

We can evaluate the integral again under the assumption of a narrow resonance. We find

$$\int_0^\infty \sigma(E)dE = 2\pi^2\lambda_r^2\omega \ (\Gamma_1\Gamma_2/\Gamma) \qquad (5.6)$$

and hence that

$$\lambda_{12} = 9.30\times10^{4\,0}\omega(AT_9)^{-3/2}(\Gamma_1\Gamma_2/\Gamma) \times \exp(-11.605\ E_r/\ T_9) \qquad (5.7)$$

where E_r is in MeV, the decay widths are in keV, and A is the reduced A of the system. It is immediately obvious that

a change in the resonance energy will significantly affect λ_{12} due to the exponential dependence on E_r. However less obvious, changing the resonance energy will also change the decay width Γ_x.

The decay width of a given state is determined from

$$\Gamma_i = h/2\pi\tau_i \qquad (5.8)$$

where τ_i is the mean lifetime for the state to the decay of type 1. If the lifetime for a given decay can be measured, then Γ_i can be determined. In the case of ^{57}Cu's excited states the Γ_γ widths can be reliably taken from the known γ lifetimes of the excited states in ^{57}Ni (Le78). The energy spacing in ^{57}Cu is different than in ^{57}Ni and hence the gamma energies will be different. The energy dependence is given by (B152)

$$\Gamma_\gamma \propto [\ E_\gamma(\mathrm{MeV})\ ]^{2l+1} \qquad (5.9)$$

However we see that if $\Gamma_p \ll \Gamma_\gamma$, then

$$\Gamma_p\ \Gamma_\gamma\ /\ \Gamma\ \approx \Gamma_p \qquad (5.10)$$

For the most dominant resonance we will consider this will be true. Thus we need only consider Γ_p. Since the proton decay lifetime is unknown and would be hard to measure, we

must calculate Γ_p. The width Γ_p can be evaluated from (see Clayton (C168) equation 4-121)

$$\Gamma_p = (3hv/R)P_l\theta_l^2 \qquad (5.11)$$

where v is the particle velocity at infinity, R is the interaction radius, P_l is the penetrability for a state with angular momentum l, and θ_l^2 is the reduced width of the state. The velocity v is determined strictly from the difference between the excited state energy and the excitation energy for the (A-1,Z-1) + p system. The reduced width is usually written

$$\theta_l^2 = \frac{R}{3} \left| \chi_l(R) \right|^2 \qquad (5.12)$$

$$\Psi(r,\theta,\phi) = Y_l^m(\theta,\phi)\ \chi_l(r)/r \qquad (5.13)$$

where $\Psi(r,\theta,\phi)$ is the exact wave function for the decaying particle, which must be deduced from the complete nuclear potential. Since this factor is in general difficult to determine, WW assumed $\theta_l^2 = 0.1$ for all states. Since we are only interested in seeing how the new resonance energy data effects the previously calculations, we will also follow this assumption.

The penetrability, P_l, is defined as

$$P_l = \frac{|\chi_l(\infty)|^2}{|\chi_l(R)|^2} \qquad (5.14)$$

which is just a measure of the probability the particle escapes once it is at the position R. The penitrabilities are easier to calculate than the reduced widths because $\chi_l(r)$ is well known for r>R and are the so called "Coulomb partial waves" (Fr55). Thus, to determine P_l we pick a value at R and integrate $\chi_l(r)$ as $r\to\infty$ to determine P_l (Be84,C168). Another approach, which we will use, shows the energy dependence of P_l. In this case $\chi_l(r)$ is evaluated using the WKB approximation (see Schiff section 34 (Sc68)). With this approximation it is possible to show that to order (E/E_c)

$$P_l \approx (E_c/E)^{.5} \times \exp(-bE^{-.5} + 1.05(ARZ_1Z_2)^{.5} - 7.62(l+.5)^{.5}(ARZ_1Z_2)^{-.5}) \qquad (5.15)$$

where

$$E_c = 1.44(\text{MeV-fm})Z_1Z_2/R \qquad (5.16)$$

and A is the reduced A, and $b=31.28Z_1Z_2A^{1/2}(\text{keV}^{1/2})$. There are two important observations to be made on equation (5.15). First, the energy dependence goes as $\exp(-b/E_r^{1/2})$, which will tend to oppose the energy dependence from the Boltzmann velocity distribution of the protons. The strong

energy dependence in the penetrability comes from the reduction in the width as the resonance energy is lowered. In the case of ^{56}Ni(p,γ) changing the resonance energy from 420 keV to 300 keV has the effect of moving the classical turning point from 96 fm to 134 fm. Considering the interaction radius in on the order of 4 fm, it is easy to see the origin of the strong energy dependence and the very narrow proton decay width which we will find for the ^{57}Cu low-lying states. Second, there is a strong dependence on the l of the state. In fact in ^{57}Cu where an l=1 and an l=3 state lie at about the same excitation, the penetrability will be a factor of 2.5 larger for the l=3 state.

Using the results of the previous paragraphs we find the full energy dependence of λ_{12} is

$$\lambda_{12} \propto \exp(-bE_r^{-1/2}) \times \exp(-11.605\ E_r/T_6) \qquad (5.17)$$

where E_r is expressed now in keV. To determine λ_{12} accurately it is necessary to know E_r well. The strong energy dependence magnifies any uncertainty in the resonance energy.

5.4.3 Photodisintegration Rates

One other effect will change the rate of production of ^{57}Cu. This effect is the breakup of the compound system through photodisintegration, the (γ,p) reaction. If the Q

value for breakup is lower (higher), it will be easier (more difficult) for breakup to take place. Thus, the photodisintegration rate depends on the Q value for the $^{57}Cu \rightarrow {}^{56}Ni + p$ reaction. We will write this Q value as $Q_{\gamma p}(^{57}Cu)$.

To see the Q dependence of the (γ,p) reaction, consider an equilibrium system with number densities of ^{57}Cu, $n_{^{57}Cu}$; ^{56}Ni, $n_{^{56}Ni}$; and protons, n_p. In this case we must have

$$\lambda_\gamma \, n_{^{57}Cu} = \lambda_{p\gamma} \, n_{^{56}Ni} \, n_p \qquad (5.18)$$

Hence, we get

$$\lambda_\gamma = \frac{n_{^{56}Ni} n_p}{n_{^{57}Cu}} \times \lambda_{p\gamma} \qquad (5.19)$$

The factor involving the number densities in equilibrium is given by the Saha equation (Sa20). Hence, we see

$$\lambda_\gamma = N_A \, 4.805 \times 10^9 \, T_9^{3/2} \exp(-11.605 \, Q_{\gamma p}(^{57}Cu)/T_9) \times \lambda_{p\gamma} \, . \qquad (5.20)$$

Since λ_γ depends only on the photon density, which is only a function of the temperature, the above equation must also be the expression for number densities not in equilibrium.

Therefore, equation 5.20 also gives the $Q_{\gamma p}$ dependence of the photodisintegration rate for the rp-process.

5.5 Comparison to the Previous Calculations

Wallace and Woosley (Wa81) describe their parameterization of the $\lambda_{p\gamma}$ and $\lambda_{\gamma p}$ rates in section (d) of appendix A of their paper. They write

$$\lambda_{p\gamma} = N_A \times T_9^{-3/2} \sum_i A_i \exp(-B_i/T_9) \qquad (5.21)$$

and

$$\lambda_{\gamma p} = N_A \times C T_9^{3/2} \lambda_{p\gamma} \exp(-D/T_9) \qquad (5.22)$$

The parameters A,B,C, and D are given in WW's Table 11. The important parameters assumed by WW compared to the measured values are shown in Table 5-2. Due to the Coulomb shift of the $5/2^-$ level our study shows there is an l=3 resonance at about the same energy as the l=1 resonance. However the larger angular momentum barrier will reduce its importance. If however this level is slightly lower in excitation, then it could conceivably be the dominant resonance by which ^{57}Cu is made. The present data however do not indicate this to be true, but are not conclusive. Wallace and Woosley also included in their calculations a resonance at 1.702 MeV on which our study has no information. However, photodisintigration of ^{57}Cu dominates its production at temperatures $T_9 > 1.0$ at which this resonance would be important. Therefore we will consider only the effect of the lower resonances, and assume the cross section is dominated by the l=1 resonance.

Table 5-2: Comparison of the old and the new parameters relevant to the $^{56}Ni(p,\gamma)^{57}Cu$ rate calculation.

Parameter	WW(Wa81)	New
A_1/N_A	1.29(-2)	4.6(-6)
B_1	4.897	3.481
A_2/N_A	7.065(3)	5.27(3)
B_2	20.33	19.75
C/N_A	4.805(9)	same
D	8.02	8.70
E_r^1	0.422 MeV	0.300 MeV
E_r^2	1.752 MeV	1.702 MeV
Γ_p^1	8.17(-8) eV	2.9(-11) eV
Γ_p^2	2.06 eV	1.54 eV
Γ_γ^1	5.7(-3) eV	4.7(-3) eV
Γ_γ^2	1.5(-2) eV	same

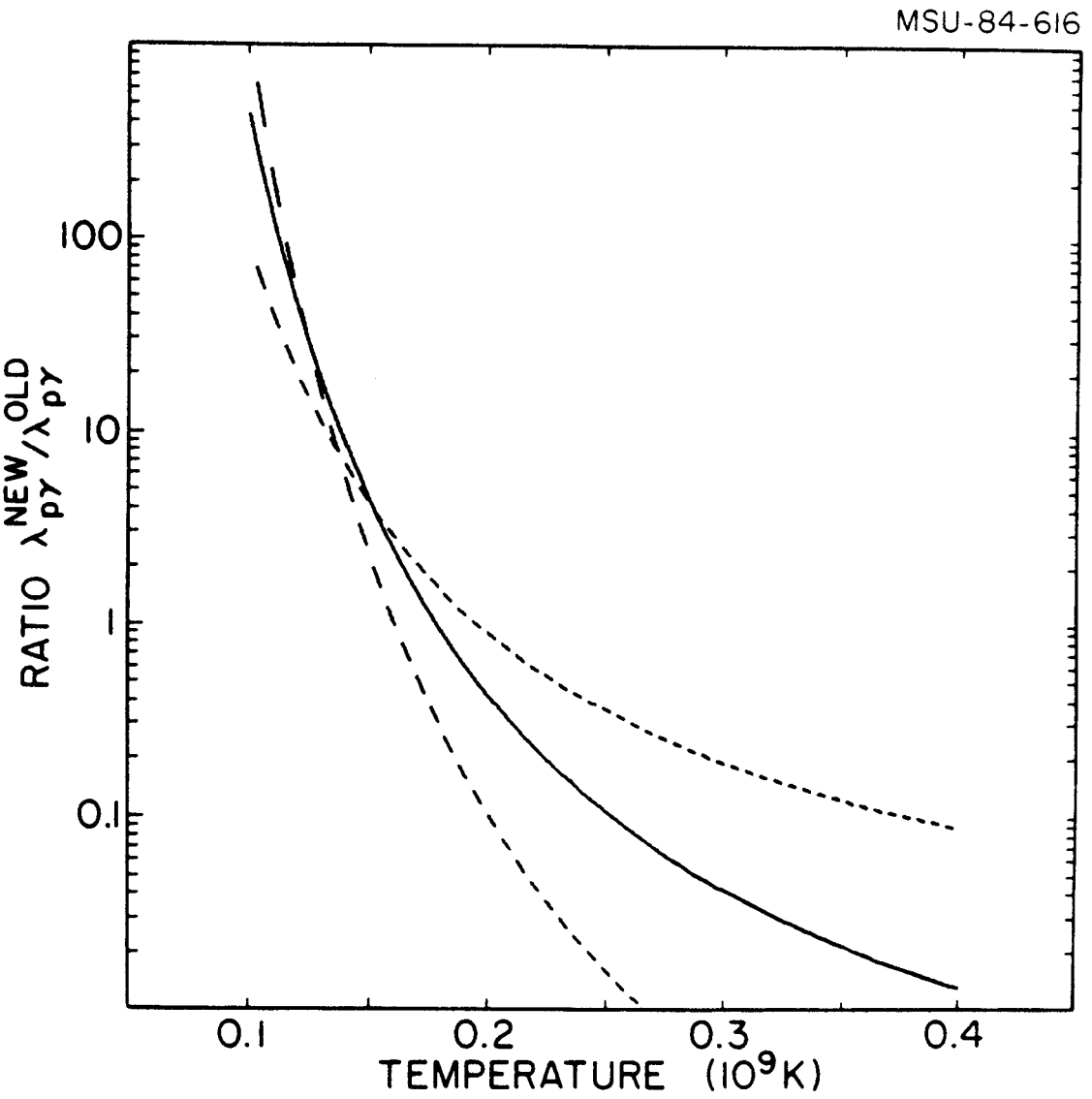

Figure 5-4: The ratio of the recalculated $^{56}Ni(p,\gamma)^{57}Cu$ rate in units of cm^3/mole-sec to the previously calculated rate vs. temperature. The dashed lines were calculated by varying the resonance energy by the uncertainty in the measurement, ±40 keV.

The ratio of the recalculated $^{56}Ni(p,\gamma)^{57}Cu$ rate to the previously calculated rate vs. temperature is shown in Figure 5-4. The dashed lines were calculated by varying the resonance energy by the uncertainty in the measurement, ± 40 keV. As we have seen, the deviation from unity is due to the narrower proton decay width of the resonance, and the decreased resonance energy. The effect of the change in the $Q_{\gamma p}$ value is to increase the temperature at which photodisintegration would dominate production.

Without repeating the full calculation of WW it is difficult to determine the exact effect of the new results on the calculations of phenomena discussed in the introduction to the rp-process although it is clear a recalculation is justified. We can study the effects in some limiting cases. To do this we write the time rate of change of ^{57}Cu as

$$\frac{dn}{dt}_{^{57}Cu} = n_{^{56}Ni} n_p \lambda_{p\gamma}(^{57}Cu) - n_{^{57}Cu}\lambda_{\gamma p}(^{57}Cu) - n_{^{57}Cu}\lambda_{\beta}(^{57}Cu) - n_{^{57}Cu} n_p \lambda_{p\gamma}(^{58}Zn) \qquad (5.23)$$

We will consider first a simple case in which the temperature remains such that $\lambda_{\gamma p} << \lambda_{p\gamma}$. We will also assume, as was done by WW, that $\lambda_{p\gamma}(^{58}Zn)$ is small. This assumption is questionable since the Garvey-Kelson charge symmetric mass relation used in chapter 3 predicted that

^{58}Zn is proton bound by 2.25 MeV, and based on the structure of ^{58}Ni, the analog of ^{58}Zn, there will be a proton resonance at around 200 keV. This low resonance energy may give $\lambda_{p\gamma}$ rates which will compete with β-decay. However using the assumption of WW we get

$$\frac{dn}{dt}^{57}Cu = n_{^{56}Ni} n_p \lambda_{p\gamma}(^{57}Cu) - n_{^{57}Cu}\lambda_{\beta}(^{57}Cu) \qquad (5.24)$$

Since only photodisintegration can inhibit flow to A>57, we see that the flow is strictly determined in this case by $\lambda_{p\gamma}$. Figure 5-4 shows the size of the effect versus reaction temperature. If we assume T_9~ constant so that $\lambda_{p\gamma} \neq \lambda_{p\gamma}(t)$, and we have an inexhaustable bath of ^{56}Ni and protons so that there number densities do not depend on time, then we find

$$n_{^{57}Cu}(t) = \frac{n_{^{56}Ni} n_p \lambda_{p\gamma}}{\lambda_{\beta}} \times (1 - \exp(-\lambda_{\beta} t)) \qquad (5.25)$$

Clearly, we have $n_{^{57}Cu}(t) \propto \lambda_{p\gamma}$. From Figure 5-4 we see that for most temperatures $\lambda_{p\gamma}^{new} < \lambda_{p\gamma}^{old}$, so we would predict less production of A>56 elements.

The other extreme is where $n_p n_{^{56}Ni} \lambda_{p\gamma} << n_{^{57}Cu}\lambda_{\gamma p}$. In this case it is clear the only solution is $n_{^{57}Cu}(t) \approx 0$.

The only question is whether ^{57}Cu β-decays before it undergoes photodisintigration. If again we assume the $\lambda_{p\gamma}(^{58}Zn)$ rate is small, then the branching ratios for β-decay and photodisintigration will be given by

$$B_{^{56}Ni} = \frac{\lambda_{\gamma p}(^{57}Cu)}{\lambda_{\gamma p}(^{57}Cu)+\lambda_{\beta}(^{57}Cu)} \tag{5.26}$$

and

$$B_{^{57}Ni} = \frac{\lambda_{\beta}(^{57}Cu)}{\lambda_{\gamma p}(^{57}Cu)+\lambda_{\beta}(^{57}Cu)} \tag{5.27}$$

Although these could be evaluated, it is simpler to consider the superratio

$$R = \frac{(B^{new}_{^{56}Ni} / B^{new}_{^{57}Ni})}{(B^{old}_{^{56}Ni} / B^{old}_{^{57}Ni})} \tag{5.28}$$

The ratio R gives the change in the relative amount for flow to A>56 between the old and the new calculations. It is easy to see R will be given by

$$R = \frac{\lambda^{new}_{p\gamma}(^{57}Cu)}{\lambda^{old}_{p\gamma}(^{57}Cu)} \times \exp(-11.605(Q^{new}_{\gamma p} - Q^{old}_{\gamma p})/T_9) \tag{5.30}$$

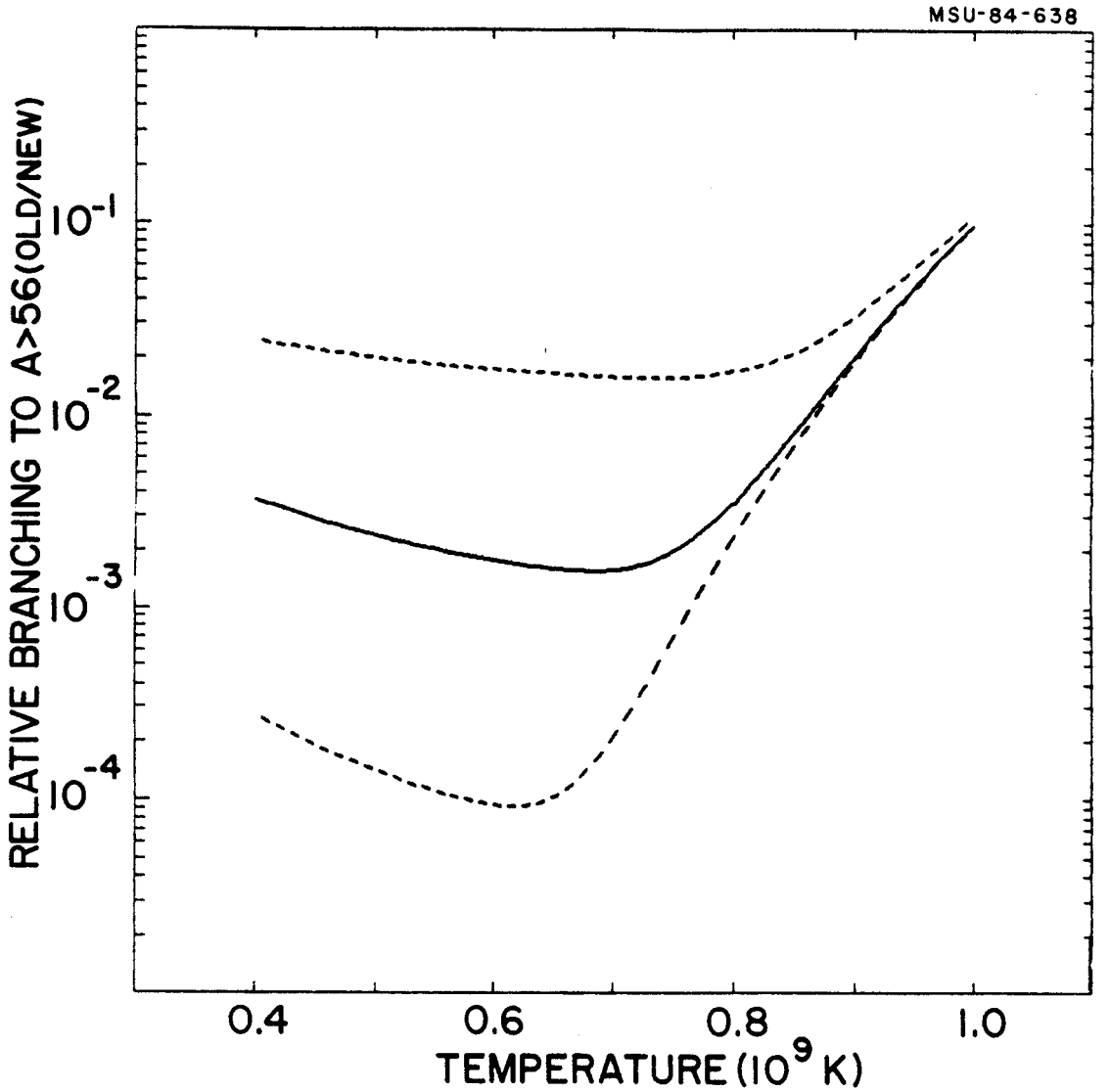

Figure 5-5: Superratio of branching to A>56 vs. temperature. The dashed lines were calculated by varying the resonance energy by the uncertainty in the measurement, ±40 keV.

The ratio is plotted versus temperature in Figure 5-5. The effect of the 1.702 MeV resonance is seen at higher T, since both calculations give almost the same rates when this resonance dominates. It is clear that the new data indicate that whatever ^{57}Cu is made, much more is processed to higher A. Again the dashed lines were calculated by varying the resonance energy by the uncertainty in the measurement, ± 40 keV. The strong sensitivity of the superratio to the exact resonance energy indicates the need for a more accurate determination of the $1/2^-$ and $5/2^-$ excitation energies. As seen in the figure, an uncertainty of 40 keV in the excitation energy of the $1/2^-$ state leads to a factor of 100 uncertainty in the superratio.

5.6 Conclusions

It is interesting that in the two limits considered the effects are exactly opposite. In the limit that photodisintegration is small, we saw the flow above A>56 was reduced relative to the previous calculations. In the other limit although the production is still down, more of the flow continues to higher A. This indicates again that a complete recalculation with the full network is necessary to understand fully the effect the new data will have on astrophysical models. Although the uncertainty in the atomic mass and level structure of ^{57}Cu leads to some

uncertainty in the exact rates of ^{57}Cu production and photodisintegration, the new data will make the recalculation of this important branch point in the rp-process more reliable than the calculations based on assumptions of the nature of ^{57}Cu. However, future study of ^{57}Cu should be attempted to further reduce the uncertainties in rp-process calculations.

CHAPTER SIX

The atomic mass excess of ^{57}Cu and ^{59}Zn have been determined by measuring the Q values of the reactions ^{58}Ni(^{7}Li,^{8}He)^{57}Cu, Q=-29.56(5) MeV, and ^{58}Ni(p,π^-)^{59}Zn, Q=-144.74(4) MeV. The measured masses agree with the predictions from standard models (Ma76). The new masses have been used to predict the mass excesses for lighter Cu and Zn isotopes using the Garvey-Kelson charge symmetric mass relation (Ke66). We predict that the lightest particle stable Cu isotope is ^{56}Cu, and the lightest Zn isotope is ^{54}Zn.

The superallowed Gamow-Teller β decays of these T_z=-1/2 nuclei show evidence for strong quenching of the $\sigma\tau$ matrix elements relative to shell model calculations. A quenching of 0.78 has been observed for s-d shell nuclei (Br83b), however the quenching for ^{57}Cu and ^{59}Zn decays is ~0.5. The increased quenching could be due to inadequacies in the shell model calculation, such as higher order configuration mixing in the ^{56}Ni core. The quenching could also come from an A dependence of the quenching mechanisms.

Presently the increased quenching is not understood. The most likely explanation is higher order mixing in the ^{56}Ni core, although as stated in chapter 2 there is some reason to believe this is not the cause.

The masses of ^{57}Cu and ^{59}Zn also provided further data to study the Nolen-Schiffer anomaly (No69). In particular the single particle nature of ^{57}Cu was used to study extensively the nuclear structure corrections which may explain the anomaly. The ^{57}Cu and ^{59}Zn data were compared to other data from mirror nuclei between A=39 and A=59. In all cases there was an approximately 10% discrepancy between the calculated and measured Coulomb displacement energies. This discrepancy seems to be strong evidence for charge asymmetric forces in nuclei. Before definite conclusions can be drawn on the size of the effect, further evidence from scattering lengths or other tests of charge symmetry are necessary.

The structure of ^{57}Cu was also used to recalculate rp-process flow above A=56. There are several astrophysical environments where such flow is important, as was outlined in chapter 5. We find a significant reduction in the ^{56}Ni(p,γ)^{57}Cu rate compared to the rates calculated by Wallace and Woosley (Wa81) based on an assumed ^{57}Cu structure taken from ^{57}Ni. To understand the effects fully, a complete recalculation of the rp-process in the particular environment to be studied, including the time dependent densities of ^{56}Ni, p , and ^{57}Cu, is necessary. However, in

the limits studied in chapter 5 we find evidence that the recalculations will show significantly different results.

These mass measurements also demonstrate the feasibility of using complicated reactions to study nuclear masses and energy levels of nuclei many neutrons from β stability. Even in the case of the $^{58}Ni(p,\pi^-)^{59}Zn$ reaction for which the cross section was only 0.08 nb/sr, we were able to measure a mass. A quick survey of reactions and targets shows that there are at least 15 nuclei with unknown masses and A<80 which could be studied using the S320 spectrograph. There are many more nuclei with known masses but little known about their level structure which could also be studied using transfer reactions. The techniques and procedures developed for this thesis should be useful for such studies.

APPENDICES

APPENDIX A

A.1 Background

The K500 cyclotron is capable of producing beams of particles with energies, E/A, up to 80 MeV. The Enge spectrograph (Sp67) has a K parameter of 120. This means it can bend particles up to E/A=30 MeV particles ($E/A=K \times (Q/A)^2$). Hence to use fully the available energy from the K500 cyclotron a K=320 spectrograph was designed and built. To keep costs low, it was constructed from existing components. In this way it was possible to complete the spectrograph for a fraction of the cost of a spectrograph consisting of new components. The price paid is in somewhat poorer resolution and smaller solid angle than that for an optimized device. However, with the addition of correcting magnetic elements it was possible to build a device with adequate parameters.

In this appendix the design of the simple K=320 spectrograph, called the S320, will be described. The discussion first will include a brief description of the mechanical design of the spectrograph. Next, some

introduction to spectrograph optic notation and the program used for the optical design of the S320, MOTER, will be presented. The final optical design will then be presented. Finally, the preliminary experimental results will be presented and compared to the predicted design. The S320 detector has been described in chapter 2 and elsewhere (Pl83,Yu82), and will not be discussed here.

A.2 Mechanical Design

A top view of the spectrograph is shown in Figure 2-1. The magnetic dipole used is a standard High Voltage Corporation MP tandem switching magnet which was obtained from the University of Pennsylvania Tandem Laboratory. The only modification required on this magnet, which will be explained later, was a change in the entrance edge curvature from a radius of -0.3 m (concave) to +0.78 m (convex). The angular range of the spectrograph is -10 deg to +60 deg. When located at zero degrees, this dipole also serves as a switching magnet to the ENGE spectrometer and the scattering chamber for neutron studies. The quadrupole doublet, which has an 8 inch aperture, became available as a result of the closing of the Space Radiation Effects Laboratory (SREL) cyclotron. A precision scattering chamber with a sliding seal was obtained on loan from the University of Minnesota. The sextupole magnet for this spectrograph was designed and constructed at the NSCL (Ha81a,No81). It is a scaled-up version (6 inch aperture) of the 3 inch and 4 inch sextupoles used in the beam transport system of the K50

cyclotron but used hollow, water-cooled conductor rather than the solid, air-cooled wire used in the smaller sextupoles. The pole tip of the new sextupole also has an improved shape determined via a conformal mapping calculation(Ha81a). An additional magnet was included between the dipole and sextupole to correct for 3rd order aberrations in the spectrograph optics. The need for and the design of this magnet are described in appendix B.

The physical parameters of the device are listed in Table 2-1. The defining aperture is located approximately 2 m from the target directly in front of the first quadrupole. This feature allows cleaner operation near zero degrees and makes the use of an active collimater easier. The primary use of the sextupole was to allow the focal plane to be perpendicular to the particle's path, which simplifies the detector design. The solid angle of the device, 0.56msr, is limited by the dipole gap. Finally, the spectrograph is designed to correct for reaction kinematics and dispersion matching to improve energy resolution. Before these features can be discussed some background is necessary.

A.3 Magnetic Optical Background

A.3.1 Notation

Consider the coordinate system shown in Figure A-1, where S is some system of magnetic elements. The orbit is defined on Serret-Ferenet coordinates.

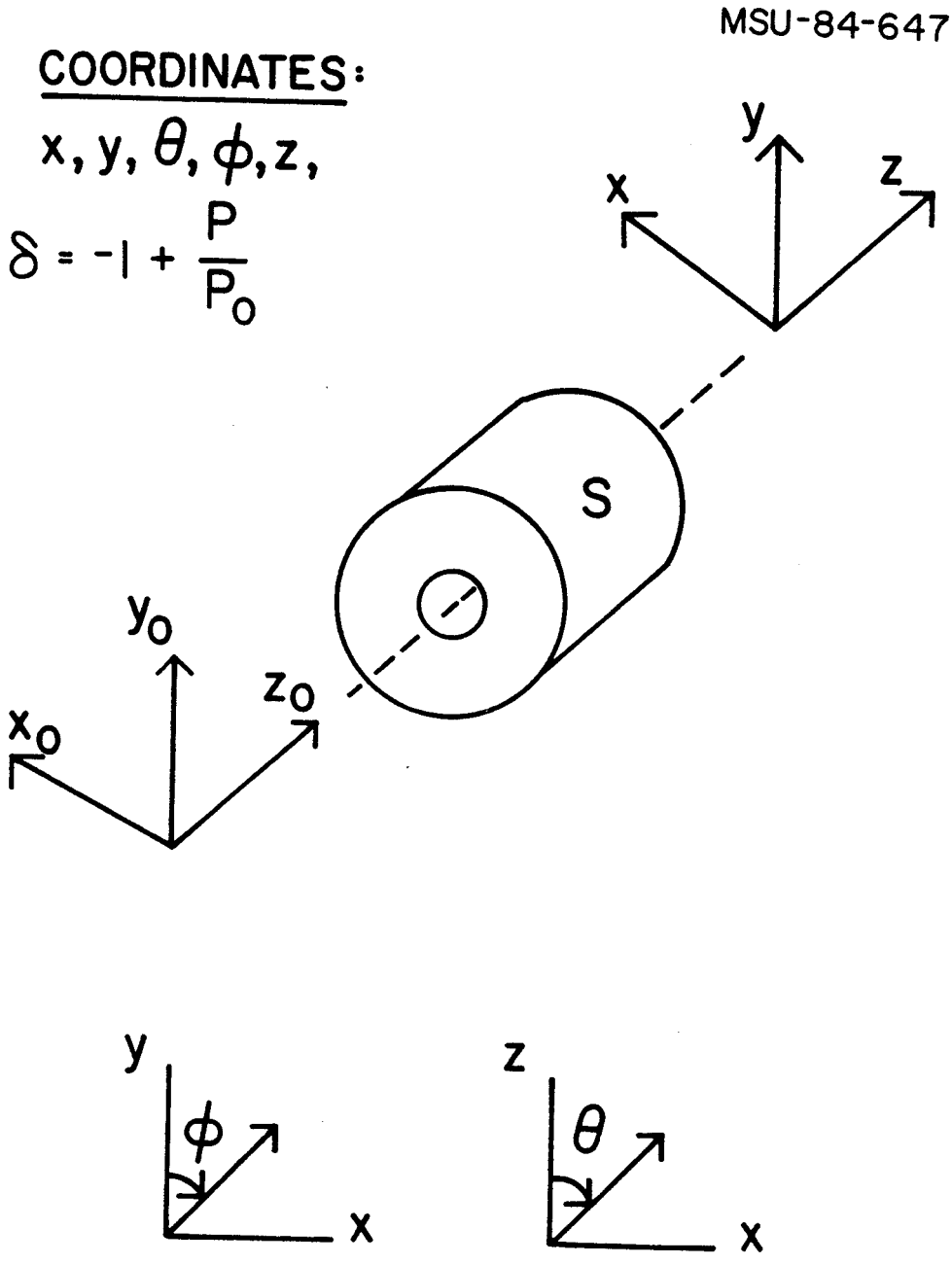

Figure A-1: Coordinate system for magnetic optical notation.

That is, the coordinate system is defined relative to a reference orbit which travels through the center of the spectrograph. This orbit is called the "central ray". The coordinates are thus a function of l, the arc length along the central ray. The parameter δ is defined as $\delta = (P - P_0)/P_0$, where P_0 is the momentum of the central ray.

Since one is in general interested in the position of a given ray at the focal plane as a function of the initial parameters, we write

$$x_f = f(x_0, y_0, \theta_0, \phi_0, \delta) \qquad (A.1)$$

(likewise for y, θ, ϕ, and δ). We can expand the final coordinates in a Taylor's expansion about the central ray as a function of the initial coordinates. For example for x_f this would be

$$x_f = (x/x)x_0 + (x/\theta)\theta_0 + (x/\phi)\phi_0 + (x/\delta)\delta_0 + (x/y)y_0 + \text{higher order terms} \qquad (A.2)$$

where we have defined

$$(x/x_0^i y_0^j \theta_0^k \phi_0^l \delta_0^m) = \frac{1}{(i+j+k+l+m)!} \times \frac{\partial^{i+j+k+l+m} x_f}{\partial^i x \, \partial^j y \, \partial^k \theta \, \partial^l \phi \, \partial^m \delta} \qquad (A.3)$$

The sum i+j+k+l+m determines the order of the term; first, second, third, and so on.

The expansion can be simplified somewhat by noting that for a system with median plane symmetry we must have

$$(x/y^i\phi^j) = 0 \qquad (A.4)$$

where i+j is odd. Thus, to second order we can expand x_f as

$$x_f = (x/x)x_o + (x/\theta)\theta_o + (x/\delta)\delta + (x/\theta^2)\theta_o^2 + (x/\phi^2)\phi_o^2 + (x/\theta\phi)\theta_o\phi_o + (x/\theta\delta)\theta_o\delta_o + (x/\delta^2)\delta^2 + (x/\phi y)y_o\phi_o + \text{higher order terms} \qquad (A.5)$$

The focal plane can be defined to be at the first order focus, where $(x/\theta) = 0$. However in general it is defined where the sum of the aberration terms is a minimum. Some of the above terms have special meaning. We see (x/x) is the first order magnification, and (x/δ) is the dispersion. Thus, we can write the first order resolving power of the system, defined as the inverse of the fractional change in momentum needed to displace the first order image a distance equal to its width, as

$$R = \frac{P}{\Delta P} = \frac{(x/\delta)}{(x/x)\Delta x_o} \qquad (A.6)$$

If we examine some of the higher terms, we note that the term (x/δ^2) and others of the form (x/δ^n) produce a nonlinearity in the dispersion at the focal plane. This may

not in general be desirable but is easily included in the spectrograph calibration.

The term $(x/\theta\delta)$ can be shown to be related to the focal plane angle, ψ, between the z-axis and the normal to the focal surface

$$\tan \psi = \frac{-(x/\theta\delta)}{(\theta/\theta)(x/\delta)} \qquad (A.7)$$

Higher order terms of the form $(x/\theta\delta^n)$ produce curvatures of the focal surface which could be corrected for with a strange focal plane curvature.

The most important terms are the aberration terms (x/θ^2), (x/ϕ^2), (x/θ^3), $(x/\theta\phi^2)$ and so on, since they lead to a blurring of the image formed of the target spot and lead to worse energy resolution. If we let Δx represent an appropriate measure of the increase in width of the image due to these aberrative terms, the obtainable resolving power becomes

$$R = \frac{(x/\delta)}{(x/x)\Delta x_0 + \Delta x} \qquad (A.8)$$

In our discussions so far, we have mainly considered the effects of aberrations in the dispersive x-direction. these are of primary importance since they have a direct effect on the resolution. In many cases the aberrations in

the y-direction are also important. Some spectrographs make use of both x and y coordinates together with angle measurements at the focal plane for purposes of software corrections both for kinematic and uncorrected optical abberations. For example this was done in the case of the mass measurement described in chapter 3, and will be used in the S800 spectrograph (Ze82) to obtain resolution of $P/\Delta P=20000$. For a more detailed description of optics theory see (En79) or (Br70).

A.3.2 Magnetic Optics Calculations

There are two general categories of computer codes for magnetic optics calculations. First there are codes which treat the terms in the Taylor's expansion as elements of a matrix and determine the optical parameters of a device by matrix manipulations. TRANSPORT (Br77b) is a well known example of this type of program. The major problem with these codes is that they are limited to 2nd or 3rd order terms in the expansion. The other category of program takes as input the magnetic fields of the elements and integrates the equation of motion of a test particle traveling through the system to determine the final particle position. Programs of this type are RAYTRACE (Ko81) and MOTER (Th79). Since MOTER was used extensively in the final S320 design it will be described briefly. In actuality, the initial designs of the S320 were done with TRANSPORT and TURTLE

(Br74). The designs were then checked and improved with RAYTRACE, and the final design was optimized with MOTER.

MOTER integrates the equation of motion for a test particle through the system to determine the final particle coordinates at the end of the system. It does a Monte Carlo simulation of the user defined phase space by picking rays at random within the phase space and tracing them through the system. MOTER then will optimize up to 40 spectrograph parameters to improve resolution. The optimization is done by minimizing χ^2 where χ^2 is calculated from the difference between the final position of a given ray and the expected final position.

One of the useful features of MOTER is that it allows a given dependence of a parameter, at the focal plane, on the initial parameters to be evaluated and subtracted from the results which are used for the χ^2 determination. For example suppose one wanted to optimize the x spot size at the focal plane. Since $x_f \propto (x/\delta)\delta$, a phase space with a range of δ would result in an optimization which would tune magnets to reduce (x/δ). This is not a desirable result for a spectrograph since the resolution depends on (x/δ). MOTER however allows us to define

$$x' = x_f - (x/\delta)\delta - (x/\delta^2) - \ldots \qquad (A.9)$$

and will determine the coefficients (x/δ^n) by fitting x_f vs. δ with a function of order n. MOTER then optimizes the spectrograph parameters to reduce $\Delta x'$. In this way the

optimization can be performed while including the spectrograph's full momentum acceptance. In practice it is easier to consider $\delta = \delta(x_f)$ and minimize $\delta_{residual} = \delta - \delta_{predicted}$, where

$$\delta_{predicted} = (\delta/x)x_f + (\delta/x_f^2)x_f^2 + \ldots \qquad (A.10)$$

The full width at half maximum of the resulting residual momenta, $\delta_{residual}$, gives directly the momentum resolution of the device since $R = P/\Delta P = \Delta\delta_{residual}$.

A sample calculation for the S320 spectrograph, assuming $\Delta\theta=\Delta\phi=12$mr, $\Delta y=3$mm, $\Delta x=2$mm, and a momentum range of 5% is shown in Figure A-2. The distribution is fitted with a Gaussian and the resulting FWHM yeilds $P/\Delta P = 3500$ for the spectrograph running in the energy loss mode with a beam energy spread of 0.10%. This is actually the worst case resolution which should be expected at any point in the S320 focal plane since the calculation includes the full focal plane. The resolution at certain places may be better.

The option of being able to specify a dependence of one parameter on another is useful in areas other than optimizing resolution. It is possible to fix coefficients to a preset, or known value.

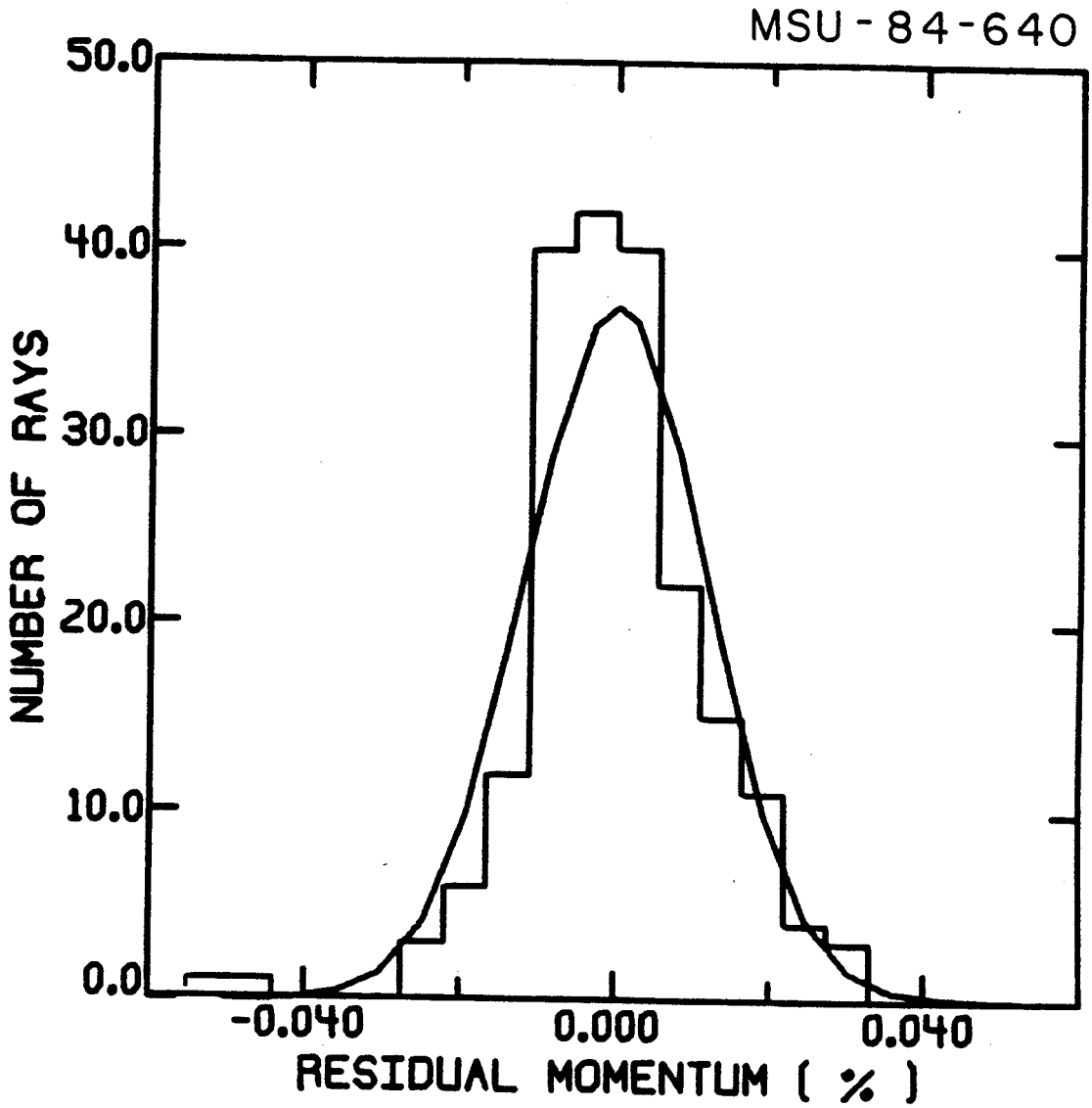

Figure A-2: Sample MOTER calculation showing the residual momentum vs. the number of rays. The FWHM of the peak gives the predicted S320 resolution.

This allows the effects of reaction kinematics, which is a known (θ/δ) correlation, to be explicitly included in the calculation and hence in the optimization. It also allows the dispersion matching feature of the device to be checked by including a known (δ/x_0) correlation to a given rays momentum. The results of these types of calculation will be described in the next section.

MOTER has many other features which were not used for the S320 study and hence will not be discussed. For a complete description of the program and options see the MOTER manual (Th79).

A.4 S320 Optical Design

The optical design parameters of the S320 are listed in Table 2-1. A schematic diagram of the component layout and first order beam envelopes calculated by TRANSPORT are shown in Figure A-3. The major goals for the design were a 0.56 msr solid angle with $E/\Delta E = 1000$, and an energy range of 20%. To achieve these goals several modifications and additions were necessary to the major used components acquired for the spectrograph. The first was the addition a sextupole to correct the large focal plane tilt, ~ 89 deg, caused by a large ($x/\theta\delta$) term.

Table A-1: Optimized S320 spectrograph parameters for the QQDMS and the QQDS configurations.

Parameter	Optimized value	
	QQDS	QQDMS
y-quad (kG)	-8.55	-8.55
x-quad (kG)	7.14	7.17
Sextupole (kG)	1.99	2.07
Dipole Entrance Curvature (cm)	69.0	68.5

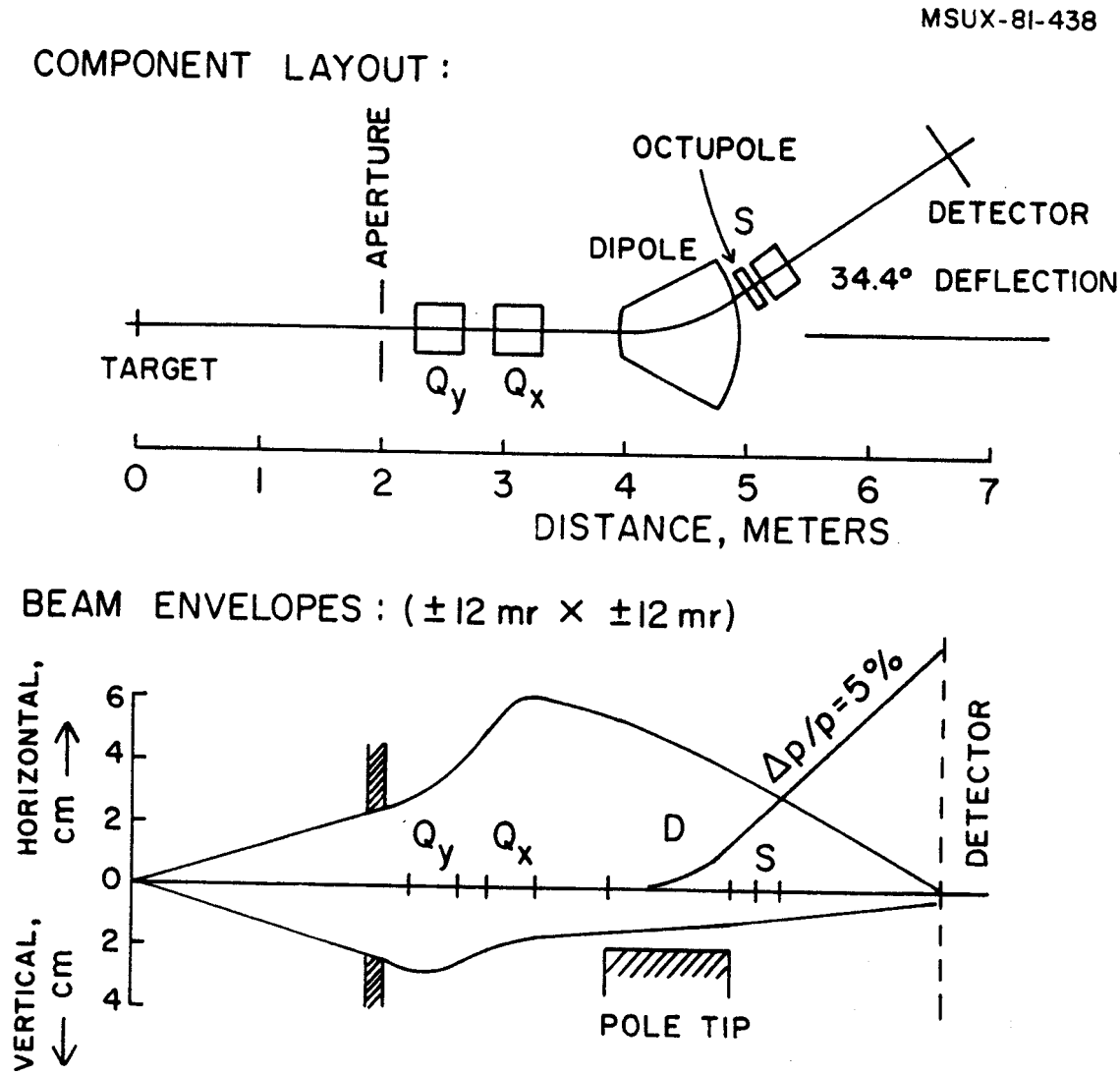

Figure A-3: Schematic layout of the S320 spectrograph showing the first order beam envelopes calculated with TRANSPORT.

A sextupole was used because it can be shown with Liouville's Theorem that a multipole magnet of order n will effect terms of order n or higher. Hence to correct the 2nd order aberration a sextupole was needed. The sextupole however induced an (x/θ^2) term which was corrected by changing the entrance curvature of the dipole. With these changes the spectrograph had the desired energy range and resolution, but only with a 0.3 msr solid angle. The remaining dominant aberration term was the third order term $(x/\theta^2\delta)$. Appendix B describes the design and positioning of the octupole to correct this aberration.

To see the effect of the octupole, the MOTER calculations were run for two cases. One with the octupole and a 0.56 msr solid angle, and one without the octupole and a 0.3 msr solid angle. These calculation will be labeled QQDMS for the 0.56 msr case and QQDS for the 0.3 msr case. All calculations included the full energy range of 20%, and assumed a 3mm high by 2mm wide target spot.

As a first check of the effect of the octupole, MOTER was allowed to optimize the x-quad, y-quad, entrance curvature and sextupole strength for the two cases considered. The results should be identical since the dominant aberration is corrected by the octupole, and as expected, the octupole has no effect below 3rd order. The results are shown in Table A-1. The optimized parameters show essentially no difference between the two cases. The overall resolution in the QQDMS case turns out to be 50%

better than for the QQDS case despite the larger solid angle.

The next step was to consider the effect of finite beam energy spread. To study this the momentum resolution was calculated as a function of the beam momentum dispersion on target. The results are shown in Figure A-4 for the two cases. In the QQDS and the QQDMS cases the optimum dispersion on target, δ_{target}, was almost exactly the predicted theoretical value obtained from requiring

$$x_{target} = \frac{(x/\delta)}{(x/x)} \times \delta_{target} \qquad (A.11)$$

where x_{target} is the horizontal position on target, and δ_{target} is the momentum deviation of the beam from the central momentum. The addition of the multipole field was seen to increase the required dispersion by approximately 2%, possible because the multipole has a small quadrupole field.

Finally, kinematic effects were included and corrected using the optimizing feature of MOTER. To correct for a given $k = -(\delta/\theta)$ the focal plane had to be moved, or the quadrupole fields varied. In our case MOTER was allowed to retune the x-quad.

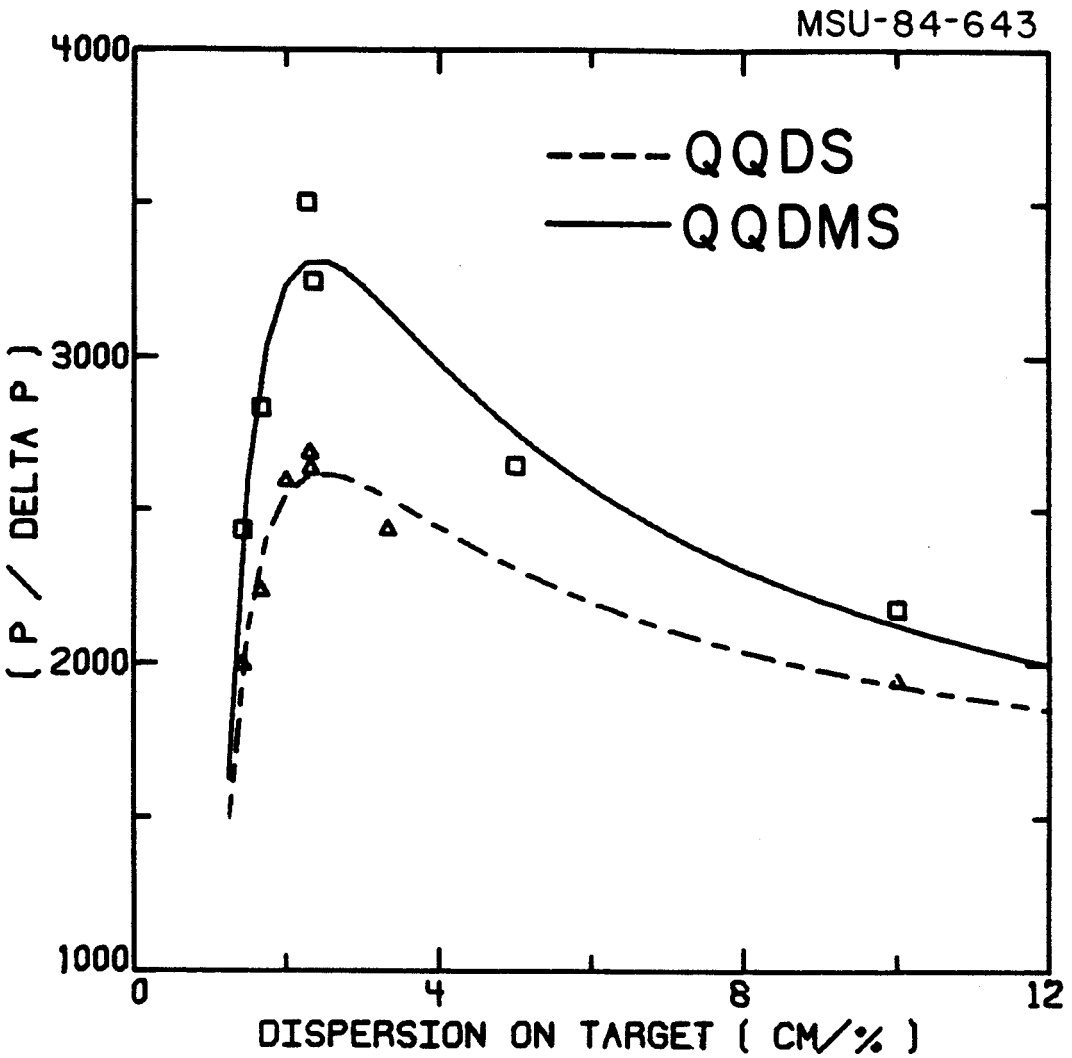

Figure A-4: The optimum beam dispersion search for the S320 spectrograph.

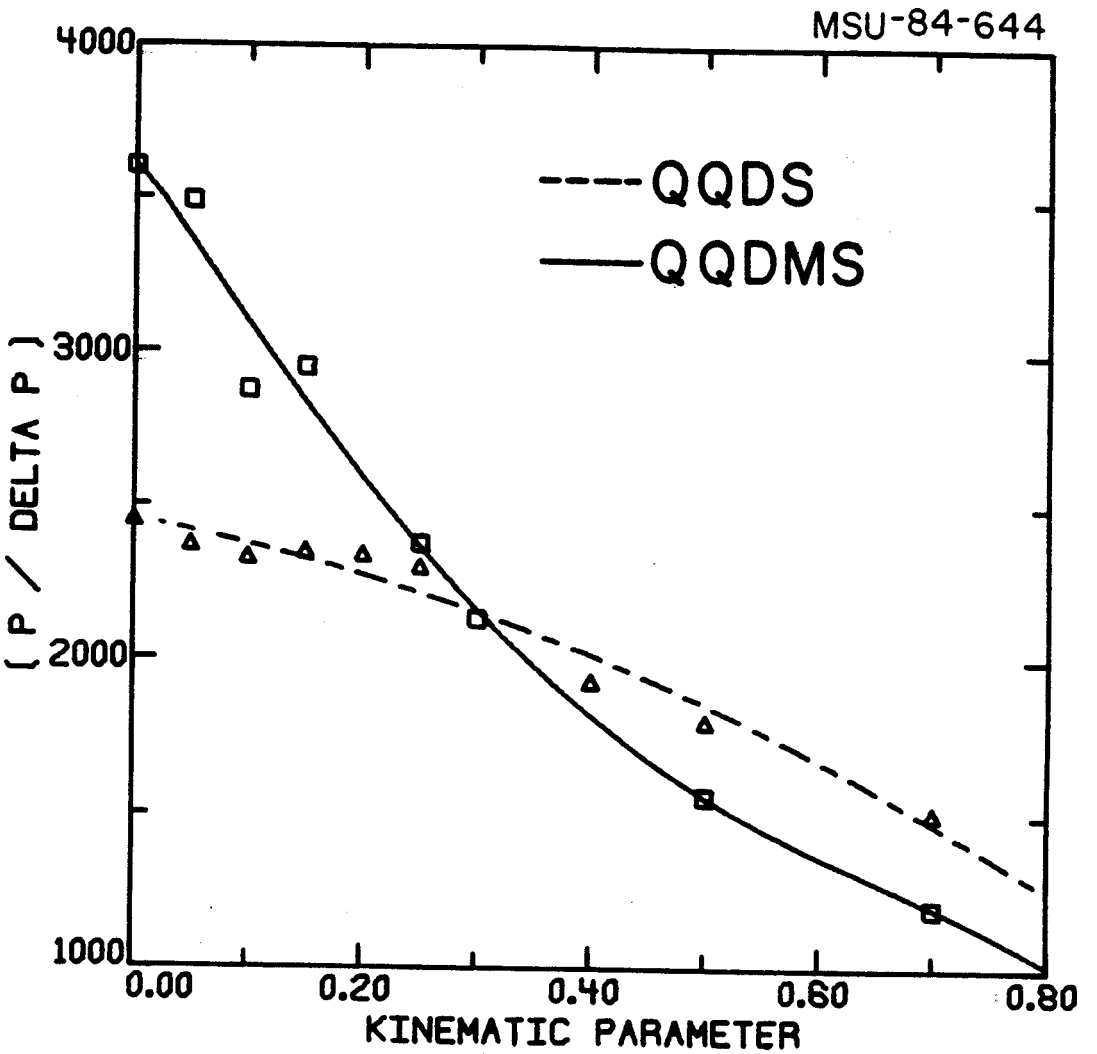

Figure A-5: Calculated effects of reaction kinematics including the x-quad retuning. The QQDS case is better at larger k because of the smaller solid angle.

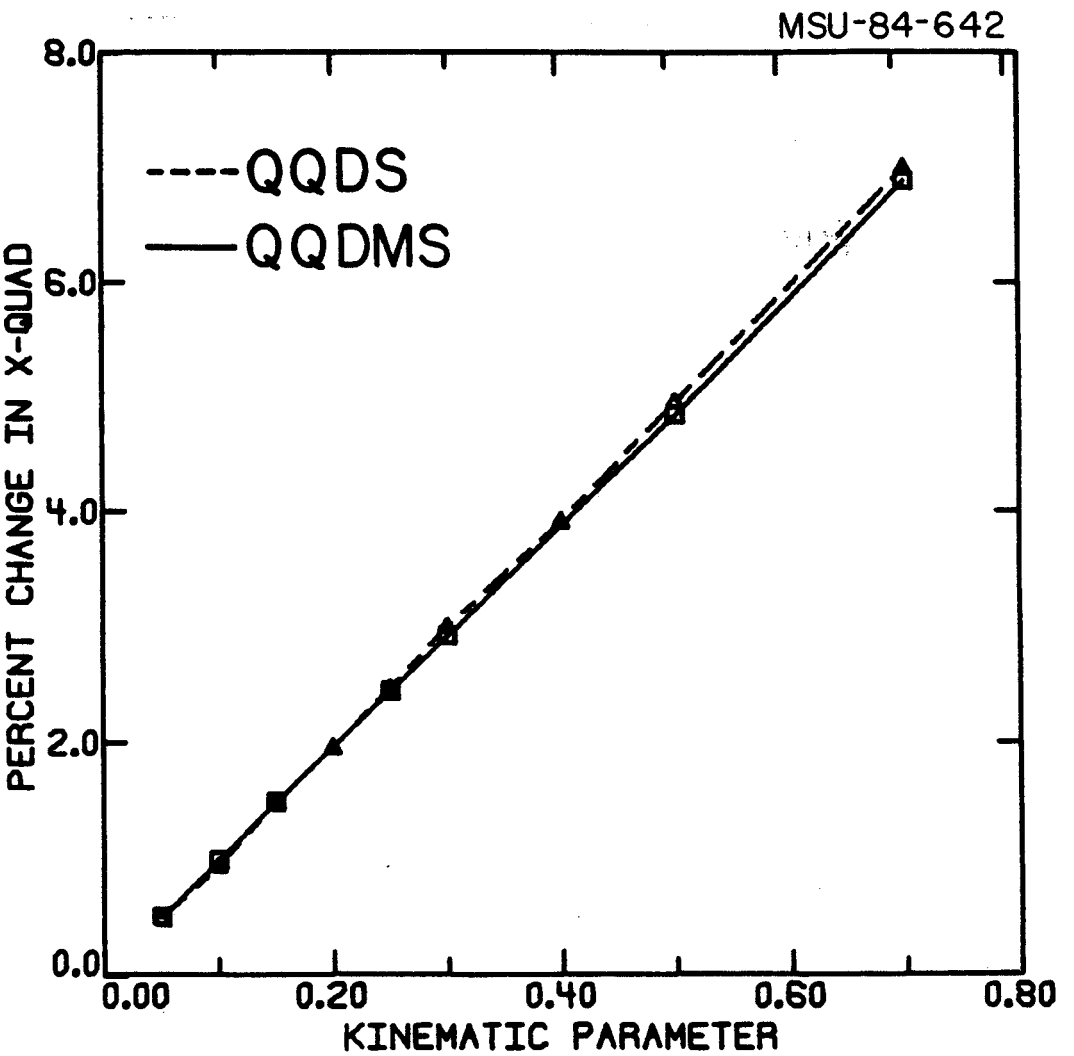

Figure A-6: Percent change in the x-quad needed to correct reaction kinematics.

It was found unnecessary to retune the y-quad or any other spectrograph parameters. The results of the two cases are shown in Figure A-5. We found a linear relationship between the k parameter and the required percentage change in the x-quad strength (see Figure A-6). The resolution plotted in Figure A-5 includes the x-quad correction and hence shows the resolution of the device as a function on kinematic parameter.

A.5 Preliminary Experimental Results

To date a detailed study of the S320 spectrograph has not been performed. In fact one of the most detailed studies was done in connection with the mass measurement described in Chapter 2. In general, however, it is possible to make several comments on the agreement between the overall operation of the spectrograph and the predicted behavior. One feature which has made detailed comparisons of the optics theory to empirical results difficult is the lack of measurement of the magnetic field of any of the elements except the dipole. Thus it is difficult to know if the optimum spectrograph parameters determined empirically agree with the predicted values.

The empirical optimum values were determined from elastic scattering of ions from the K500 cyclotron. To simulate a $\delta \neq 0$ all spectrograph parameters were changed by the amount δ. The resolution was studied typically at $\delta = \pm$

5%, 0%. By displaying x vs. θ it was possible to observe and determine which aberration was affecting the resolution and correct it with the appropriate multipole. For example an (x/θ) term which varied with δ must be the second order term (x/θδ). This aberration was then corrected by a change in the sextupole strength. Using this technique it was possible to obtain a constant resolution of $E/\Delta E = 667$ over the full range of the focal plane. The uncertainty in the angular measurement made determining whether a higher order aberration was responsible for the limited resolution. The design resolution was $E/\Delta E = 1000$. The inability to reach the optimum resolution is currently not understood. There are many possible explanations. One was that space limitations which caused the focal plane to be placed 20cm closer to the dipole than the optimized value is responsible. However recalculations with MOTER using the shorter drift length show that this would not make the resolution worse than the design $E/\Delta E = 1000$. Since the resolution seems to be independent of the S320 solid angle, this indicates it is not a spectrograph aberration. The most likely cause in this case is beam properties worse than that assumed in the calculations. Further study is needed to determine if this is this is true.

The technique of changing the x-quad to correct for reaction kinematics has been verified to work as predicted. The use of the entrance curvature to cancel the induced (x/θ^2) term from the sextupole also seems to have worked

since a uniform spot size can be obtained at all positions in the focal plane. The use of the octupole also seems to improve the spectrograph's resolution, and is necessary to obtain uniform resolution over the full spectrograph range. Finally although not a detailed comparison, the signs of the strengths in all the elements agree with the predicted sign from MOTER.

In the future a more detailed study is planned to attempt to determine the cause of the less than optimum resolution and test the accuracy of the optical design.

APPENDIX B

To achieve the requirements of a 0.56 msr solid angle and energy resolution of $E/\Delta E = 1000$ for the S320 spectrograph, optical corrections to higher than 2nd order had to be made. The conventional approach would be to build the corrections into the dipole exit curvature, or equivalently to build an octupole magnet. Since the dipole exit curvature was difficult to change, the octupole magnet approach was taken.

The optimum position in the spectrograph for a magnetic element of order n, to correct an aberration of the same order, can be determined from the relation (Br74)

$$\frac{\partial(x/x^i y^j \theta^k \phi^l \delta^m)}{\partial S_n} = \pm \left(\frac{n!}{i!j!k!l!m!}\right) \times (x/x)^i (x/y)^j \times (x/\theta)^k (x/\phi)^l (x/\delta)^m \times M \qquad (B.1)$$

where $i+j+k+l+m=n$, M is the spectrograph magnification, and S_n is the strength of a multipole of order n. All matrix elements are evaluated at the location of the multipole.

The primary term to be corrected in the S320 was the $(x/\theta^2\delta)$ term. Using equation B.1 we see the octupole will have the most effect on this aberration where $(x/\theta)^3(x/\delta)$ is large. This occurs between the dipole and the sextupole. This region is actually between the coils of the dipole and hence is only 6 inches high, while the beam phase space fills 3 inches of this area. Due to these limitations a conventional octupole magnet, which uses iron poles to create the octupole field, was impractical since it would require at least 10 inches vertically. The solution was to build a magnet which uses a varying current distribution, instead of iron, to shape the magnetic field. An example of this type of magnet (called a current sheet magnet) is the Panofsky quadrupole (Ha59). Previously, higher order multipole magnets of this type have been constructed and included in the Q3D type spectrometers (Ik77).

To understand how current can be used to create a multipole field, consider a two dimensional view of a distribution of iron enclosing a region of air. Along the iron-air interface runs a current density j(s) with direction out of the picture. The variable s is the arc length along the interface starting from some arbitrary reference point. Using Ampere's law it is possible to show

$$j(s) = -\frac{\partial \phi}{\partial s} \qquad (B.2)$$

where,

$$\underline{B} = - \underline{\nabla} \phi \qquad (B.3)$$

A multipole field of order n is defined as

$$\phi = - k_{2n} r^n \sin(n\theta) \qquad (B.4)$$

where $r = (x^2+y^2)^{1/2}$, $\theta = \tan^{-1}(y/x)$, and k_{2n} is the multipole strength. Thus to create a certain multipole the current distribution must be

$$j = n\, k_{2n}\, r^{n-1} \sin\{ \alpha + (n-1)\theta \} \qquad (B.5)$$

where α is the angle between the y-axis and unit vector pointing in the direction ds. Thus with the proper current distribution any multipole field or sum of multipole fields can be created.

To be able to include the effects of finite conductor size, iron geometry, and finite permeabiltiy, the two dimensional code POISSON (Ho81) was used to calculate the magnetic fields. The code uses the result of Maxwell's equations that the field at any point can be taken as the average of the surrounding points on an arbitrary closed contour. Given the boundary conditions and a current distribution the resulting series of linear equations are solved using the overrelaxation method (Bu78). Many different combinations of current and iron were tried to reach a satisfactory final design.

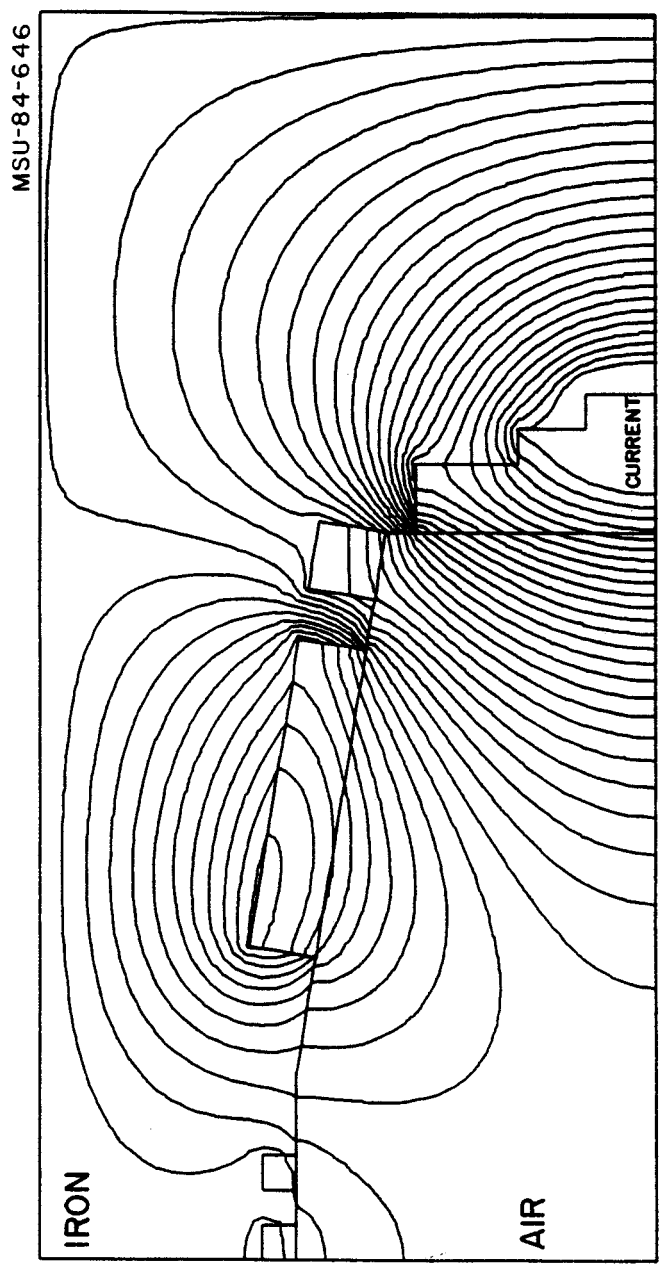

Figure B-1: Cross section of the final design for the octupole magnet. One quarter of the magnet is shown. The boxed regions carry current, while the air and iron regions are labeled. The lines drawn are lines of constant magnetic field calculated with the program POISSON.

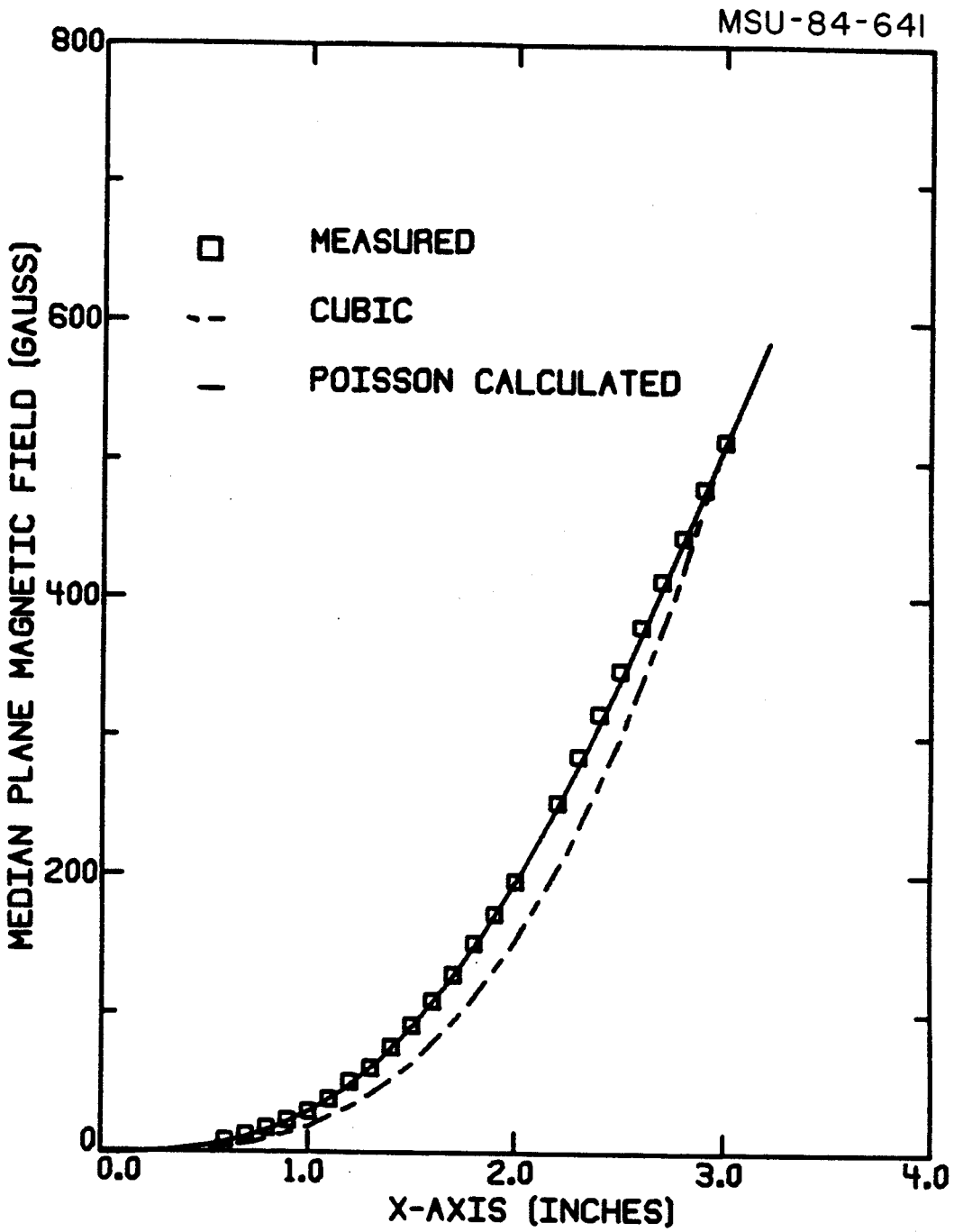

Figure B-2: Plot of the POISSON calculated vs. measured median plane magnetic field. For reference, a true octupole field is also plotted.

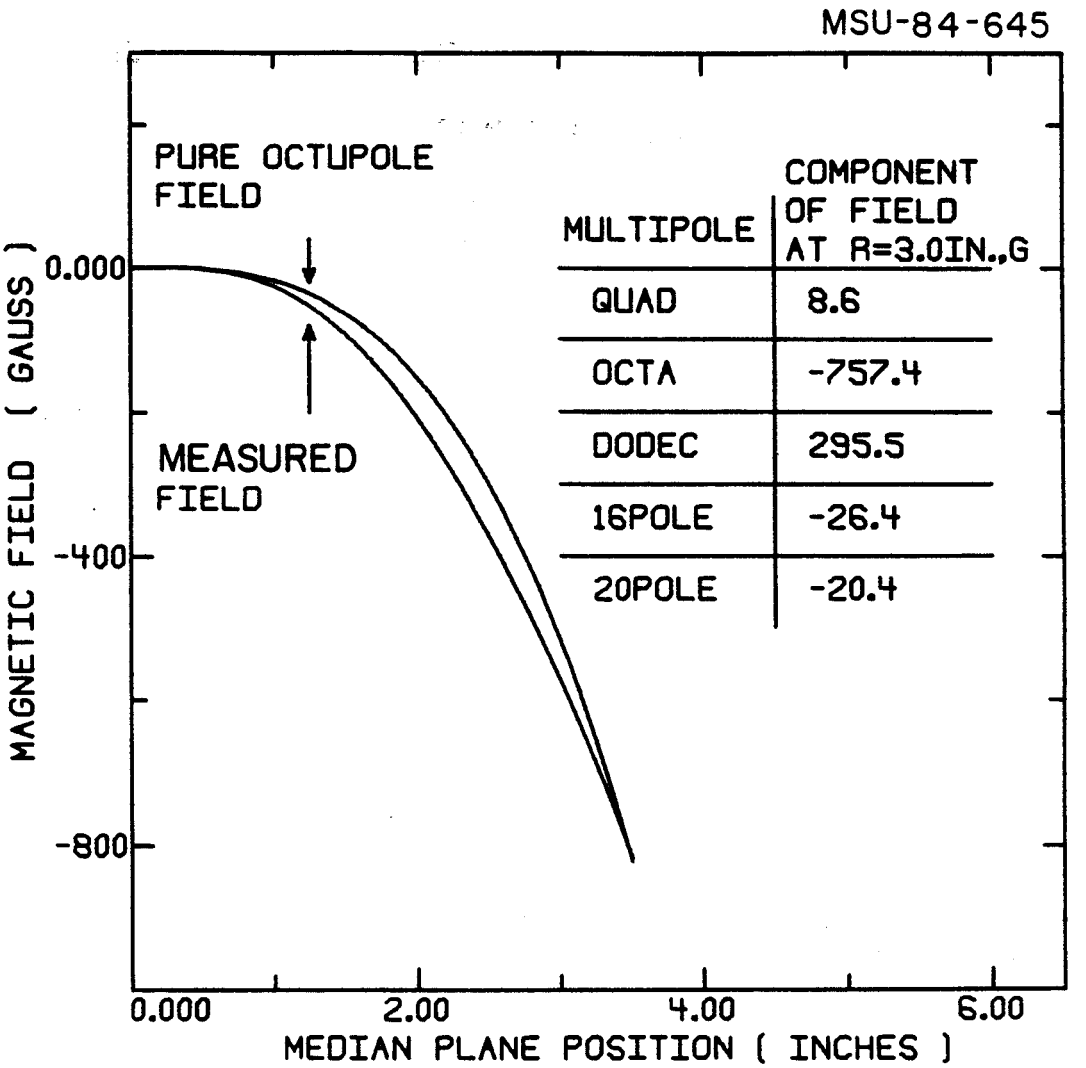

Figure B-3: Detailed comparison between the measured multipole field and a pure octupole field. Also listed are the coefficients from a multipole expansion of the the measured field.

The final design is shown is Figure B-1. Also plotted are lines of constant magnetic field, calculated by POISSON. Figure B-2 shows the calculated and measured median plane field for the completed magnet. As shown in the figure, the true field is not completely octupole. The other higher order components, however, were of the correct sign to correct even higher order aberrations in the spectrograph. Hence, additional attempts to improve the octupole quality of the field would have been counterproductive in the final spectrograph resolution. Figure B-3 shows the comparison of the final median plane field to a pure octupole field. The multipole expansion coefficients for this magnet are also shown in the figure.

The full field of the magnet is 500 G at r = 3 inches. The current for this field is ~100 A, with a power consumption of 1000 W. The conductor is 1/8 inch square with a 1/16 inch diameter hole for cooling water. The cooling water flow rate for the entire magnet is 0.75 gal/min.

Based on the success of the design and construction of this magnet one can conclude that in general the current sheet method is a flexible and workable solution to geometries in which conventional magnets are not practical. The field quality of conventional magnets is generally better, but for many cases the higher order multipole moments are desirable and difficult to build into a conventional magnet.

APPENDIX C

The complexity of the S320 detector requires computer hardware for data taking. Consequently software is needed to allow online display of the data. For this purpose a series of routines under the name SARA have been written to allow data display and manipulation. This same series of routines can also be used for offline analysis. This appendix is intended to serve as an outline and overview of SARA and its relation to the NSCL data acquisition system. A detailed description of the operating procedure and commands for SARA can be found in the SARA manual (Sh84b), hence they will not be discussed here.

The hardware to store and analyze experimental data consists of two major parts. First, an LSI-11 smart CAMAC crate controller buffers the data. The data buffers are passed to the second major component a VAX 11-750 computer via a Kinetic Systems serial highway driver. The VAX 11-750 is used to write the data buffers onto magnetic tape and display the incoming data on an AED color graphics display.

Figure C-1 show a schematic diagram of the NSCL data taking system. Figure C-2 shows a flow diagram for online data taking. The data are collected and buffered in the LSI-11 and passed to the VAX. The buffers are collected by a program ROUTER and sent to specified subprocesses. The buffers are located in a buffer storage area which is accessed in either a sample or a no-sample mode by the subprocesses. ROUTER notifies the subprocess that it has read a buffer and passes the address at which the routine can access the buffer through a mailbox. The figure shows three commonly used subprocesses. One is a scaler handler which sums and displays scaler totals, and another is a tape handling routine which writes the data buffers to tape. The third, which is the subject of this appendix, is the display and manipulation program SARA. All communications from the user's terminal to the various subprocess are made through a program NOTIFIER. NOTIFIER creates a system mailbox as the input and output devices for the various tasks. The user is able with the CONNECT command to connect the terminal to the mailbox and hence the subprocess.

For offline analysis the picture is simplified as can be seen in Figure C-3. In this case a program simulating ROUTER, named LOG, reads data buffers from tape and passes them to SARA through a system mailbox. SARA is spawned from LOG when LOG is run. When started SARA determines whether it is on or offline by performing a logical translation of SARA_IN, which is the data mailbox for online operation.

MSU-83-247

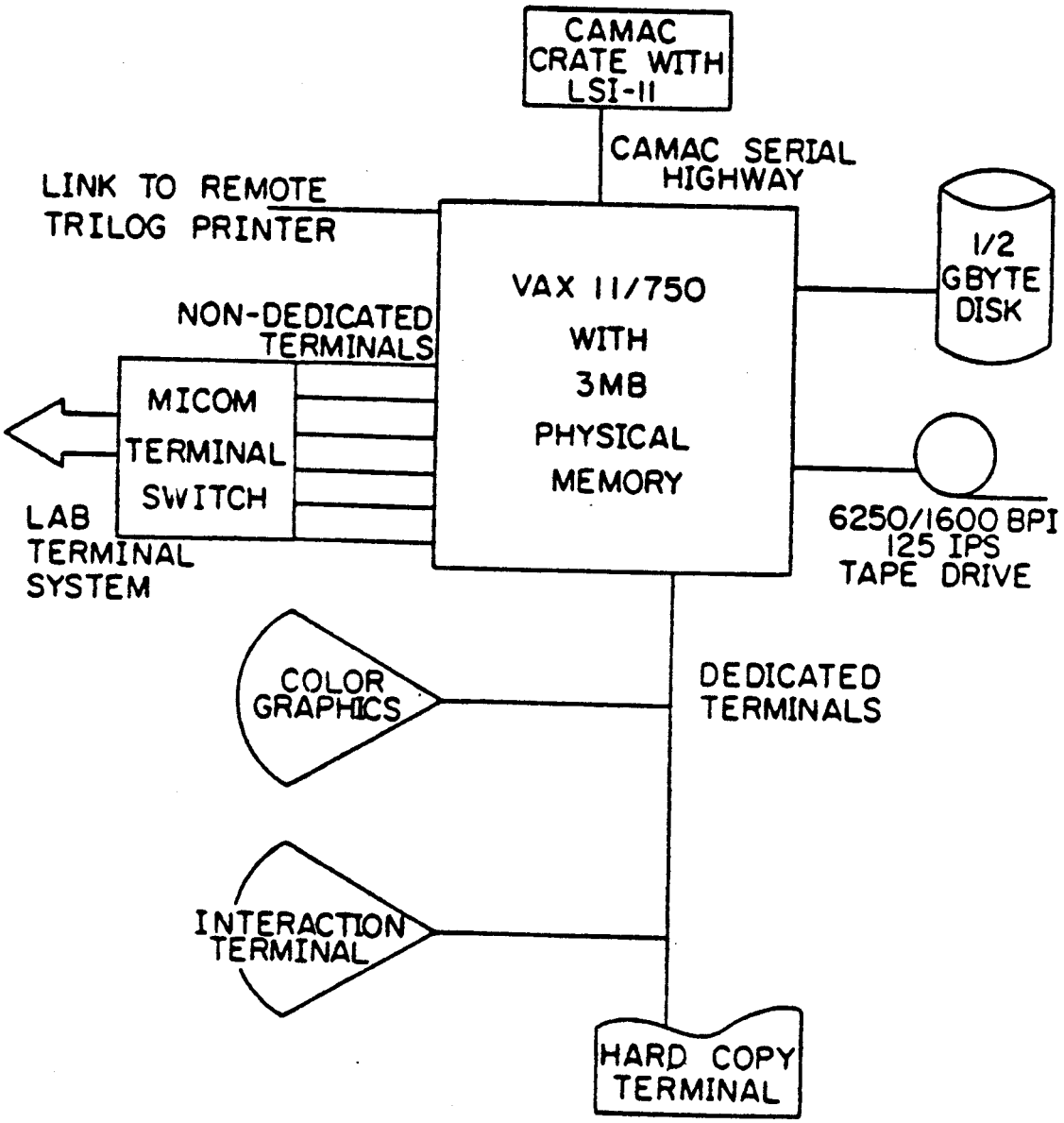

Figure C-1: Schematic diagram of the NSCL data taking system.

MSU-84-632

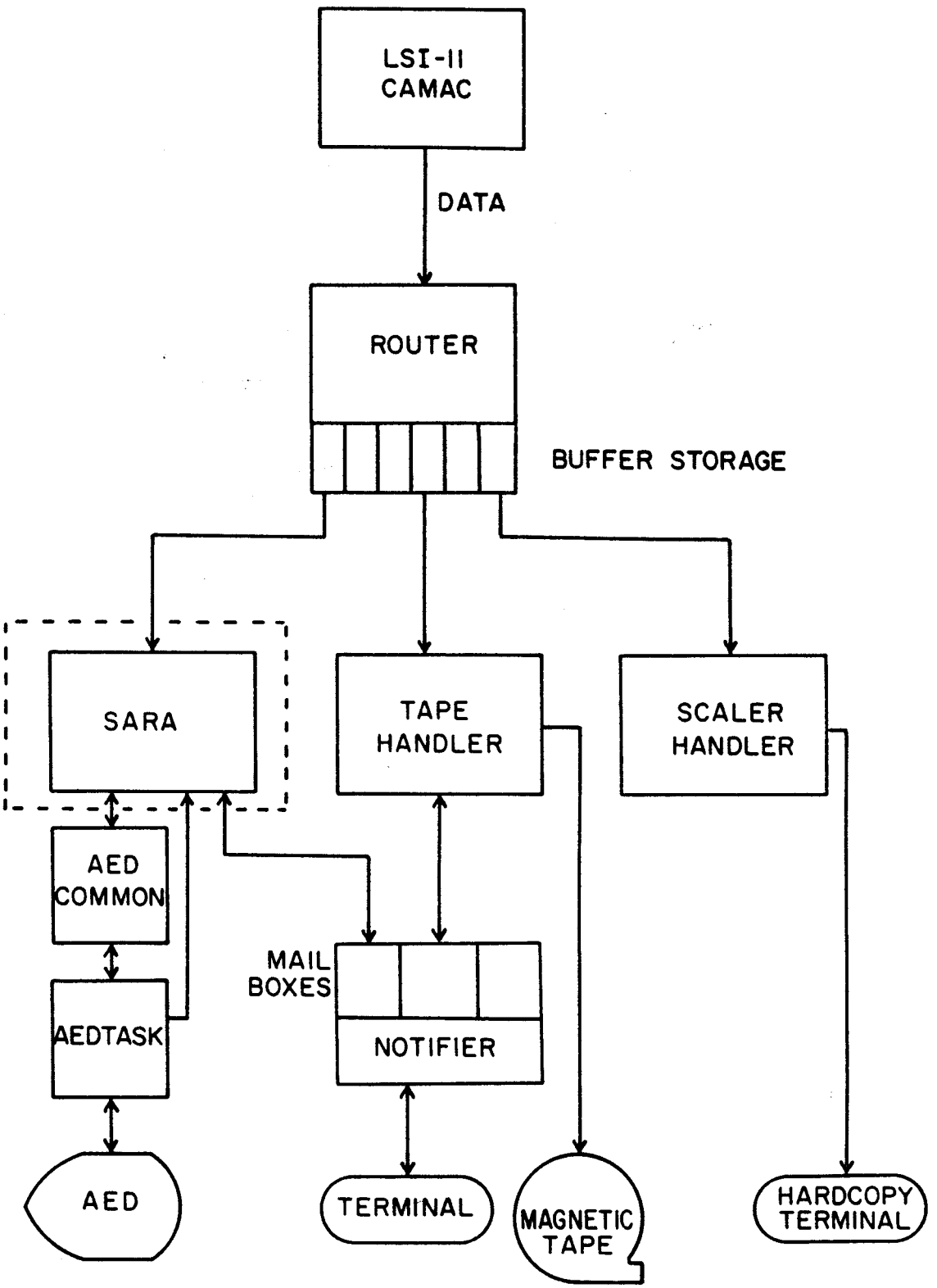

Figure C-2: Flow diagram for online data taking.

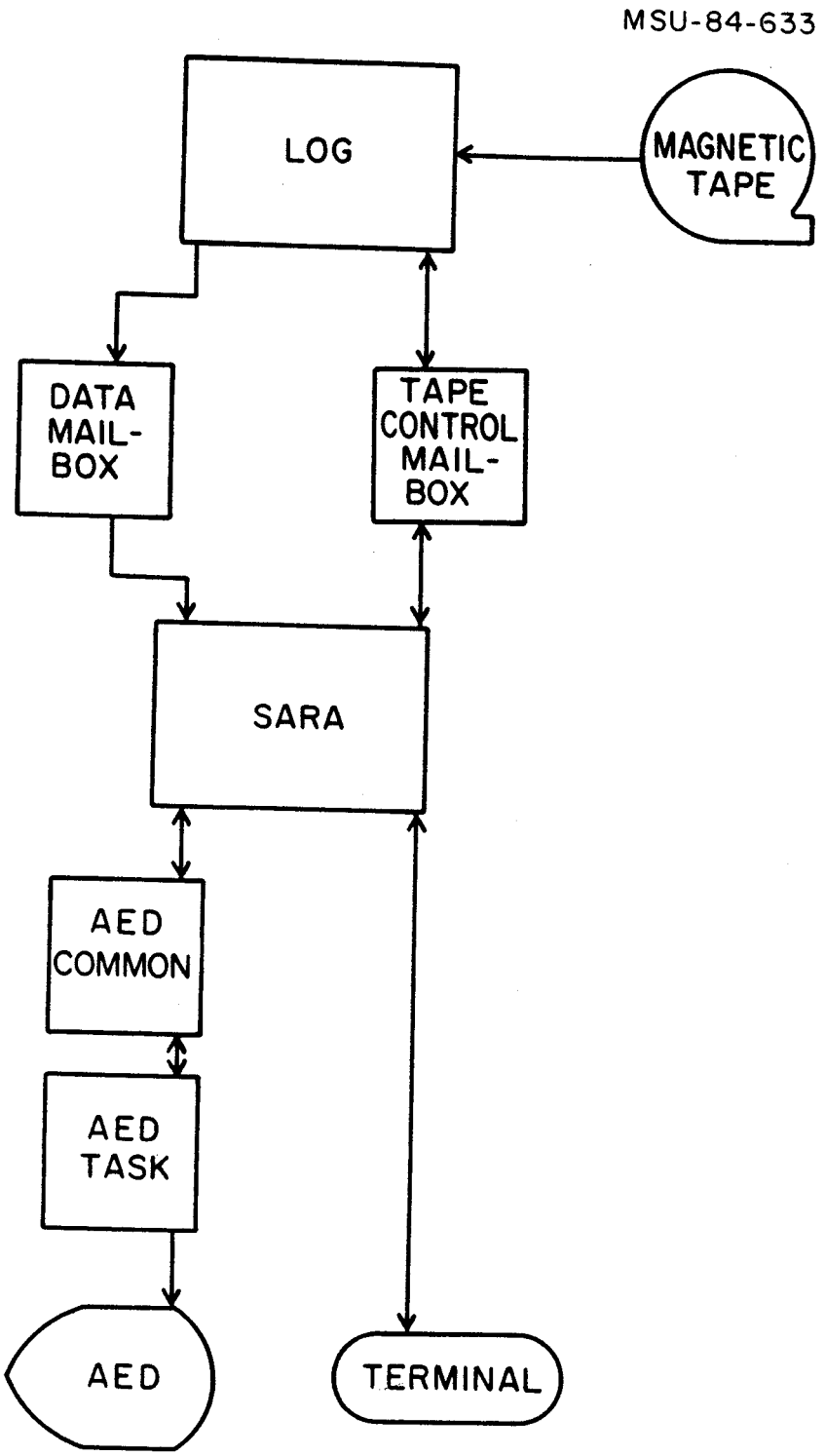

Figure C-3: Flow diagram of offline data analysis.

If SARA_IN translates to a mailbox, the program will run in the online mode. If no translation exists, SARA will run in the offline mode.

The reason that SARA is separated from LOG in the offline data analysis is that this allows the same version of SARA to be used on or offline. Because the data stream will always be passed into SARA, it retains its generality as a display and manipulation routine. Finally, both the ROUTER and LOG programs run independently and can spawn other subprocess. For example, SARA could be replaced by a data compression routine which accepts buffers from LOG and selects events for refiling based on some criteria.

When started, SARA starts the AED color display task AEDTSK (Au82) as a subprocess. SARA and AEDTSK share a common area call AEDCOMMON, which contains condition and histogram definition areas and the histogram data storage area. SARA can be run without starting the AEDTSK. In such a case a virtual memory section is created which is identical to the AEDCOMMON but is not connected with the AEDTSK. AEDCOMMON is created in such a way that all users in the system have access to it. It is possible for other programs to read the data from AEDCOMMON as it is being stored. A potential problem is that the data may also be inadvertently erased or modified by other routines.

SARA is organized around three concepts; parameters, conditions, and histograms. Parameters are defined as the the signals from the experiment, or the pseudo signals which are the results of calculations involving the initial

signals. If for example the experiment consisted of one silicon ΔE-E telescope, there would be two parameters, one for the ΔE signal and one for the E signal. A third possible parameter is a pseudo parameter defined as the total energy; the sum ΔE + E. Histograms then are the one or two dimensional displays of the parameters. Histograms can be gated by conditions. Conditions are one or two dimensional limits defined on the parameters. This includes gates, lines, bands, contours, and circles as defined in the AEDTSK documentation (Au82). The conditions depend only on parameters and not on the histogram they were drawn in. Hence, a condition defined on a previously gated histogram will not preserve the conditions used to gate the histogram. The gating specification for a histogram may include condition negations and complex logical statements involving the logical operations AND, OR, NAND, and NOR. For example a valid condition string could be:

N01 + (C02 . C03),

meaning this histogram should be binned if condition 2 or condition 3 is true and condition 1 is false. The program creates a truth table for the string which is checked before a histogram is binned. The check is quick because the program need only check an element in an array representing the truth table. The appropriate element is determined from the status of the conditions.

A general flow diagram for SARA is shown in Figure C-4. After the program is started, it performs the on- or offline test. Depending on the result, SARA reads data from the

appropriate data stream. This is a mailbox containing the data buffers for offline, which are passed by LOG, or a mailbox containing the address of the buffer passed by ROUTER. Next, the subroutine DEFINE, which reads the user's SETUP file, is called. The SETUP file contains a list of parameters for the experiment, histograms which the user wants binned, and condition definitions which will be used for gating histograms. DEFINE will also start the AEDTSK if desired and initializes the AEDCOMMON area. It also fills the common area DEFCOMMON which contains all parameter, histogram, and condition information used by the routines in SARA. After the initialization a QIO read with no wait is sent to the input device (usually the users terminal), the AED, and the data stream. When one of the reads is satisfied, a local event flag is set, and SARA branches to the appropriate section of code. The priority for the event flag branching has the input device with the highest priority; the AED has the second priority, and the data stream has the lowest priority. The data is interpreted and binned by the subroutine DATAR. Due to the importance of this routine it will be discussed in detail.

Figure C-5 is a detailed flow diagram for the DATAR subroutine. The first operation is to print a section of the buffer if requested by the user using the command SBUF. Next, the sampling efficiency is calculated as

Sampling Efficiency= # of buffer processed/ sequence number of last buffer.

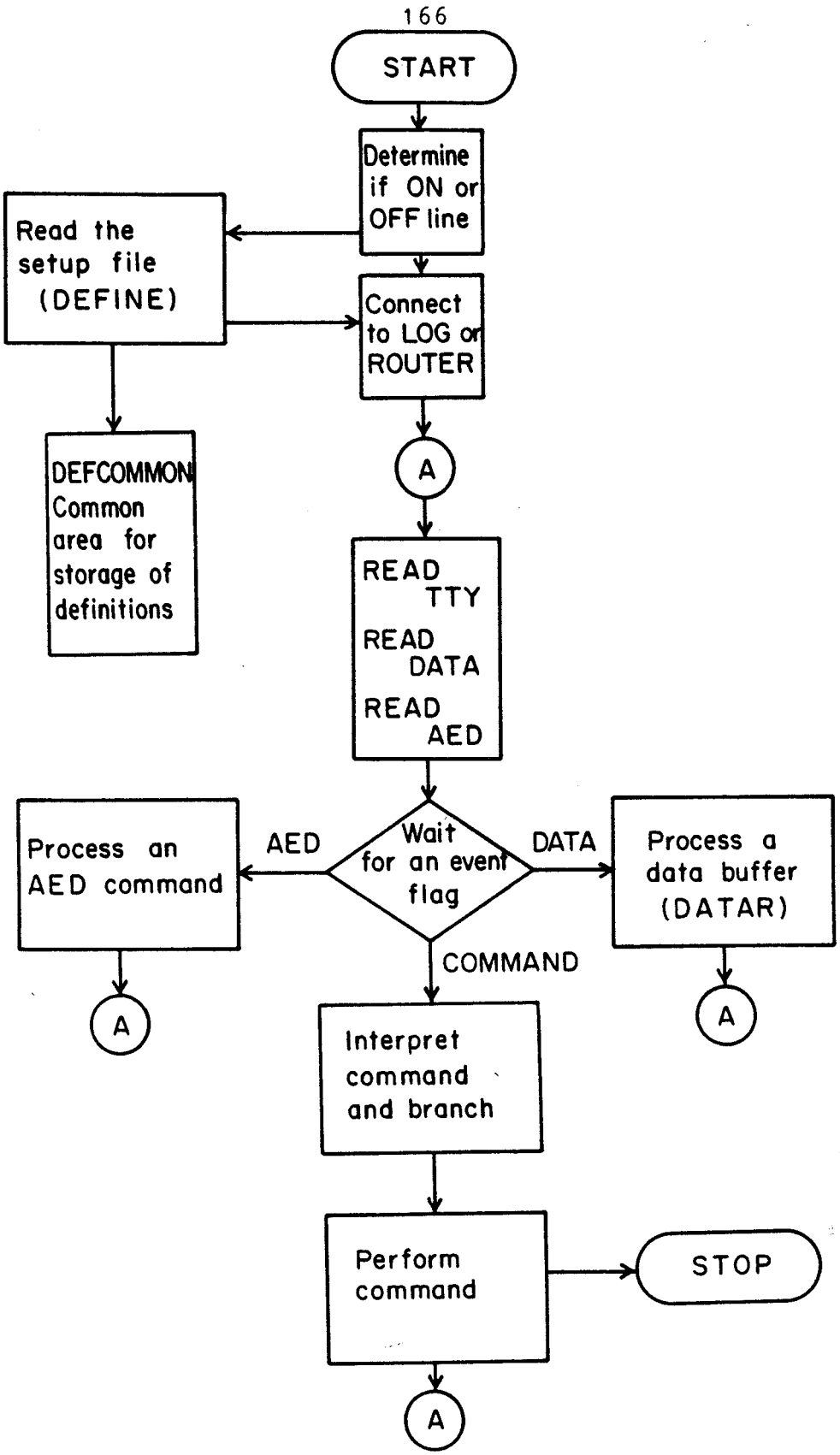

Figure C-4: Flow diagram for the program SARA.

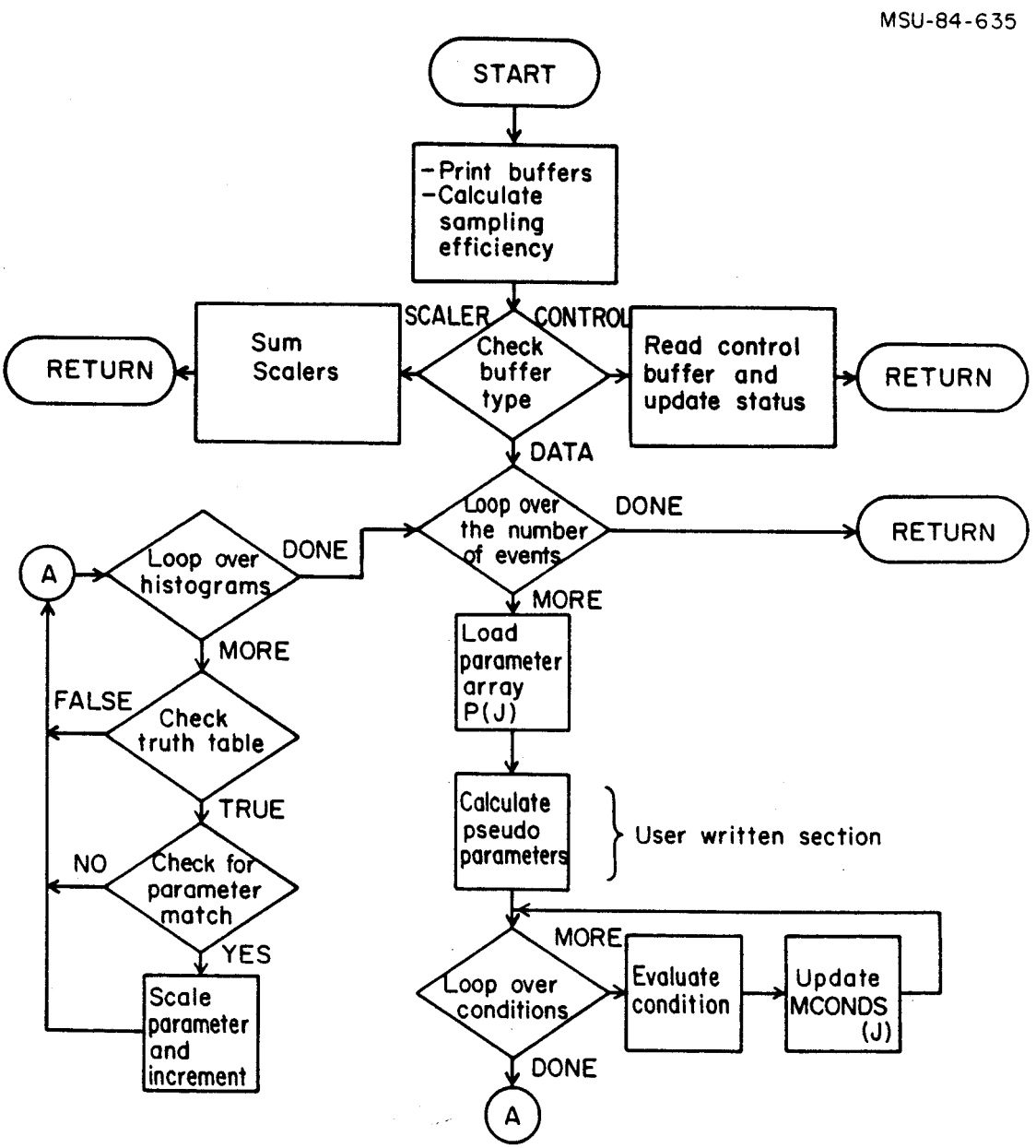

Figure C-5: Flow diagram for the subroutine DATAR.

It is important to remember that the scaler buffers are also given sequence numbers, hence the sampling efficiency also reflects the sampling efficiency for scaler buffers. Therefore the sampling efficiency must be used with caution in determining cross sections online. The routine then checks the buffer type (START, STOP, PAUSE, RESUME, SCALER, or DATA) and branches to the appropriate section of code. Control buffers are used to update status information. Scaler buffers are read, and the scalers summed. For offline analysis additional buffer types exist which indicate the end of a file or a tape read error.

If the buffer is a data buffer, the program starts a DO loop which runs over the number of events in the buffer. First, based on the event type, the parameters are loaded into the slot in the parameter array, P(i), where i is the parameter number specified in the SETUP file. A user written section follows in which pseudo parameters can be calculated. After this point the program reads the parameters from the array P(i). The first step before binning the histograms is to check the conditions. Two criteria must be met for a condition to be true. First, the event type must match the event type for the parameters involved in the condition. Second, the parameter must fall within or on the limits of the condition. All conditions are inclusive. The condition status is stored in the array MCONDS(j), where j is the condition number.

The final section of DATAR handles the histogram binning. The program loops through the entered histograms.

Based on the status of the conditions from the condition string entered with the histogram, the truth table associated with the histogram is checked. If the entry is true, the parameter or parameters are checked for a match with the event type. If this is satisfied, the parameters are scaled corresponding to the size of the histogram. The scaling is done by dropping lower order bits of the data word, hence all histograms have dimensions of 2^n where n is an integer.

The speed of SARA in analysing data will vary greatly with the number of pseudo parameters calculated, the number of conditions checked, and the number of histograms binned. In a test case for a 9 parameter experiment with 7 pseudo parameters, 4 conditions, and 10 histograms, timing studies of SARA were made. It was found that equal amounts of time were taken for loading parameters and calculating pseudo parameters as was taken for checking conditions and binning histograms. It was also found that the overall speed of SARA can be increased by up to 50% by compiling DATAR with the NOCHECK qualifier. For the case studied the maximum data analysis rate was 500 events/sec. , which should provide an adequate sampling rate for most experiments. For offline analysis it is recommended that the experimenter first strip the data to eliminate unwanted events. The stripping process will probably speed up data analysis more than any possible improvements in the software.

LIST OF REFERENCES

Aj81 F. Ajzenberg-Selove, Nucl. Phys. A360, (1981) 40.

Al81 K. Aleklett, P. Hoff, E. Lund, and G. Rudstam, Proc. Conf. on Nucl. far from Stability, CERN-Report 84-09, p. 124.

An74 N. Anyes-Weiss, J.C. Cornell, P.S. Fisher, P.N. Hudson, A. Mechaca-Rocha, D.J. Millener, A.D. Panagioutou, D.K. Scott, D. Strotlman, D.M. Brink, B. Buck, P. Jellis, and T. Engeland, Phy. Rep. 12, (1974) 201.

Ar69 A.G. Artukh, G.F. Gridnev, V.L. Mikheev, V.V. Volkov, Nucl. Phys. A137, (1969) 348.

Ar70 A.G. Artukh et al., Phys. Lett. 32B, (1970) 43.

Ar71a A.G. Artukh, V.V. Audeichikov, G.F. Gridnev, V.L. Mikheev, V.V. Volkov, J. Wilczynski, Nucl. Phys. A168, (1971) 321.

Ar71b A.G. Artukh et al., Nucl. Phys. A176, (1971) 284.

Ar79 M. Arnould, in Proc. of AMCO6, (Plenum, New York, 1979), p. 375.

Ar81 Y. Arai et al., Phys. Lett. 104B, (1981) 196.

Ar84 A. Arai et al., Nucl. Phys. A420, (1984) 193.

Au69 E.H. Auerbach et al., Phys. Rev. Lett. 23, (1969) 1253.

Au80 N. Auerbach, V. Bernard and N. vanGiai, Phys. Rev. C 21, (1980) 744.

Au82 R. Au, computer code AEDTSK, NSCL 1982.

Au83 R. Au, R. Fox, D. Notman, and B. Sherrill, NSCL Annual Report 1982-1983, p. 87.

Ay84 J. Äystö, J. Ärje, V. Koponen, H. Hyvönen, A. Havtojärvi, K. Vierinen, Phys. Lett 138B, (1984) 369.

Ba76 A. Barrose, Nucl. Phys. A281, (1977) 267.

Ba82 H. Baier, W. Bentz, Ch. Hajduk, and P.V. Sauer, Nucl. Phys. A386, (1982) 460.

Be76 F.D. Becchetti, C.E. Thorn, and M.J. Levine, NIM 138, (1967) 93.

Be79 W. Benenson and E. Kashy, Rev. Mod. Phys. 51, (1979) 527.

Be80 E. Bergmann et al., in Proc. of the Int. Conf. on Nucl. Physics, (Berkeley, 1980) p. 110.

Be83 K. Beard, private communication, SPECKINE9 computer program.

Be84 G. Bertsch, private communication.

Bi76 P.K. Bindal, D.H. Youngblood, and R.L. Kozub, Phy. Rev. C 14, (1976) 519.

Bi83 J. Birchall et al., in High Energy Spin Physics 1982, AIP Conf. Proc. 95, (AIP,New York, 1983), p.165.

Bl52 J.M. Blatt and V.F. Weisikopf, Theoretical Nuclear Physics, (Wiley, New York, 1952).

Bo71 S. Borg, I. Bergström, G.B. Holm, B. Rydberg, L.E. DeGeer, G. Rudstam, B. Grapengiesser, E. Lund, and L. Westgaard, NIM 91, (1971) 109.

Bo74 J.D. bowman, A.M. Poskanzer, R.G. Korteling, and G.W. Butler, Phys. Rev. C 9, (1974) 836.

Br70 K.L. Brown, SLAC Report No. 75, (1970).

Br72 D.M. Brink, Phys. Lett. 40B, (1972) 36.

Br74 K.L. Brown and Ch. Iselin, CERN 74-2, (1974).

Br77a B.J. Brussard and P.W.M. Glaudemans, Shell-Model Applications in Nuclear Spectroscopy, (North-Holland, New York, 1977) Chpt. 12.

Br77b K.L. Brown, F. Rothacker, D.C. Carey, Ch. Iselin, SLAC Report No. 91, (1977).

Br78a B.A. Brown and L. Meyer-Schutzmeister (unpublished).

Br78b R.A. Brandenburg, S.A. Coon, and P.V. Sauer, Nucl. Phys. A294, (1978) 305.

Br78c B.A. Brown, W. Chung, and B.H. Wildenthal, Phys.

Rev. Lett. 40, (1978) 1631.

Br79 B.A. Brown, S.E. Massen, and P.E. Hodgson, J. Phys. G 5, (1979) 1655.

Br80a B.A. Brown, W. Chung and B.H. Wildenthal, Phys. Rev. C 22, (1980) 774.

Br80b D.S. Brenner et al., Proc. Int. Symp. on Future Directions in the Study of Nucl. far from Stab., (North-Holland, Amsterdam, 1980) p. 389.

Br81 D.S. Brenner et al., in Proc. Conf. on Nucl. far from Stability, CERN-Report 84-09, p. 123.

Br83a B.A. Brown, O. Scholten, H. Toki, Phys. Rev. Lett. 51, (1983) 1952.

Br83b B.A. Brown and B.H. Wildenthal, Phy. Rev. C 28, (1983) 2397.

Br84 B.A. Brown, MSU, private communication.

Bu57 E.M. Burbidge, G.R. Burbidge, W.A. Fowler, and F. Hoyle, Rev. Mod. Phys. 29, (1957) 547.

Bu78 R.L. Burden, J.D. Faires, and A.C. Reynolds, Numerical Methods, (Prindle,Weber and Schmidt, Boston, 1978), Section 8.3, p.388.

C168 D.D. Clayton, Principles of Steller Evolution and Nucleosynthesis, (McGraw-Hill, New York, 1968).

De81 R.P. DeVito, S.M. Austin, W. Sterrenburg, and V.E.P. Berg, Phy. Rev. Letts. 47, (1981) 628.

De83 C. Detraz, M. Langevin, M.C. Goffri-Kouassi, D. Guillemaud, M. Epherre, G. Audi, C. Thibault, F. Touchard, Nucl. Phys. A394, (1983) .

Du84 J.P. Dufour et al., submitted to Z. Phys. A, (1984); and CENBG preprint no. 8430.

En70 H.A. Enge and S. Kowalski, Proc. 3'rd Int. Conf. on Magnet Technology, Hamburg 1970, p. 366.

En78 P.M. Endt and C. vanderLeun, Nucl. Phys. A310, (1978) 1.

En79 H.A. Enge, NIM 162, (1979) 161.

Fa84 T. Faestermann et al., Phys. Lett. 137B, (1984) 23.

Fe81 H.W. Fearing, Nucl. Phys. A353, (1981) 17C.

Fo84 R. Fox, private communication, SPECTRO program.

Fr55 C.E. Fröberg, Rev. Mod. Phys. 27, (1955) 399.

Fr73 K.J. Fricke, Ap. J. 183, (1973) 941.

Fr74 K.J. Fricke, Ap. J. 189, (1974) 535.

Fr77 E. Friedman and S. Shlomo, Z. Phys. A 238, (1977) 67.

Fr78 K.J. Fricke and W. Ober, personal communication; Ann. NY Acad. Sci. 336, (1980) 399.

Fu81 M. Fujioka, T. Shinozuka, E. Tanaka, Y. Arai, S. Hayashibe, and T. Ishimatsu, NIM 186, (1981) 121.

Ga81 B. Gabioud et al., Phys. Lett. 103B, (1981) 9.

Ga84 S. Gales, E. Hourani, M. Hussonois, J.P. Schapira, L. Stab, M. Vergres, Phys. Rev. Lett. 53, (1984) 759.

Gi81 N. vanGiai and H. Sagawa, Nucl. Phys. A371, (1981) 1; and Phys. Lett. 106B, (1981) 379.

Gi84 R. Gilman et al., Phy. Rev. C 30, (1984) 958.

Gr80 S.A. Gronemeyer, L. Meyer-Schützmeister, A.J. Elwyn, and G. Hardie, Phys. Rev. C 21, (1980) 1290.

Gr82 M.C. Green, in Proc. Conf. on Pion Absorption in Nuclei, AIP Conf. Proc. 79, (AIP, New York, 1982) p. 131.

Gr83 M.C. Green, PhD. Thesis (unpublished).

Gr84 J.M. Greben and A.W. Thomas, Phys. Rev. C 30, (1984) 1021.

Ha49 O. Haxel, T.H.D. Jensen, and H.E. Suces, Phys. Rev. 75, (1949) 1766.

Ha59 L.N. Hand and W.K. Panofsky, Rev. Sci. Instr. 30, (1959) 927.

Ha67 M. Harchol, A.A. Jaffe, J. Miron, I. Unna, and J. Zioru, Nucl. Phys. A90, (1967) 459.

Ha75 C.J. Hanson and H.M. van Horn, Ap. J. 195, (1975) 735.

Ha77 M.L. Halbert, Nucl. Data Sheets 22, (1977) 59.

Ha78 M.L. Halbert, Nucl. Data Sheets 24, (1978) 175.

Ha81a L.H. Harwood and J.A. Nolen Jr., NSCL Annual Report 1980-81, p. 92.

Ha81b L.H. Harwood and J.A. Nolen Jr., NIM 186, (1981) 435.

He32 W. Heisenberg, Z. Phys. 77, (1932) 1.

He73 E.M. Henley, in Few Particle Problems in Nucl. Int., Eds. I. Slavs, R.P. Haddock and W.T.H. van Oers, (North-Holland, Amsterdam, 1973), p.221.

He79 E.M. Henley and G.A. Miller, in Mesons in Nuclei, Ed. M. Rho and D. Wilkinson, (North Holland, Amsterdam, 1979) Chpt. 10.

He81 A.G.M. van Hees and P.W.M. Glaudemans, Z. Phys. 303, (1981) 267.

Ho65 F. Hoyle and W.A. Fowler, in Quasi-Stellar Sources and Gravitational Collapse, Ed. I. Robinson, A. Schild, and E.L. Schucking (Univ. Chicago Press, Chicago, 1965) p. 62.

Ho75 F. Hoyle, Ap. J. 196, (1975) 661.

Ho81a J. Honkanen et al., Nucl. Phys. A366, (1981) 109.

Ho81b R.F. Holsinger and L.H. Harwood, private communication.

Hu80 F. Hubert, A. Fleury, R. Bimbot, and D. Gardes, Ann. de Phys. Supp. 5, (1980) 1.

Ik77 H. Ikegami et al., RCNL Annual Report, (1977) 137.

Ja68 J. Jäneke, Isospin in Nuclear Physics, Ed. D.H. Wilkinson (North-Holland, Amsterdam, 1968) p.297.

Jo80 P.C. Joss and F.K. Li, Ap. J. 238, (1980) 287.

Ka75 E. Kashy et al., AMCO5, (Plenum Press, New York, 1975).

Ke66 I. Kelson and G.T. Garvey, Phys. Lett. 23, (1966) 689.

Kl79 P. Kleinheinz et al., Z. Phys. A290, (1979) 279.

Ko79 J. Kowalski et al., Z. Physik A290, (1979) 345.

Ko81 S. Kowalski and H.A. Enge, MIT program (unpublished).

La84 M. Langevin et al., Orsay Preprint IPNO/DRC-84-36,

(1984).

Le78 C.M. Lederer and V.S. Shirley, Table of Isotopes (Wiley, New York, 1978).

Ma48 M.G. Mayer, Phys. Rev. 75, (1949) 1969.

Ma76 S. Maripuu Spec. Ed., At. Data Nucl. Data Tables 17, (1976) .

Ma83 S.A. Martin et al., NIM 214, (1983) 281.

Me78 L. Meyer-Schützmeister, A.J. Elwyn, S.A. Groneneger, G. Hardie, R.E. Holand, and K.E. Rehm, Phys Rev. C 18, (1978) 1148.

Mi83 H. Miyatake, T. Shimouka, H. Hama, M. Yoshii, T. Kamiya, and M. Fujioka, CYRIC Annual Report 1983, p. 17.

Mo83 R.B.M. Mooy and P.W.M. Glaudemans, Z. Phys. 312, (1983) 59.

Mu75 D. Mueller, E. Kashy, W. Benenson, and H. Nann, Phy. Rev. C 12, (1975) 51.

Mu77 D. Mueller, E. Kashy, and W. Benenson, Phys. Rev. C 15, (1977) 1282.

Mu84 J.A. Musser and J.D. Stevenson, to be published in Phys. Rev. Lett.

My76 W. Myers, At. Data Nucl. Data Tables 17, Ed. S. Maripuu, (1976) 411.

Na79 M.M. Nagels et al., Nucl. Phys. B147, (1979) 189.

Ne74 J.W. Negele, in Proc. of the Int. Conf. on Nucl. Structure and Spec., Ed. H.E. Blok and A.E.L. Dieperink (Scholars, Amsterdam, 1974), Vol. 2, p.618.

No69 J.A. Nolen Jr. and J.P. Schiffer, Annu. Rev. Nucl. Sci. 19, (1969) 471.

No74 J.A. Nolen Jr. et al., NIM 115, (1974) 189.

No77 J.A. Nolen, T.S. Bhatia, H. Hafner, P. Doll, C.A. Wiedner, and G.S. Wagner, Phys. Lett. 71B, (1977) 314.

No81 J.A. Nolen Jr., M. Distasio, B. Sherrill, N. Kedarnath, and M. Pangia, NSCL Annual Report 1980-81, p. 93.

Oe82 W.T.H. van Oers, Comments Nucl. Part. Phys. 10,(1982)

251.

Pl83 J. vanderPlicht, W. Benenson, R.A. Blue, W.G. Lynch, B. Sherrill, J. Yurkon, NSCL Annual Report 1982-83, p. 109.

Po65 A.M. Poskanzer, P.L. Reader, and J. Dostrovosky, Phys. Rev. 138, (1965) 1318.

Po73 F. Poughon and P. Roussel, Phys. Rev. Letts. 30, (1973) 1223.

Po77 A. Poves, A.L. Cedillo, and J.M.G. Gomes, Nucl. Phys. A293, (1977) 397.

Ra84 W.D.M. Rae, A. Etchegoyen, N.S. Godwin, and B.A. Brown, computer code OXBASH, Oxford-Buenos Aires, 1984.

Re72 M. Rees, Phys. Rev. Lett. 28, (1972) 1669.

Ro78 E. Roeckl, R. Kirchner, O. Klepper, G. Nyman, W. Reisdorf, D. Schardt, K. Wien, R.Fass, S. Mattesson, Phys. Lett. 78B, (1979) 393.

Ro79 E. Roechel, in Proc. of AMCO6, (Plenum, New York, 1979), p. 389.

Ro84a H.J. Rose and G.A. Jones, Nature 307, (1984) 245.

Ro84b E. Roeckl, private communication; see also papers in Proc. of AMCO7, to be published.

Sa20 M.N. Saha, Phil. Mag. 40, (1920) 472.

Sa76 H. Sato, Nucl. Phys. A281, (1977) 267.

Sa77 P.V. Sauer and H. Walliser, J. Phys. G 3, (1977) 1513.

Sc68 L.I. Schiff, Quantum Mechanics, (McGraw-Hill, 1968) 268.

Sc76 H. Schmeing, V. Koslowsky, M. Wightman, J.C. Hardy, J.A. McDonald, T. Faestermann, H.R. Andrews, J.S. Geiger, and R.L. Graham, NIM 139, (1976) 335.

Sc79 D. Schardt et al., Nucl. Phys. A326, (1979) 65.

Sc81 D. Schardt et al., in Proc. Conf. Nucl. far from Stability, CERN-Report 84-09, p. 168.

Sc83 D. Schüll, GSI preprint, GSI-38-2, (1983).

Se65 P.A. Seeger, W.A. Fowler, and D.D. Clayton, Ap. J. Suppl. 11, (1965) 121.

Se78 K.K. Seth, H. Nann, S. Iverson, M. Kaletka, J. Hird, and H.A. Theissen, Phys. Rev. Lett. 41, (1978) 1589.

Sh74 A. deShalit and H. Feshback, Theoretical Nuclear Physics V.1, (Wiley and Sons, New York,1974), Chpt 9.

Sh76 E.B. Shera et al., Phys. Rev. C 14, (1976) 731.

Sh77 S. Shlomo and E. Friedman, Phys. Rev. Lett. 39, (1977) 1180.

Sh78 S. Shlomo, Rep. Prog. Phys. 41, (1978) 957.

Sh83 B. Sherrill, K. Beard, W. Benenson, B.A. Brown, E. Kashy, W.E. Ormand, H. Nann, J.J. Kehayias, A.D. Bacher, and T.E. Ward, Phys. Rev. C 28, (1983) 1712.

Sh84a T. Shinozuka, M. Fujioka, H. Miyatake, M. Yoshii, H. Hama, T. Kamiya, Phy. Rev C 30, (1984) 2111.

Sh84b B. Sherrill, J. Winfield, and M. Lowe, NSCL Report No. MSUCL-499, (1984).

Sh85 B. Sherrill, K. Beard, W. Benenson, C. Bloch, B.A. Brown, E. Kashy, J.A. Nolen Jr., A.D. Panagiotou, J. vanderPlicht, and J.S. Winfield, to be published in Phys. Rev. C, (1985).

Sp67 J.E. Spencer and H.A. Enge, NIM 49, (1967) 181.

St74 S. Starrfield, W.M. Sparks, and J.W. Truran, Ap. J. Suppl. 28, (1974) 247.

St75 S. Starrfield, W.M. Sparks, and J.W. Truran, Ap. J. 198, (1975) L113.

St81 J.D. Stevenson and P.B. Price, Phys. Rev. C 24, (1981) 2102.

St85a J. Stevenson, S. Barwick, P.B. Price, and H.L. Ravn, Phys. Rev. Letts. 54, (1985) 297.

St85b J. Stevenson, private communication.

Sy79 T.J.M. Symons, Y.P. Yiyogi, G.D. Westfall, P. Doll, D.E. Greiner, H.Faraggi, P.J. Lindstrom, D.K. Scott, Phys. Rev. Lett. 42, (1979) 40.

Ta74 Tamura and Low, Comp. Phys. Comm. 13, (1974) 349.

Ta81 R.E. Tann, Ap. J. 247, (1981) 257.

Th75 C. Thibault, R. Klapisch, C. Rigaud, A.M. Poskanzer, R. Priels, L. Lessard, and W. Reisdorf, Phy. Rev. C 12, (1975) 644.

Th79 H.A. Thiessen, M.M. Klein, and K.G. Boyer, LASL Report, April 1979 (unpublished).

Th82 C.E. Thorn et al., Phys. Rev. C 25, (1982) 331.

To81 F. Tonder, in Proc. 4th Int. Conf. on Nuclei Far from Stability, Helsingor 1981, CERN-Report 81-09, p. 81.

To83a A.W. Thomas, Adv. Nucl. Phys. 13, (1983) 1.

To83b I.S. Towner, and F.C. Khanna, Nucl. Phys. A399, (1983) 344.

Vi76 D.J. Vieira, D.F. Sherman, M.S. Zisman, R.A. Gough, and J. Cerny, Phys. Lett. 60B, (1976) 261.

Vi81 S.E. Vigdor et al., in Polarization Phenomena in Nuclear Physics 1980, AIP Conf. Proc. 69, (AIP, New York, 1981), p.1455.

Vi82 S.E. Vigdor et al., Phy. Rev. Letts. 49, (1982) 1314.

Vi84 D.J. Vieira, J.M. Wouters, G.W. Butler, C. Pillai, L.W. Swenson, K. Vaziri, S.H. rokni, V.G. Lind, L.P. Remsberg, in Proc. of AMCO7, to be published.

Vo78 V.V. Volkov, Phys. Rep. 44, (1978) 93.

Wa67 R.V. Wagoner, W.A. Fowler, and F. Hoyle, Ap. J. 148, (1967) 3.

Wa73 R.V. Wagoner, Ap. J. 179, (1973) 343.

Wa81 R.K. Wallace and S.E. Woosley, Ap. J. Supp. 45, (1981) 389.

Wa82 R.K. Wallace, S.E. Woosley, and T.A. Weaver, Ap. J. 258, (1982) 696.

Wa83 R.K. Wallace and S.E. Woosley, AIP Conf. Proc. 115, (AIP, New York, 1983) p. 319.

Wa84 A.H. Wapstra an G. Audi, 1983 Atomic Mass Table, to be published in Nucl. Phys. A.

We76 R. Welch, private communication, IUCF program RACHEL.

We79 G.D. Westfall et al., Phys. Rev. Lett. 43, (1979) 1859.

Wi74 D.H. Wilkinson and B.E.F. Macefield, Nucl. Phys. A232, (1974) 58.

Wi78 D.H. Wilkinson, A. Gallman, and D.E. Alburger, Phys. Rev. C 18, (1978) 401.

Wi83 B.H. Wildenthal, M.S. Curtin, and B.A. Brown, Phys. Rev. C 28, (1983) 1343.

Wi84 J.S. Winfield and S.M. Austin, private communication.

Wo80 H.D. Wohlfahrt, O. Schwentker, G. Fricke, H.G. Andersen and E.B. Shera, Phys. Rev. C 22, (1980) 264.

Wo81 H.D. Wohlfahrt, E.B. Shera, M.V. Hoehn, Y. Yamazaki, and R.M. Steffen, Phys. Rev. C 23, (1981) 533.

Wo84 J.M. Wouters et al., in Proc. of AMCO7, to be published.

Yu82 J. Yurkon, B. Lynch, and N. Matsushita, NSCL Annual Report 1981-82, p. 72.

Ze82 A.F. Zeller, L.H. Harwood, and J.A. Nolen Jr., NSCL Annual Report 1981-82, p. 88.

Zi80 J.F. Ziegler, Handbook of Stopping Cross-sections, (Pergamon, New York, 1980).